CLOUD-AEROSOL TRANSITION ZONE RADIATIVE EFFECTS FROM MODELING AND OBSERVATIONAL PERSPECTIVES

Babak Jahani

Universitat de Girona

DOCTORAL THESIS

Cloud-Aerosol Transition Zone Radiative Effects from Modeling and Observational Perspectives

Babak Jahani

2021

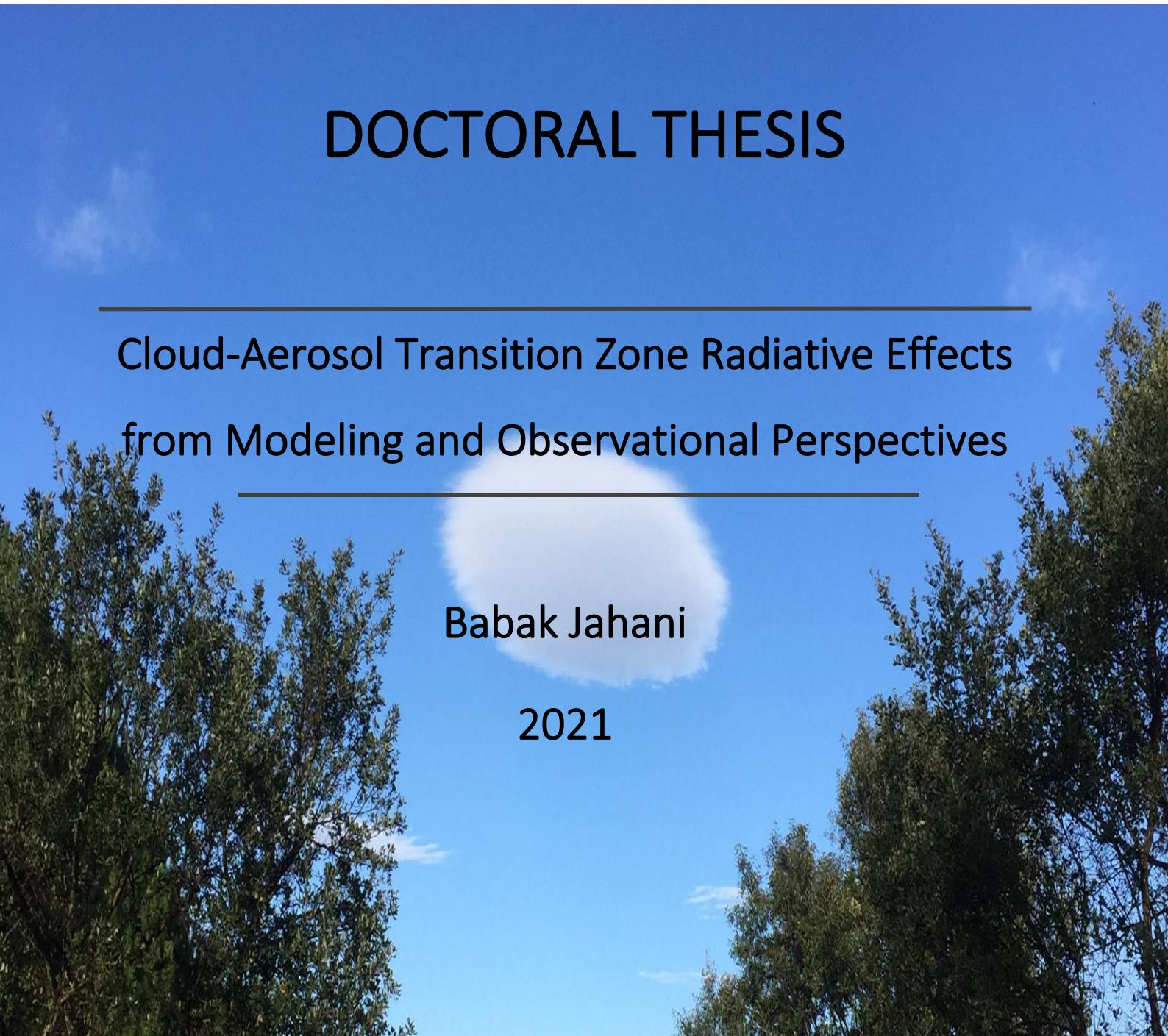

Universitat de Girona

DOCTORAL THESIS

Cloud-Aerosol Transition Zone Radiative Effects from Modeling and Observational Perspectives

Babak Jahani

2021

Doctoral Program in Environment

Supervisors:

Josep Calbó

Josep-Abel González

Thesis submitted to the University of Girona for the degree of doctorate

Universitat de Girona

Dr. Josep Calbó and Dr. Josep-Abel González, of the Department of Physics, Universitat de Girona,

We declare:

That the thesis entitled "Cloud-Aerosol Transition Zone Radiative Effects from Modeling and Observational Perspectives" presented by Babak Jahani for obtaining a doctoral degree, has been completed under our supervision in accordance with the code of good practice and does not contain plagiarized elements, and meets the criteria required for obtaining the Doctorate title.

For all intents and purposes, we hereby sign this document.

Dr. Josep Calbó

Dr. Josep-Abel González

Universitat de Girona

List of Publications

The following papers present results achieved in the framework of this PhD thesis:

- Jahani, B., Calbó, J., & González, J. (2019). Transition zone radiative effects in shortwave radiation parameterizations: Case of weather research and forecasting model. *Journal of Geophysical Research: Atmospheres*, 124, 13,091– 13,104. doi: https://doi.org/10.1029/2019JD031064

- Jahani, B., Calbó, J., & González, J.A. (2020). Quantifying Transition Zone Radiative Effects in Longwave Radiation Parameterizations. Geophysical Research Letters 47 (22), e2020GL090408. doi: https://doi.org/10.1029/2020GL090408

- Jahani, B., Andersen, H., Calbó, J., González, J.A., Cermak, J. (2021) Longwave Radiative Effect of the Cloud-Aerosol Transition Zone Based on CERES Observations. Atmospheric Chemistry and Physics Discussions. doi: https://doi.org/10.5194/acp-2021-421

The methodologies, results and discussion given in these papers comprise the main core of this thesis and for this reason they constitute chapters (4-6).

Universitat de Girona

List of Abbreviations and Symbols defined/used in chapter 1

term	*description*
λ	Wavelength
X	Size parameter
r	Radius of a spherical particle
UV	Ultraviolet radiation
PAR	Photosynthetically active radiation
near-IR	Near Infrared
TOA	Top of the atmosphere
MODIS	MODerate resolution Imaging Spectroradiometer
CALIPSO	Cloud-Aerosol Lidar and Infrared Pathfinder Satellite Observations
MFRSR	Multi-Filter Rotating Shadowband Radiometer
radar	Radio Detection and Ranging
lidar	Light Detection and Ranging

Universitat de Girona

List of Abbreviations and Symbols defined/used in chapter 2

term	*description*
λ	Wavelength
Ω	Solid Angle
sr	steradian
θ''	CERES viewing zenith angle
θ'	Scattering angle
θ	Zenithal angle in polar coordinates / CERES viewing zenith angle at surface
ϕ	Azimuthal angle in polar coordinates
$\delta_{ext,\lambda}$	Monochromatic extinction coefficient
$\delta_{abs,\lambda}$	Monochromatic absorption coefficient
$\delta_{sca,\lambda}$	Monochromatic scattering coefficient
ω_λ	Monochromatic single scattering albedo
g_λ	Monochromatic asymmetry factor
τ_λ	Monochromatic optical thickness
μ	cos(θ)
$P_\lambda(\theta')$	Monochromatic Phase function
dA	Element of area
L_λ	Monochromatic radiance
L	Broadband radiance
E_λ	Monochromatic irradiance
E	Broadband irradiance
dL_λ	Change in radiance value
$L_\lambda(0)$	Initial value of radiance
J_λ	Monochromatic source function
dz	Physical thickness of an atmospheric layer
$B_\lambda(T)$	Monochromatic Planck function for temperature T
$\uparrow L_{CERES}$	Instantaneous outgoing broadband longwave radiances observed at TOA by CERES
$\uparrow L_{RTM,clr}$	Simulated upwelling broadband longwave clear-sky radiances at TOA
AOD	Aerosol optical thickness
CERES	Clouds and the Earth's Radiant Energy System
COD	Cloud optical thickness
ERA5	Fifth generation ECMWF reanalysis
FLG	Fu-Liou-Gu radiation parameterization
FOV	Field of view
h_{sat}	Satellite Altitude
$l_{cross\text{-}scan}$	Estimated cross-scan length of the CERES footprints
$l_{along\text{-}scan}$	Estimated along-scan length of the CERES footprints
lw	Longwave
lwrad	Longwave radiation
MODIS	MODerate resolution Imaging Spectroradiometer

MPAS	Model for Prediction Across Scales
MYD03	MODIS geolocation product
MYD04	MODIS Level-2 aerosol product
MYD06	MODIS Level-2 Cloud product
MYD35	MODIS cloud mask
near-IR	Near Infrared
NGO	New Goddard Parameterization
PAR	Photosynthetically active radiation
R_e	Earth Radius
RRTMG	Rapid Radiative Transfer Model for General circulation models parameterization
RTE	Radiative Transfer Equation
SBDART	Santa Barbara DISORT Atmospheric Radiative Transfer
SSF	Single Scanner Footprint
sw	Shortwave
swrad	Shortwave radiation
TOA	Top of the atmosphere
trz	Transition zone
UV	Ultraviolet radiation
WRF-ARW	Advanced Research – Weather Research and Forecasting model

Universitat de Girona

List of Abbreviations and Symbols defined/used in chapter 3

term	*description*
λ	Wavelength
Ω	Solid Angle
sr	steradian
θ''	CERES viewing zenith angle
θ'	Scattering angle
θ	Zenithal angle in polar coordinates / CERES viewing zenith angle at surface
ϕ	Azimuthal angle in polar coordinates
$\delta_{ext,\lambda}$	Monochromatic extinction coefficient
$\delta_{abs,\lambda}$	Monochromatic absorption coefficient
$\delta_{sca,\lambda}$	Monochromatic scattering coefficient
ω_λ	Monochromatic single scattering albedo
g_λ	Monochromatic asymmetry factor
τ_λ	Monochromatic optical thickness
μ	cos(θ)
$P_\lambda(\theta')$	Monochromatic Phase function
dA	Element of area
L_λ	Monochromatic radiance
L	Broadband radiance
E_λ	Monochromatic irradiance
E	Broadband irradiance
dL_λ	Change in radiance value
$L_\lambda(0)$	Initial value of radiance
J_λ	Monochromatic source function
dz	Physical thickness of an atmospheric layer
$B_\lambda(T)$	Monochromatic Planck function for temperature T
$\uparrow L_{CERES}$	Instantaneous outgoing broadband longwave radiances observed at TOA by CERES
$\uparrow L_{RTM,clr}$	Simulated upwelling broadband longwave clear-sky radiances at TOA
AOD	Aerosol optical thickness
CERES	Clouds and the Earth's Radiant Energy System
COD	Cloud optical thickness
ERA5	Fifth generation ECMWF reanalysis
FLG	Fu-Liou-Gu radiation parameterization
FOV	Field of view
h_{sat}	Satellite Altitude
$l_{cross\text{-}scan}$	Estimated cross-scan length of the CERES footprints
$l_{along\text{-}scan}$	Estimated along-scan length of the CERES footprints
lw	Longwave
lwrad	Longwave radiation
MODIS	MODerate resolution Imaging Spectroradiometer

MPAS	Model for Prediction Across Scales
MYD03	MODIS geolocation product
MYD04	MODIS Level-2 aerosol product
MYD06	MODIS Level-2 Cloud product
MYD35	MODIS cloud mask
near-IR	Near Infrared
NGO	New Goddard Parameterization
PAR	Photosynthetically active radiation
R_e	Earth Radius
RRTMG	Rapid Radiative Transfer Model for General circulation models parameterization
RTE	Radiative Transfer Equation
SBDART	Santa Barbara DISORT Atmospheric Radiative Transfer
SSF	Single Scanner Footprint
sw	Shortwave
swrad	Shortwave radiation
TOA	Top of the atmosphere
trz	Transition zone
UV	Ultraviolet radiation
WRF-ARW	Advanced Research – Weather Research and Forecasting model

Universitat de Girona

List of Abbreviations and Symbols defined/used in chapter 4

term	*description*
τ	Optical thickness/depth at the band that contains 0.550 μm wavelength
qv	water vapor mixing ratio
irr	Irradiance component (direct, diffuse or total)
par	Parameterization
SSA	Single scattering albedo
ASY	Asymmetry factor
RTE	Radiative Transfer Equation
T	Temperature
t	Total
dir	Direct
dif	Diffuse
E	Broadband shortwave irradiance
RE	Broadband radiative effect on irradiance
$\overline{\mathrm{RE}}$	Mid-range radiative effect
ΔRE	Radiative effect range
RΔRE	Relative radiative effect sensitivity
$\overline{\mathrm{R\Delta RE}}$	Mean relative radiative effect sensitivity
L-a	Comparison between liquid clouds and aerosols
I-a	Comparison between ice clouds and aerosols
WRF-ARW	Advanced Research – Weather Research and Forecasting model
swrad	Shortwave radiation
sw	Shortwave
RRTMG	Rapid Radiative Transfer Model for General circulation models parameterization
NGO	New Goddard Parameterization
FLG	Fu-Liou-Gu radiation parameterization
UV	Ultraviolet radiation
PAR	Photosynthetically active radiation
near-IR	Near Infrared

Universitat de Girona

List of Abbreviations and Symbols defined/used in chapter 5

term	*description*
λ	Wavelength
τ	Optical thickness/depth at the band that contains0.550 μm wavelength
$\downarrow$	Downwelling direction
$\uparrow$	Upwelling direction
top	Top of the atmosphere
bot	Ground surface
δ	Extinction coefficient
ω	Single scattering albedo
g	Asymmetry factor
r_e	Effective radii
irr	Irradiance component (downwelling or upwelling)
par	Parameterization
RTE	Radiative Transfer Equation
E	Broadband longwave irradiance
RE	Broadband radiative effect on irradiance
ΔRE	Radiative effect range
L-a	Comparison between liquid clouds and aerosols
I-a	Comparison between ice clouds and aerosols
WRF-ARW	Advanced Research – Weather Research and Forecasting model
MPAS	Model for Prediction Across Scales
lwrad	Longwave radiation
lw	Longwave
RRTMG	Rapid Radiative Transfer Model for General circulation models parameterization
NGO	New Goddard Parameterization
FLG	Fu-Liou-Gu radiation parameterization
OPAC	Optical Properties of Aerosols and Clouds

Universitat de Girona

List of Abbreviations and Symbols defined/used in chapter 6

term	*description*
θ	CERES viewing zenith angle at surface
ε_{clr}	Difference between the calculated and observed clear-sky upward irradiances
$\bar{\varepsilon}_{clr}$	Bias associated with the simulated clear-sky radiance
r^2	Determination coefficient
dT	Difference between the temperatures at which the emission is performed at top of a parcel of transition zone suspension and sea surface
trz	Transition zone
clr	Clear-sky
$\uparrow L_{CERES}$	Instantaneous outgoing broadband longwave radiances observed at TOA by CERES
$\uparrow L_{RTM,clr}$	Simulated upwelling broadband longwave clear-sky radiances at TOA
AOD	Aerosol Optical Depth
CERES	Clouds and the Earth's Radiant Energy System
COD	Cloud Optical Depth
ERA5	Fifth generation ECMWF reanalysis
FOV	Field of View
MODIS	Moderate Resolution Imaging Spectroradiometer
MYD03	MODIS geolocation product
MYD04	MODIS Level-2 aerosol product
MYD06	MODIS Level-2 Cloud product
MYD35	MODIS cloud mask
RE	Broadband longwave radiative effect on irradiance at TOA
SBDART	Santa Barbara DISORT Atmospheric Radiative Transfer model
SSF	Single Scanner Footprint
TOA	Top of the atmosphere

Universitat de Girona

List of Abbreviations and Symbols defined/used in chapter 7

term	*Description*
τ	Optical thickness/depth at the band that contains 0.550 μm wavelength
δ_{scat}	Extinction coefficient
ω	Single scattering albedo
P(θ')	Phase function
dT	Difference between the temperatures at which the emission is performed at top of a parcel of transition zone suspension and sea surface
CERES	Clouds and the Earth's Radiant Energy System
ERA5	Fifth generation ECMWF reanalysis
FLG	Fu-Liou-Gu radiation parameterization
FOV	Field of View
lw	Longwave
lwrad	Longwave radiation
MFRSR	Multi-Filter Rotating Shadowband Radiometer
MODIS	MODerate resolution Imaging Spectroradiometer
NGO	New Goddard Parameterization
RE	Broadband radiative effect on irradiance
RTE	Radiative Transfer Equation
RRTMG	Rapid Radiative Transfer Model for General circulation models parameterization
SBDART	Santa Barbara DISORT Atmospheric Radiative Transfer
sw	Shortwave
swrad	Shortwave radiation
TOA	Top of the atmosphere
WRF-ARW	Advanced Research – Weather Research and Forecasting model

Universitat de Girona

List of Abbreviations and Symbols defined/used in chapter 8

term	*description*
CERES	Clouds and the Earth's Radiant Energy System
lwrad	Longwave radiation
MODIS	Moderate Resolution Imaging Spectroradiometer
RE	Broadband radiative effect on irradiance
RTE	Radiative Transfer Equation
swrad	Shortwave radiation
TOA	Top of the atmosphere
WRF-ARW	Advanced Research – Weather Research and Forecasting model

Universitat de Girona

Acknowledgements

I would like to kindly thank my PhD thesis supervisors Dr. Josep Calbó and Dr. Josep-Abel González for their continuous and very valuable support during and also before the start of the PhD. I would also like to kindly thank the financial supporters which have made this research possible. Specifically, the Government of Catalunya (Secretaria d'Universitats i Recerca) and European Union for providing the FI-AGAUR PhD grant (grant number: 2018FI_B_00830), and the Spanish Ministry of Economy and Competitiveness and Spanish Ministry of Science and Innovation for funding the projects NUBESOL (CGL2014-55976-R) and NUBESOL-2 (PID2019-105901RB-I00) developed at the Department of Physics of the University of Girona.

Some of the ideas and the methodologies presented in this thesis have been developed during a three-month research stay at the Karlsruhe Institute of Technology - Institute of Photogrammetry and Remote Sensing (KIT-IPF), funded by the FI-AGAUR PhD grant mentioned above. I would like to thank Dr. Jan Cermak and Dr. Hendrik Andersen for hosting me at KIT-IPF and for their valuable scientific assessment to the present thesis.

I would also like to kindly thank Dr. Alex Montornés i Torrecillas for his unsparing technical and scientific assistance. Especially with WRF-ARW model and the shortwave radiative parameterizations included in it.

In addition, I would like to kindly thank the anonymous reviewers for the time they have spent on reviewing this thesis and their constructive and helpful comments, as well as the academic committee at the University of Girona for the efficiency in handling the thesis related administrative matters.

Universitat de Girona

Table of content

Universitat de Girona

List of Figures

Universitat de Girona

List of Tables

Abstract

Aerosols and clouds, as two particular cases of a single phenomenon (i.e., a suspension of particles in the air), are important components in the climate system. They play a crucial role in determination of Earth's energy budget, as they strongly affect the balance between the incoming shortwave solar radiation absorbed by Earth's atmosphere and surface, and the thermal longwave radiation emitted from the Earth. Although aerosols and clouds interact and affect each other's properties, their radiative properties and effects are usually treated separately in climate, meteorological, and weather forecasting studies and models. Thus, a discrimination between the cloudy and noncloudy skies is often required in such contexts. Traditionally, the algorithms used for performing this discrimination assume that the state of the sky is either cloudy or noncloudy (but containing a certain aerosol load), leaving no space for an intermediate phase. However, the change in the state of sky from cloudy to cloudless (or vice versa) occurs gradually, and it comprises an additional phase called "transition zone" (or "twilight zone"), which may represent a variety of atmospheric processes: hydration/dehydration of aerosols, cloud fragments shearing off from the adjacent clouds, decaying and incipient clouds, etc. As a result of this simplified assumption about the state of sky, the area corresponding to the transition zone is often labeled as an area containing optically thin layers of cloud or aerosol. However, the microphysical and radiative

characteristics of the transition zone are expected to lay on the border between those corresponding to a cloud and those corresponding to an atmospheric aerosol. In other words, radiative and optical properties corresponding to clear (noncloudy) or cloudy skies are misleadingly used to characterize such transition zone conditions.

In the present thesis we contribute to the knowledge available about the transition zone from an energy balance perspective. First, we investigated the uncertainties which may arise from neglection of the transition zone (assuming it as cloud or aerosol) in the radiative processes simulated in the models. To this aim, we isolated some of the shortwave and longwave radiative schemes included in the Advanced Research - Weather Research and Forecasting model (WRF-ARW) version 4.0, which allow users to consider different treatments of aerosols and clouds (RRTMG, NewGoddard and FLG) and then utilized them to perform a number of simulations under ideal "cloud" and "aerosol" modes, for different values of (i) cloud optical thicknesses resulting from different sizes of ice crystals or liquid droplets, cloud height, mixing ratios; and (ii) different aerosol optical thicknesses combined with various aerosol types. We found that assuming a situation corresponding to the transition zone as optically thin layers of cloud and aerosol by the radiative parameterizations can indeed introduce substantial uncertainties to the radiative processes simulated by the parameterizations in both shortwave and longwave bands. Based on these simulations we showed that assigning the properties of clouds and aerosol to a transition zone condition producing an optical depth of 0.1 (at 0.550 µm wavelength) can introduce uncertainties up to 27.0 W m^{-2} and 7.2 W m^{-2} to the simulated surface shortwave and longwave irradiances, respectively.

Furthermore, with the aim of understanding the role that the transition zone plays in the determination of the Earth's energy budget, we developed a method for quantifying the transition zone broadband longwave radiative effects at the top of the atmosphere. This method quantifies the transition zone radiative effects over the oceans based on the combination of instantaneous radiative measurements made by MODIS and CERES spaceborne radiometers and radiative transfer simulations. We tested this method using the daytime data recorded by MODIS and CERES instruments onboard Aqua spacecraft during August 2010 over South-East Atlantic Ocean. The results obtained from this analysis showed that this method is capable of detecting the transition zone broadband longwave radiative signature with an accuracy of $\pm$ 3.7 W m^{-2} at a spatial resolution of 20 km at nadir. Worth

mentioning that the transition zone broadband longwave radiative effect for the studied domain and time was on average equal to 8.0 W m^{-2} (heating effect), although cases with radiative effects as large as 50 W m^{-2} were also found.

Resum

Els aerosols i els núvols, com a dos casos particulars d'un mateix fenomen (és a dir, una suspensió de partícules a l'aire), són components importants del sistema climàtic. Tenen un paper crucial en la determinació del balanç energètic de la Terra, ja que afecten fortament l'equilibri entre la radiació solar, d'ona curta, que absorbeixen l'atmosfera i la superfície de la Terra i la radiació tèrmica, d'ona llarga, emesa des de la Terra. Tot i que els aerosols i els núvols interactuen entre ells, modificant uns les característiques dels altres, les seves propietats i efectes radiatius se solen tractar per separat en estudis i models climàtics, meteorològics i de predicció del temps. Per tant, sovint es requereix una discriminació entre el cel serè i el cel ennuvolat. Tradicionalment, els algoritmes utilitzats per realitzar aquesta discriminació suposen que l'estat del cel és o bé ennuvolat o bé serè (sense núvols però que conté una certa càrrega d'aerosol), sense deixar espai per a una fase intermèdia. No obstant això, el canvi de l'estat del cel d'ennuvolat a serè (o viceversa) es produeix gradualment i comprèn una fase addicional anomenada "zona de transició" (o "twilight zone"), que pot representar una varietat de processos atmosfèrics: hidratació / deshidratació d'aerosols, fragments de núvols que sorgeixen dels núvols adjacents, núvols incipients o a punt de desaparèixer, etc. Com a resultat d'aquest supòsit simplificat sobre l'estat del cel, l'àrea corresponent a la zona de transició sovint s'etiqueta com una àrea que conté capes

òpticament primes de núvol o aerosol, tot i que s'espera que les característiques microfísiques i radiatives de la zona de transició es trobin al límit entre les que corresponen a un núvol i les que corresponen a un aerosol atmosfèric. En altres paraules, les propietats òptiques i radiatives corresponents a cel serè (no nuvolós) o ennuvolat s'utilitzen de manera no del tot adequada per caracteritzar les condicions de zones de transició.

En la present tesi contribuïm al coneixement disponible sobre la zona de transició des d'una perspectiva de balanç energètic. En primer lloc, hem investigat les incerteses que poden sorgir pel fet de negligir la zona de transició (suposant-la com a núvol o aerosol) en els processos radiatius simulats en els models. Amb aquest objectiu, vam aïllar alguns dels esquemes radiatius d'ona curta i d'ona llarga inclosos en el model Advanced Research - Weather Research and Forecasting (WRF-ARW) versió 4.0, que permeten als usuaris considerar diferents tractaments d'aerosols i núvols (RRTMG, NewGoddard i FLG) i després els vam utilitzar per realitzar una sèrie de simulacions en modes ideals de "núvol" i "aerosol", per a diferents valors de (i) gruixos òptics de núvol resultants de diferents mides de cristalls de gel o gotes d'aigua, alçada del núvol, i proporcions de barreja; i (ii) diferents gruixos òptics d'aerosol combinats amb diversos tipus d'aerosol. Hem trobat que suposar una situació que correspon a la zona de transició com a capes òpticament primes de núvol o aerosol en les parametritzacions radiatives pot introduir incerteses substancials als processos radiatius simulats per les parametritzacions, tant en bandes d'ona curta com d'ona llarga. Basant-nos en aquestes simulacions, hem demostrat que assignar les propietats dels núvols i de l'aerosol a una condició de zona de transició que produeix una profunditat òptica de 0,1 (a una longitud d'ona de 0,550 μm) pot introduir incerteses de fins a 27,0 W m^{-2} i 7,2 W m^{-2} a la simulació d'irradiància d'ona curta i d'ona llarga en superfície, respectivament.

A més, amb l'objectiu d'entendre el paper que juga la zona de transició en la determinació del balanç energètic de la Terra, vam desenvolupar un mètode per quantificar els efectes radiatius, en la banda d'ona llarga, de la zona de transició, a la part superior de l'atmosfera. Aquest mètode quantifica els efectes radiatius de la zona de transició basant-se en la combinació de mesures radiatives instantànies realitzades pels radiòmetres MODIS i CERES, que es troben a bord de satèl·lits, sobre els oceans i en simulacions de transferència radiativa. Hem provat aquest mètode utilitzant les dades diàries enregistrades pels instruments MODIS i CERES a bord de la sonda espacial Aqua durant l'agost de 2010 al sud-est de l'oceà Atlàntic.

Els resultats obtinguts d'aquesta anàlisi han mostrat que aquest mètode és capaç de detectar l'empremta radiativa de la zona de transició en ona llarga de banda ampla amb una precisió de $\pm$ 3,7 W m^{-2} a una resolució espacial de 20 km al nadir. Val a dir que l'efecte radiatiu de la zona de transició en ona llarga de banda ampla , per al domini i el temps estudiats, presentava un valor mitjà de 8,0 W m^{-2} (efecte escalfador), tot i que també es van trobar casos amb efectes radiatius de fins a 50 W m^{-2}.

Resumen

Los aerosoles y las nubes, como dos casos particulares de un mismo fenómeno (es decir, una suspensión de partículas en el aire), son componentes importantes del sistema climático. Desempeñan un papel crucial en la determinación del balance energético de la Tierra, ya que afectan en gran medida el equilibrio entre la radiación solar de onda corta entrante absorbida por la atmósfera y la superficie de la Tierra y la radiación térmica de onda larga emitida desde la Tierra. Aunque los aerosoles y las nubes interactúan entre ellos y afectan las características respectivas, sus propiedades y efectos radiativos suelen tratarse por separado en los estudios y modelos climáticos, meteorológicos y de predicción del tiempo. Por lo tanto, a menudo se requiere una discriminación entre los cielos nublados y despejados en tales contextos. Tradicionalmente, los algoritmos utilizados para realizar esta discriminación asumen que el estado del cielo es nublado o despejado (sin nubes pero que contiene una cierta carga de aerosol), sin dejar espacio para una fase intermedia. Sin embargo, el cambio en el estado del cielo de nublado a despejado (o viceversa) ocurre gradualmente y comprende una fase adicional llamada "zona de transición" (o "twilight zone"), que puede representar una variedad de procesos atmosféricos: hidratación / deshidratación de aerosoles, fragmentos de nubes desprendiéndose de las nubes adyacentes, nubes incipientes o en disolución, etc. Como resultado de esta simplificación sobre el estado del cielo, el área correspondiente a la

zona de transición a menudo se etiqueta como un área que contiene capas ópticamente delgadas de nubes o aerosoles, aunque se espera que las características microfísicas y radiativas de la zona de transición se encuentren en el límite entre las correspondientes a una nube y las correspondientes a un aerosol atmosférico. En otras palabras, las propiedades radiativas y ópticas correspondientes a cielos despejados (no nublados) o nublados se utilizan de forma no del todo adecuada para caracterizar las condiciones de las zonas de transición.

En la presente tesis contribuimos al conocimiento disponible sobre la zona de transición desde una perspectiva de balance energético. Primero, hemos investigado las incertidumbres que pueden surgir de negligir la zona de transición (asumiéndola como nube o aerosol) en los procesos radiativos simulados en los modelos. Para ello, aislamos algunos de los esquemas radiativos de onda corta y onda larga incluidos en el modelo Advanced Research - Weather Research and Forecasting (WRF-ARW) versión 4.0, que permiten a los usuarios considerar diferentes tratamientos de aerosoles y nubes (RRTMG, NewGoddard y FLG). A continuación, los utilizamos para realizar una serie de simulaciones en modos ideales de “nube” y “aerosol”, para diferentes valores de (i) espesores ópticos de las nubes resultantes de diferentes tamaños de cristales de hielo o gotas de agua, altura de las nubes, proporciones de mezcla; y (ii) diferentes espesores ópticos de aerosoles combinados con varios tipos de aerosoles. Hemos obtenido que asumir una situación correspondiente a la zona de transición como capas ópticamente delgadas de nubes y aerosoles por las parametrizaciones radiativas puede introducir incertidumbres sustanciales en los procesos radiativos simulados por las parametrizaciones en las bandas de onda corta y larga. Basándonos en estas simulaciones, hemos mostrado que asignar las propiedades de las nubes y el aerosol a una condición de zona de transición que produce una profundidad óptica de 0,1 (a una longitud de onda de 0,550 µm) puede introducir incertidumbres de hasta 27,0 W m^{-2} y 7,2 W m^{-2} en las irradiancias simuladas en superficie, de onda corta y onda larga, respectivamente.

Además, con el objetivo de comprender el papel que juega la zona de transición en la determinación del balance energético de la Tierra, desarrollamos un método para cuantificar los efectos radiativos de onda larga de banda ancha de la zona de transición en la parte superior de la atmósfera. Este método cuantifica los efectos radiativos de la zona de transición basándose en la combinación de medidas radiativas instantáneas realizadas por los radiómetros MODIS y CERES, situados a bordo de satélites, sobre los océanos y en

simulaciones de transferencia radiativa. Probamos este método utilizando los datos diurnos registrados por los instrumentos MODIS y CERES a bordo de la nave espacial Aqua durante agosto de 2010 sobre el Océano Atlántico Suroriental. Los resultados obtenidos de este análisis mostraron que este método es capaz de detectar la huella radiativa de la zona de transición, en la onda larga de banda ancha, con una precisión de $\pm$ 3,7 W m^{-2} a una resolución espacial de 20 km en el nadir. Cabe mencionar que el efecto radiativo de la zona de transición en onda larga de banda ancha, para el dominio y tiempo estudiados, fue en promedio igual a 8.0 W m^{-2} (efecto de calentamiento), aunque también se encontraron casos con efectos radiativos tan grandes como 50 W m^{-2}.

Chapter 1
Introduction

Background

The balance between the incoming shortwave solar radiation (typically referred to as radiation at wavelengths shorter than 4.0 μm) absorbed by Earth's atmosphere and surface, and the thermal longwave radiation (typically referred to as radiation at wavelengths longer than 4.0 μm) emitted from the Earth to the space is the driving force behind weather, climate, and even life on the planet Earth. Indeed, this is the energy responsible for maintaining the atmosphere's overall temperature structure, including the horizontal gradients that drive atmospheric circulations, as well as the vertical gradients that dominate in the convection and therefore in most of the water cycle. There are a number of factors contributing to the determination of Earth's energy budget as well as its distribution across the globe, including the amount of solar radiation arriving to the top of Earth's atmosphere, the amount of longwave radiation emitted by the Earth's surface and interactions of atmosphere with radiation in both longwave and shortwave bands. The focus of this research is on the effects of the atmosphere on radiation under the conditions that we call "transition zone".

1.1 Radiative Processes in the Atmosphere

Earth's atmosphere contains suspended particles with a wide range of characteristics, which have, due to their size, terminal fall velocities of the order of centimeters per second at most, so they have atmospheric residence times on the order of hours, days, or even longer in some cases. Despite their small mass, or volume fraction, particles in the atmosphere strongly affect the transfer of energy as well as its spatial distribution in the atmosphere, thus affecting the weather at any moment and climate in the long term.

As the radiation travels through the Earth's atmosphere, it gets *attenuated* (or *extinguished*) and redistributed due to interaction with the suspended particles. The attenuation occurs through *absorption* and *scattering* mechanisms. Absorption of radiation increases the internal energy of the particles and heats them up. Then, they exchange this energy with their surrounding environment through *emission*. On the other hand, scattering deviates radiation from its initial path without changing its energy content (frequency remains unchanged). The scattered radiation, which is referred to as *diffuse radiation*, continues to interact with atmospheric components until it is totally absorbed, reaches the surface, or escapes to the space.

The rate at which absorption, scattering and emission is performed in an atmospheric layer depends on the radiative properties of the particles interacting with radiation, which are the result of their chemical and physical characteristics, such as chemical composition, size, concentration, geometric shape, etc. Figure 1.1 shows the relationship between radius and scattering behavior for spherical particles in interaction with monochromatic radiation. The horizontal and vertical axis in this figure show the wavelength (λ) and radius of the particle (r), respectively. The dashed lines also show the *size parameter* (X, dimensionless) for the threshold between different *scattering regimes*. It is defined as

$$X=2\pi r/\lambda \qquad \textit{Eq. 1.1}$$

In the case of non-spherical particles, r might represent the radius of a sphere having the same volume or surface area, depending on the context.

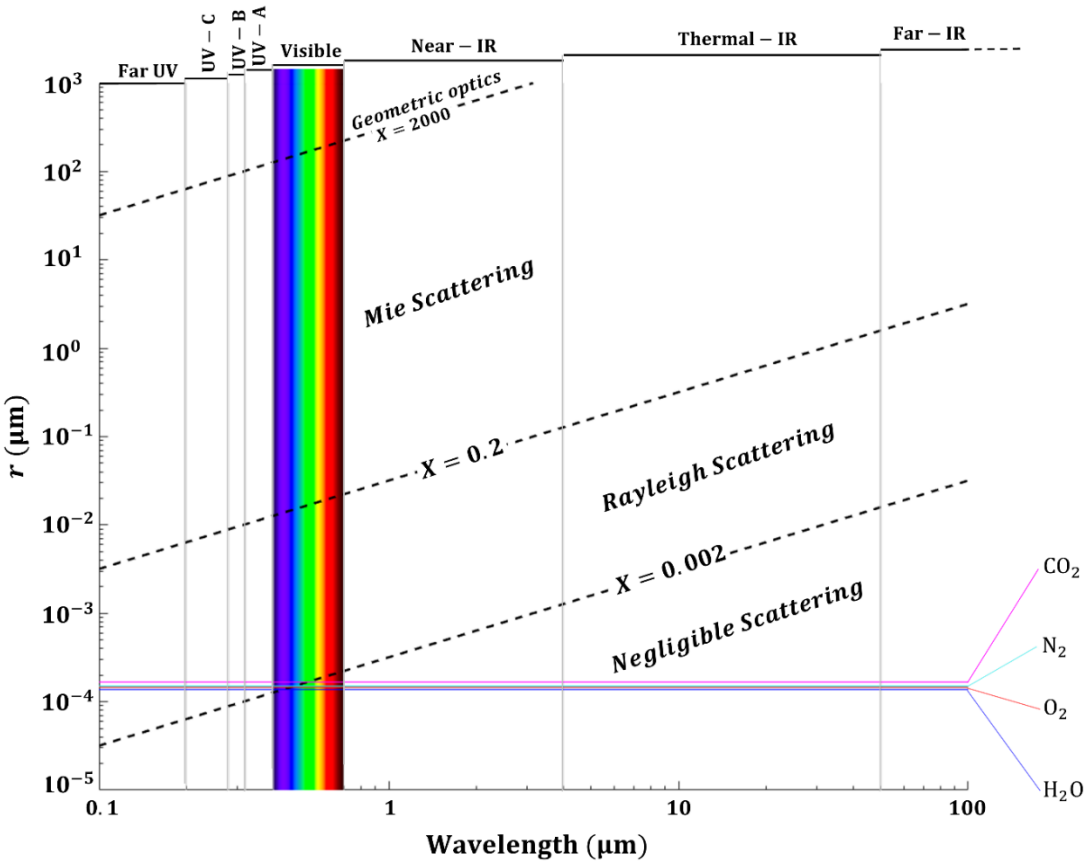

Figure 1.1. Relationship between particle radius (r), radiation wavelength (λ) and scattering behavior for atmospheric particles. The dashed lines represent rough boundaries between scattering regimes. The colored lines indicate the radius of the CO2, N2, O2 and H2O molecules. (Source: own elaboration with inspiration from Petty, 1958).

From Figure 1.1, it can be seen that scattering is negligible for the values of *X* less than 0.002, meaning that the interaction of radiation with particles with sizes way smaller than the wavelength, is limited, if any, to absorption and emission. This is the case of a number of atmospheric molecules (e.g. CO_2, N_2, O_2 and H_2O) for wavelengths longer than 0.5 µm. Indeed, the Rayleigh scattering effect performed by atmospheric gases (basically N_2 and O_2) at shorter visible wavelengths is responsible for the blue color of a clear sky. Whereas for *X* values between 0.002-0.2 and 0.2-2000, scattering is performed according to the *Rayleigh* and *Mie* Scattering regimes, respectively (Bohren & Huffman, 1998).

It is indeed the magnitude of the radiative transfer processes occurring in parallel at different levels of the atmosphere and at various locations that shapes the thermal structure and hence, the dynamics of the atmosphere. For this reason, it is required to quantify the radiative transfer processes in the atmospheric models and a number of meteorological/climate studies. An accurate quantification of radiative transfer processes in the atmosphere requires

addressing the interactions of radiation with the particles separately and in detail. Doing so, eventually requires discriminating particles from each other. That is because different particles interact differently with radiation, as they have different chemical and physical characteristics. However, the size, concentration and composition of the particles vary in time and location, thus discrimination among them can sometimes be quite challenging. Specifically, some types of particles are well mixed in the atmosphere, and thus their concentration and size can be well approximated (this is the case of atmospheric gases such as N_2, O_2, and CO_2,). Whereas there exist some other gases such as water vapor and other types of particles that constitute clouds and atmospheric aerosols (aerosols in short) that are highly variable in location and time, which makes it quite challenging to address their interaction with radiation.

1.2 Clouds and Aerosols

Clouds and aerosol are the particular names for two specific particle suspensions in the atmosphere which play a key role in determination of Earth's energy budget. They both may cool down the atmosphere through reflecting (backscattering) some fraction of the incoming shortwave solar radiation back to space (cooling effect), but also keep it warm through absorbing the upwelling longwave terrestrial radiation (heating effect) and re-emitting some proportion of the radiation absorbed in both upwelling and downwelling directions. Clouds of different types cover at any moment a vast area of the planet and aerosols exist in the air with various concentrations under all sky conditions. Characteristics of both clouds and aerosols are indeed highly variable in time and space and any changes occurring in their concentration, distribution and composition strongly affects transmissivity of the atmosphere, which eventually affects the amount of energy absorbed by the Earth's atmosphere and surface and how this energy is distributed. The fact that clouds are responsible for 25% out of the total 30% terrestrial global albedo is an evidence showing the great role that the clouds play in the determination of Earth's energy budget (Wild et al., 2013). Also, the dimming and brightening (widespread decrease/increase observed in the downwelling solar radiation) phenomenon is a major source of evidence showing how strongly the aerosols influence Earth's energy budget (Mateos et al., 2014; Wild et al., 2005). In this section, we explain what the names aerosol and cloud refer to.

Atmospheric aerosol is a suspension of particles in the atmosphere with a wide range of compositions, size distributions and characteristics, which may be present in liquid, solid or mixed phases. These particles may be from natural sources such as sea spray, dust storms, volcanoes, and wildfires, as well as from anthropogenic sources such as biomass burning, mining, industrial and agricultural activities, fossil fuel burning, etc. In addition, an aerosol can be directly emitted to the atmosphere (primary aerosols) or produced in the atmosphere from precursor gases (secondary aerosols).

When the thermodynamic conditions of a volume of air (which eventually contains a certain load of aerosol particles) change and it reaches saturation/supersaturation levels, the aerosol particles within it gets humidified and their size grows, as the molecules of water vapor condense on them (Spiridonov & Ćurić, 2021). This process is referred to as aerosol activation, and eventually leads to formation of liquid droplets and ice crystals (Rejano et al., 2021). According to the World Meteorological Organization, a cloud is a hydrometeor consisting of a suspension in the atmosphere of such tiny particles of liquid water or ice, or both, and usually not touching the ground (International Cloud Atlas, Definition of Cloud: https://cloudatlas.wmo.int/en/definition-of-a-cloud.html, last access: 18 August 2021). It may also include particles of liquid water or ice of larger dimensions, as well as non-aqueous liquid particles or solid particles originating, for example, from industrial vapors, smoke or dust. This process is schematically explained in Figure 1.2. The meteorological conditions as well as the characteristics and compositions of the aerosols serving as the cloud condensation nuclei drive the cloud droplet/crystal number concentration and size distribution, cloud liquid water content, and cloud albedo, which altogether control the magnitude of the cloud-radiation interactions (Abdul-Razzak & Ghan, 2002; Kanji et al., 2017).

However, although according to abovementioned explanations clouds and aerosols are both essentially suspended particles in the air and components of a coupled system, they are identified with different names and very often studied separately. This is because humidification and activation of aerosols strongly changes their physical characteristics such as shape, composition and size and so does their optical properties (some links between the physical and optical properties of the particles are explained in section 1.1). These changes are so significant that after *some certain threshold* the characteristics of the suspension become totally distinct that we no longer identify the suspension as aerosol, but rather as

cloud. For this reason, they are often discriminated from each other in climate, meteorological and weather forecasting studies. Further explanations about these mechanisms can be found in some relevant text books (Ahrens, 2009; Houghton, 1985).

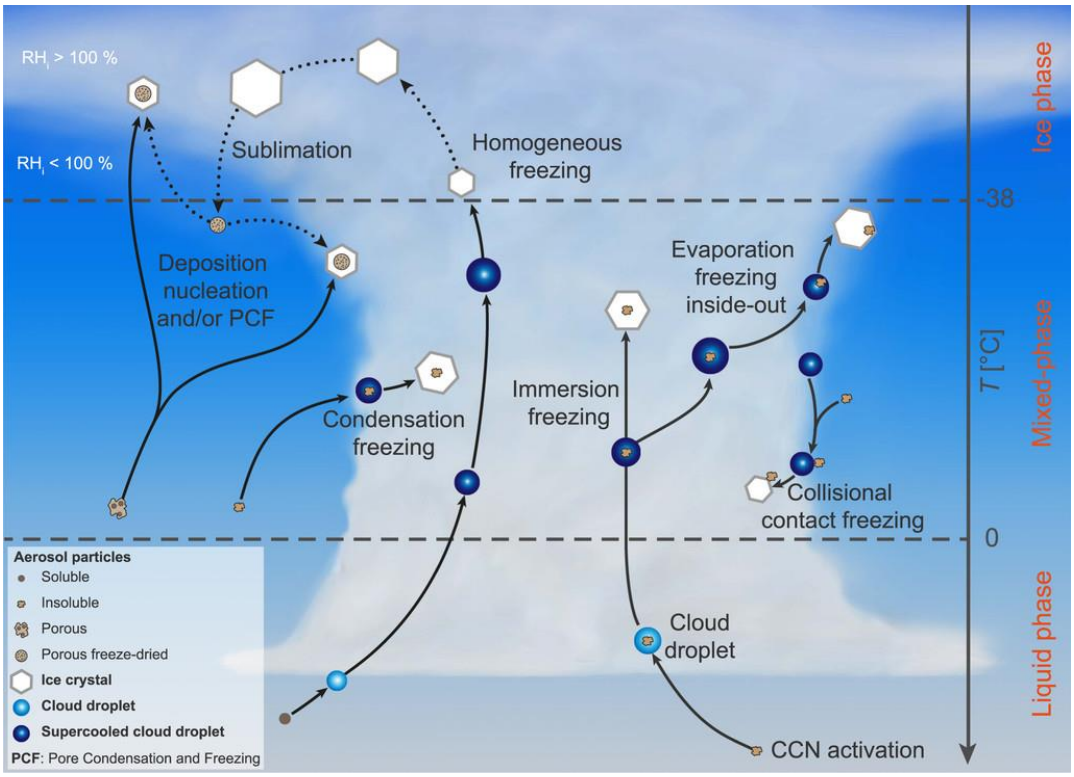

Figure 1.2. Schematic description of aerosol activation and cloud formation processes. Source: © American Meteorological Society (Kanji et al., 2017). Used with permission.

1.3 Cloud-Aerosol Discrimination

As mentioned in section 1.2, clouds and aerosols have distinct characteristics which make them different from each other and as a result of these differences, they interact differently with the radiation and have different effects on the dynamics of the atmosphere (they are also indicators of different atmospheric/climate processes). For this reason, it is often required to discriminate them from one another in meteorological, climate and atmospheric studies and models. To discriminating clouds and aerosols from each other, a number of methods, usually referred to as "*cloud-screening*" and "*cloud-masking*" algorithms, have been developed to this date. In these methods, in general the discrimination is performed on the basis of the differences in features expected from clouds and aerosols. For example, clouds are easily seen, and they are a ubiquitous natural phenomenon (in most of the occasions, they can be easily seen with the naked human eye, at least in the daytime). As well, clouds particles are larger in size and contain more water compared to aerosols. On the other hand, aerosols

are better mixed in the atmosphere and appear with lower mass mixing ratios compared to clouds. Also, in interaction with radiation in both shortwave and longwave bands, they usually leave different, yet unique monochromatic and broadband radiative signatures (as they have different optical properties).

Generally speaking, cloud-screening methods seek for detectable clouds in the sky based on some criteria and, if the conditions of the criteria are fulfilled, the method defines the state of sky as "*cloudy*", and if not as "*cloud-free*" (or "*clear*"). The areas labeled as cloud-free are assumed to contain some certain load of aerosol and for this reason the observations made for these regions are assigned to aerosols, accordingly those of cloudy regions are assigned to clouds. Then, based on radiative measurements, the optical and microphysical properties of the clouds and aerosols may be retrieved.

For example, the broadband downwelling longwave radiation recorded at surface under cloudy conditions is expected to be greater than that measured under clear-sky. On the basis of this principle, a cloud-screening method was developed for pyrgeometers which measure the broadband and hemispherically integrated downwelling longwave radiation at a certain point on the Earth's surface (Dürr & Philipona, 2004). Specifically, in this method, the ratio of the apparent emittance of the sky to the expected apparent cloud-free emittance (so-called the cloud-free index) is calculated and a cloud-free index greater than 1 would imply a cloudy condition. Also, on the basis of the absolute values and the temporal variability of shortwave (solar) irradiances (direct, diffuse and total) measured at surface by broadband pyrometers calculation of downwelling shortwave cloud effects, Long & Ackerman (2000) developed a cloud-screening method to discriminate the recorded signals that potentially correspond to the clouds from those corresponding to the cloud-free regions. The idea behind this method is that clouds tend to cause a higher temporal variability in the recorded signals compared to aerosols and also that clouds tend to attenuate more strongly compared with aerosols. For the Multi-Filter Rotating Shadowband Radiometer (Harrison & Michalsky, 1994; MFRSR; an instrument making point measurements of direct, diffuse and total surface irradiances at narrow-band channels, which derives optical depth at different wavelengths under all sky conditions), temporal variability in the optical depth measurement is the cloud-screening criteria (Michalsky et al., 2010). In case of sky cameras, which see the entire 180° sky view from a particular point at the surface, it is often a threshold in one or several parameters

derived for one single pixel (Calbó & Sabburg, 2008; Kazantzidis et al., 2012; Long et al., 2006). For MODIS (MODerate resolution Imaging Spectroradiometer) instrument, which is an imager instrument installed on Aqua and Terra spacecrafts with 36 narrow-band channels, the cloud-masking criteria is the spatial variability of the signals received at the time of observation (Ackerman et al., 2010; Ackerman & Frey, 2015; Frey et al., 2008), which is in a sense similar to the criteria considered for using MFRSR (variability of signal at fixed location over time). These were examples of "*passive*" remote-sensing instruments. They are called passive because they detect natural energy that is reflected, scattered, or emitted from the observed scene.

There exist also instruments referred to as "*active*" remote-sensing instruments, that provide their own energy (electromagnetic radiation) to illuminate the object or scene they observe. They send a pulse of energy from the sensor to the object (at a single or multiple wavelengths) and then receive the radiation that is reflected or backscattered from that object. Then, based on the intensity and/or polarization of the reflected or backscattered radiation, they identify the cloud particles. Radars (Radio Detection and Ranging), lidars (Light Detection and Ranging) and ceilometers are examples of active remote-sensing instruments (Luke et al., 2010; Marchand et al., 2008; Martucci et al., 2010; Vaughan et al., 2009). CALIPSO (Cloud-Aerosol Lidar and Infrared Pathfinder Satellite Observations), for example, is a two-wavelength polarization ratio-sensitive backscatter spaceborne lidar. This instrument sends laser pulses at a water vapor absorptive and a non-water absorptive narrow-bands, centered at 1.064 μm and 0.532 μm wavelengths respectively, and then measures the extinction-to-backscatter ratio (in the lidar community, extinction-to-backscatter ratio is commonly referred to as the "lidar ratio"). The cloud-screening algorithm developed for this instrument is based on the principle that clouds contain high amount of water vapor which strongly absorbs radiation at 1.064 μm and thus the lidar ratio at this band becomes infinity. Then, based on the principle that ice particles tend to scatter radiation at 0.532 μm wavelength in forward direction more strongly than the droplets, they further classify the clouds to ice and liquid clouds (Liu et al., 2009; Trepte, 2021).

Here we should state that the sky classified as cloudy by one method or instrument can be labeled as cloud-free by another, even if we are comparing the best screening methods. Because, depending on the characteristics of instrumentation used (such as spectral, spatial

and temporal resolution) and the platform the instrumentations are operated at (Earth surface, satellite, airplane, drone, balloon, etc.), the criteria applied for considering a suspension as cloud can be different. More importantly, regardless of the cloud-screening method used, classification of the sky condition as cloudy or cloud-free will eventually require considering some thresholds, and the decision about these thresholds is rather subjective and finally can depend on human criterium. The underlaying cause is that the definition provided for cloud (see section 1.2) is not very clear and does not specify the limits between the characteristics of cloudy and cloud-free regions. In other words, the definition of cloud does not provide quantitative information about "*thresholds*" between the characteristics of clouds and cloud-free atmosphere (i.e., aerosols). For example, it does not specify what should be the size of particles to name them droplets/crystals, what should be concentrations of droplets/crystal to call them a cloud, and many other similar questions such as what does the statement "visible to the human eye" mean? Visible from what distance? Visible based on average human sight? Visible to naked human eye or to human eye inspecting some kind of images or measurements? The study performed by Calbó et al. (2017), describes how the decision made about the quantitative thresholds applied in cloud-screening methods can affect the final outcome of the cloud-screening process.

Another very important reason is the fact that the state of sky is traditionally classified into these two classes (i.e. cloudy and cloud-free), whereas there exists situations for which neither of the statements can be strictly true. Discussion about such situations is provided in the next section.

1.4 Transition Zone

Cloud formation is indeed a continuous and gradual process (see section 1.2) comprising an additional phase of a particle suspension that tends to be called the "*transition zone*" (also known as "*Twilight Zone*") at which the characteristics of the suspension are in "*transition*" between those corresponding to the adjacent clouds and aerosols (Koren et al., 2007). However, the transition zone particle suspension is often neglected and considered as an area containing either optically thin clouds or aerosols in atmospheric, climate and weather studies. This is because in such studies the state of sky is assumed to be either cloudy or cloud-free, leaving no space for any condition in between. Thus, regardless of the instrumentation used and the thresholds considered in the cloud-screening methods applied, the observed

transition zone properties are assigned to clouds or aerosols. Similarly, in the weather and climate models, the characteristics of the clouds and aerosols are used to define the interactions of radiation with the transition zone particle suspension.

The transition zone may correspond to different processes such as hydration and dehydration of aerosols, cloud fragments shearing off from the adjacent clouds, decaying and incipient clouds, pockets of high humidity oscillating near saturation, clouds which have formed but yet not yet visible, etc. (Koren et al., 2009). It has been found that at any time, between 30 and 60% of the sky categorized as cloud-free/clear could potentially contain particle suspension with characteristics of the transition zone (Bar-Or et al., 2011; Koren et al., 2007). Wollner et al. (2014) also observed evidence confirming the existence of large particles which are likely to be ice crystals in the areas around the cloud-free regions extending up to 5.5 km away from the closest detectable cirrus cloud field. Nevertheless, the areas considered to contain optically thin clouds could also correspond to the transition zone conditions, as no matter where the threshold between the cloudy and cloud-free sky is put, the area corresponding to the transition zone will be categorized as optically thin layers of cloud or aerosols (Fuchs & Cermak, 2015). On the basis of the measurements made by the CALIPSO instrument, Várnai & Marshak (2011) also concluded that transition zone may expand up to tens of kilometers away from the cloud field. Calbó et al. (2017) quantified that the frequency of the transition zone is about 10%, on the basis of three ground-based observation methods (broadband shortwave measurements, MFRSR optical depth retrievals and total sky imager observations) at two mid-latitude sites (Girona, Spain and Boulder, Colorado, US). They also found that the transition zone produces typically an optical depth of less than 0.32 (at 0.500 µm wavelength), but it might be found, at those sites, for optical depth as high as 2.00. Schwarz et al. (2017) proposed a method for identification of transition zone conditions based on narrow-band top of the atmosphere radiance measured by MODIS instrument. They applied this method to the entire global August and January records of this instrument onboard Aqua spacecraft over the oceans between 2007 and 2011 and suggests a frequency of 20% for the occurrence of the transition zone.

The abovementioned literature underlines the fact that a significant proportion of sky at any time is covered by a particle suspension with characteristics of the transition zone, and that the transition zone particle suspension could play an important role in the determination of

Earth's energy budget. Based upon an observational and statistical study, Eytan et al. (2020) estimated the top of the atmosphere (TOA) radiative effect of the transition zone around shallow warm clouds in the atmospheric window region (8.4-12.2 μm). They found that over the oceans on average the transition zone radiative effect in the mentioned spectral region is about 0.75 W m^{-2} (although they found cases with average radiative effects as large as 4 W m^{-2}), which is equal to the radiative forcing resulting from increasing atmospheric CO_2 by 75 ppm. The overall radiative effects of the transition zone are likely to be higher, as the radiative effect estimations given in this study correspond to a lower bound of the effect and are limited to the low-level (warm) transition zone conditions. These results obtained from this study along with those stating that the vast area that could potentially correspond to transition zone particle suspension show that transition zone is an important phase of particle suspension in the atmosphere, which requires to be further characterized, studied and if eventually possible, considered in climate/meteorological/atmospheric studies and models as an additional phase of particle suspension.

Chapter 2
Goals and Objectives

The Question

Although the area that potentially may contain transition zone particle suspension is vast, the transition zone is often neglected in climatic, meteorological, and atmospheric related studies. For example, the radiative schemes included in the atmospheric, meteorological and climate models quantify the radiative processes that occur at different levels of the atmosphere assuming the particle suspension is either a cloud particle (ice or liquid) or an atmospheric aerosol, although sometimes a mixture of both is allowed. Similarly, the cloud-screening algorithms are also developed on the basis of the same dichotomic principle. Such treatment of the transition zone and the considerable frequency of its occurrence rises questions such as: “How different the simulated radiative effects in a grid cell of a meteorological/weather forecasting model will be, if a situation corresponding to transition zone is assumed as cloud or aerosol?”, “What are the actual radiative effects of the transition zone?”, “Is it possible to detect radiative signature of the transition zone conditions in coarse-scale measurements?”.

Goals and Objectives

The main goal of the present thesis is to contribute to the knowledge available about the climate system from an energy budget perspective by enriching the information available about the transition zone radiative effects and their representation in the atmospheric models. Within the frame of this goal, the specific objectives of the thesis consist of:

- Analyzing the uncertainties which may arise from neglection of the transition zone in the radiative transfer processes simulated by the radiative schemes included in a meteorological model. In other words, we aim to analyze to what extent assuming a situation corresponding to the transition zone as optically thin layers of cloud or aerosol could be introducing a bias to the radiative processes simulated by a meteorological model.

- Estimating the actual transition zone broadband radiative forcing (effect), which will involve developing methods for detection of transition zone conditions on the basis of the radiative measurements performed by multiple spaceborne and/or surface radiometers.

This research has been conducted within the frame of the projects NUBESOL (CGL2014-55976-R) and NUBESOL-2 (PID2019-105901RB-I00) developed at the Department of Physics of the University of Girona and funded by the Spanish Ministry of Economy and Competitiveness and Spanish Ministry of Science and Innovation, respectively. The overall aim of these projects is to contribute to increasing information about the clouds, aerosols and the situations that lay just in the transition ("border") between a cloud and an aerosol, which can lead to a reduction in the uncertainties associated with the estimates of the Earth's energy budget. More specific information about the objectives of these projects can be found in the descriptions given for these projects on the research group's website at *https://sites.google.com/campus.udg.edu/nuclierprojects/nuclier?authuser=0*.

Chapter 3
Methods

Preview

In chapters 4 and 5 of this thesis, we investigate uncertainties which may arise from neglection of the transition zone in the radiative transfer processes simulated by the radiative schemes included in a meteorological model. To this aim, in these sections we isolate some shortwave and longwave radiation parameterizations included in Advanced Research Weather Research and Forecasting model Version 4.0 (WRF-ARW) from the main model structure. Specifically, those which allow users to consider different treatments of clouds and aerosol. Then, we adapt these parameterizations for one-dimensional vertical simulations ("sandbox" approach; for more information about this approach refer to (Montornès, 2017) and use them to perform several idealized simulations under ideal "clear-sky", "cloud" and "aerosol" modes, as the basis of a sensitivity analysis. Afterwards, based on the results obtained from the sensitivity analysis, we quantify the uncertainties risen from different treatments of the transition zone (i.e., from using the properties of clouds or/and aerosols to describe it). Later, in chapter 6 we investigate the feasibility of quantifying the actual radiative signature (radiative effects) of the transition zone at the top of the atmosphere based on instantaneous radiative measurements made by spaceborne radiometers. Specifically, in this

chapter we combine different products of MODIS radiometer with that of CERES (Clouds and the Earth's Radiant Energy System), Fifth generation ECMWF reanalysis (ERA5) products and radiative transfer simulation for identification of large scale horizontally homogeneous transition zone conditions and quantifying the radiative effects associated with them. Detailed information about the methodology adopted and the data utilized for performing each individual research is given in the corresponding chapters. However, in the following sections of the current chapter we provide some general information about the methods applied and data utilized along this thesis and also give a short introduction to some concepts such as the radiative transfer in a plane-parallel atmosphere, radiance and irradiance, and the sandbox approach applied in the next chapters.

3.1 Radiance and Irradiance

Radiance and irradiance are two important terms in the field of radiative transfer. But before talking about the radiance and irradiance, we will first need to define the concept of solid angle (Ω). It is a measure of the amount of the field of view from some particular point that a given object covers. In the International System of Units Ω is quantified in terms of steradian (sr). For a sphere whose surface area is $4\pi r^2$, its solid angle (from any internal point) is 4π sr. A differential solid angle ($d\Omega$) in a polar coordinates system can be expressed as

$$d\Omega = sin(\theta)\, d\theta\, d\varphi \qquad \textit{Eq. 3.1}$$

where θ and ϕ are the zenithal and azimuthal angles in polar coordinates, respectively. Figure 3.1 illustrates a $d\Omega$ and its representation in polar coordinates.

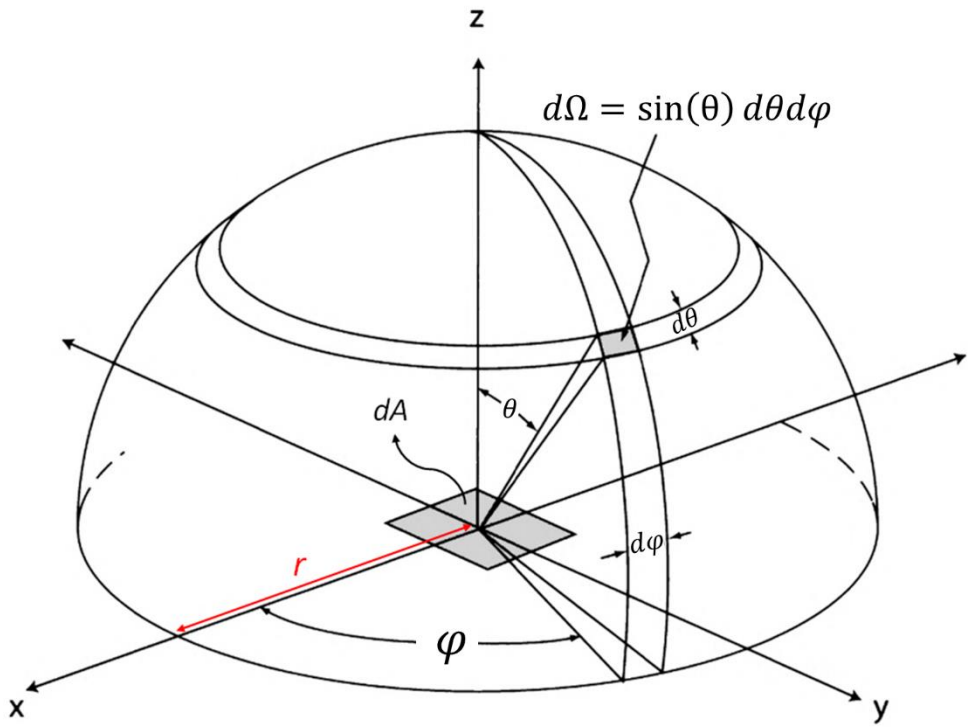

Figure 3.1. Illustration of a differential solid angle ($d\Omega$) and its representation in polar coordinates (source: *Petty, 1958* with slight modifications).

The amount of radiant energy (radiation) crossing an element of area (dA) in a time interval dt, in a specific wavelength interval $d\lambda$ in directions confined to a $d\Omega$ which is oriented at an angle θ to the normal of dA is referred to as "*monochromatic radiance*" (L_λ, W m^{-2} μm^{-1} sr^{-1}). Thus, L_λ implies a directionality in the radiation stream and for this reason it is a function of θ and ϕ. The integration of the normal component of L_λ (with respect the considered surface,

e.g. horizontal) over some range of directions yields *"monochromatic irradiance"* (E_λ, W m^{-2} μm^{-1}). In case of the upwelling (downwelling) irradiances, the integration of radiance should be made over the 2π sr of solid angle corresponding to the upper (lower) hemisphere, and for the net irradiance (sum of downwelling and upwelling irradiances), the integration should be made over the entire spherical solid angle (4π sr). Thus, in polar coordinates, E_λ in upward direction can be computed as shown in Eq. 3.2 (E_λ in the downward direction can be written the same as the upward component except for including a negative sign behind the integrals).

$$E_\lambda = \int_0^{2\pi} \int_0^{\pi/2} L_\lambda(\theta, \varphi) \cos(\theta) \sin(\theta)\, d\theta d\varphi \qquad \textit{Eq. 3.2}$$

From this equation it can be inferred that for upward/downward isotropic radiation (if the magnitude of radiant energy is independent of the direction), the magnitude of E_λ equals L_λ multiplied by π.

Along this thesis we also talk about *broadband radiance, L(θ,φ) and irradiance, E*. *L(θ,φ)* (or *E*) is the total value of $L_\lambda(\theta,\varphi)$ (E_λ) for all wavelengths over some extended spectral range [λ_1, λ_2]. Thus, *L* and *E* can be obtained by integrating $L_\lambda(\theta,\varphi)$ and E_λ over the extended range of wavelength [λ_1, λ_2], according to Eqs 3.3 and 3.4:

$$L\,(\theta, \varphi) = \int_{\lambda_1}^{\lambda_2} L_\lambda(\theta, \varphi)\, d\lambda \qquad \textit{Eq. 3.3}$$

$$E = \int_{\lambda_1}^{\lambda_2} E_\lambda\, d\lambda \qquad \textit{Eq. 3.4}$$

3.2 Radiative Transfer in Plane-Parallel Atmosphere

Plane parallel is an approximation (atmosphere model) used in many radiation models for addressing the radiative processes in the atmosphere. In this approach, the atmosphere is assumed to be only one-dimensional and bounded at the top and bottom by horizontal plane surfaces. In the plane parallel atmosphere, the horizontal variations in the structure of the atmosphere are ignored and all relevant radiative properties depend strictly on the vertical coordinate.

Imagine an atmospheric layer with a physical thickness of *dz* in a plane-parallel atmosphere as illustrated in Figure 3.2. As described in chapter 1, when L_λ passes through an atmospheric element, its magnitude changes. The magnitude of this change (dL_λ) depends on the initial

magnitude of the incident L_λ and the characteristics of the particles (including gas molecules) within the atmospheric element.

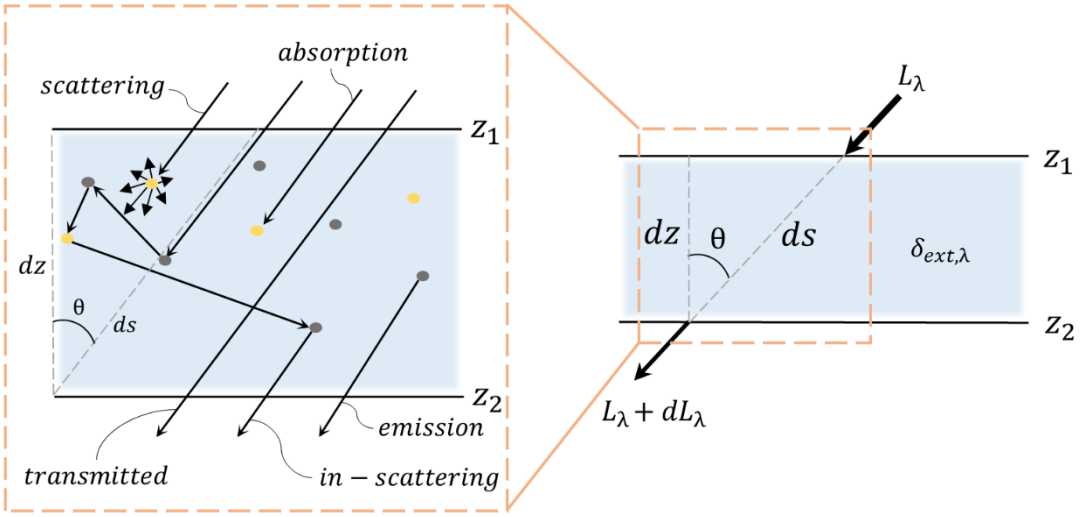

Figure 3.2. Schematic illustration of the radiance (L_λ) with an initial value of $L_\lambda(0)$ passing through an atmospheric element with a physical thickness equal to *dz* with an inclination (to the upward normal) angle of θ (note: $ds = dz / \cos(\theta)$). (Source: own elaboration)

According to Liou (1980), the rate of attenuation for the L_λ passing through this layer with an inclination (to the upward normal) angle equal to θ (Figure 3.2) can be written as

$$dL_\lambda = -\delta_{ext,\lambda} L_\lambda \, ds \qquad \textit{Eq. 3.5}$$

where $\delta_{ext,\lambda}$ is the extinction coefficient and can be decomposed into the sum of the absorption ($\delta_{abs,\lambda}$) and scattering ($\delta_{sca,\lambda}$) coefficients. On the other hand, in-scattering and emission may strengthen the L_λ which is passing through the layer, thus Eq. 3.5 can be re-expressed as follows:

$$dL_\lambda = -\delta_{ext,\lambda} L_\lambda \, ds + \delta_{ext,\lambda} J_\lambda \, ds \qquad \textit{Eq. 3.6}$$

where J_λ is the source function and accounts for the sum of increments in the value of L_λ due to emission ($J_{em,\lambda}$) and in-scattering ($J_{in\text{-}sca,\lambda}$; photons coming from other directions and scattered in the considered direction of the radiance; see Figure 3.2). The magnitude of $J_{em,\lambda}$ can be described according to Eq. 3.7.

$$J_{em,\lambda} = (1-\omega_\lambda) \, B_\lambda(T) \qquad \textit{Eq. 3.7}$$

where ω_λ is referred to as the "*monochromatic single scattering albedo*" and is defined as the ratio of $\delta_{sca,\lambda}$ to $\delta_{ext,\lambda}$. $B_\lambda(T)$ is the Planck function and indicates the monochromatic value of

the radiance emitted from a blackbody. $B_\lambda(T)$ is a function of wavelength and the temperature at which emission is performed. Figure 3.3 shows values of $B_\lambda(T)$ at typical temperatures found in the atmosphere for wavelengths between 1 and 50 µm.

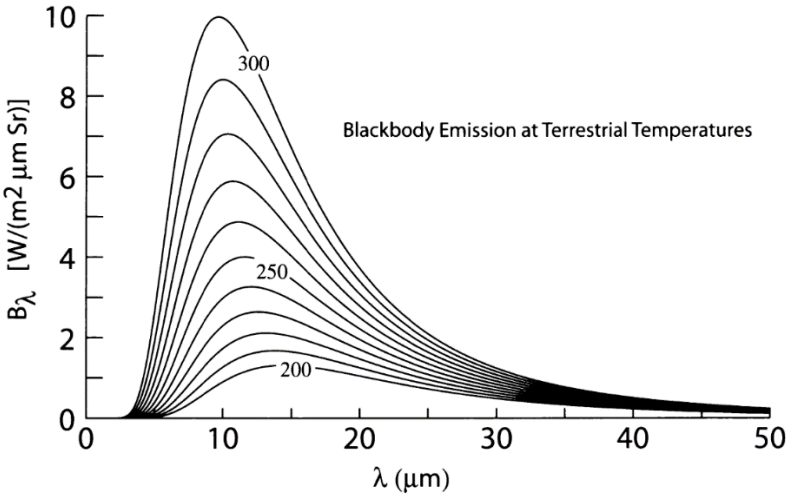

Figure 3.3. The magnitude of Planck function ($B_\lambda(T)$) for temperatures typical of those found in the atmosphere and wavelengths (λ) between 0 and 50 µm (Source: Petty, 1958).

$J_{in\text{-}sca,\lambda}$ can be described as follows:

$$J_{in-sca,\lambda} = \frac{\omega_\lambda}{4\pi}\left[\int_{4\pi} L_\lambda P_\lambda(\theta')d\Omega\right] ds \qquad \textit{Eq. 3.8}$$

where $P_\lambda(\theta')$ is the "*phase function*" (it is here normalized to 1) indicating the angular distribution of light intensity scattered by a particle at a given wavelength. It can be thought of as a probability value function, showing the chances of a photon of light being scattered in the particular direction θ' relative to the incidence direction (Figure 3.4).

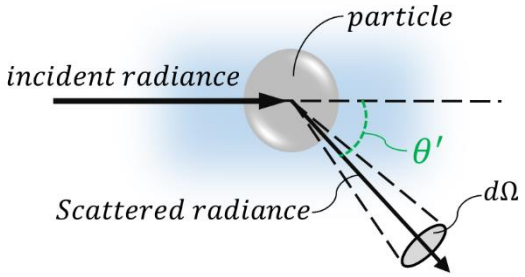

Figure 3.4. Schematical illustration of the scattering angle (θ'). (Source: own elaboration)

Introducing the *monochromatic (normal) optical thickness* ($d\tau_\lambda$) for the atmospheric element confined between the altitudes z_1 and z_2 according to Eq. 3.9 and writing *ds* as a function of

the vertical thickness of the layer (*dz*, see Figure 3.2), Eq. 3.6 may be rearranged to yield Eq. 3.10:

$$d\tau_\lambda = -\delta_{ext,\lambda}(z)\, dz \qquad \textit{Eq. 3.9}$$

$$\mu \frac{dL_\lambda}{d\tau_\lambda} = L_\lambda(0) - J_{in-sca,\lambda} - J_{em,\lambda} \qquad \textit{Eq. 3.10}$$

where μ is equal to cos(θ). Eq. 3.10 is referred to as the radiative transfer equation (RTE) for the monochromatic radiance in a plane-parallel atmosphere. Also, worth mentioning that the integration of $d\tau_\lambda$ over the atmospheric column will yield the total atmospheric optical depth.

3.3 Radiative schemes from WRF-ARW

The Advanced Research – Weather Research and Forecasting model (WRF-ARW) is a state-of-the-art open source mesoscale atmospheric model developed by the National Center for Atmospheric Research (NCAR; Powers et al., 2017). This model is widely used at research institutes and meteorological organizations worldwide for various purposes, such as real-time numerical weather prediction, data assimilation, parameterized-physics research, regional climate simulations, air quality modeling, atmosphere-ocean coupling, and idealized simulations, etc. (Blossey et al., 2013; Jimenez et al., 2016; Lin et al., 2015; Moeng et al., 2007; Montornes et al., 2016; Wang et al., 2009; Yamaguchi & Feingold, 2012; Zhong et al., 2016). It can be ran at different domains and offers various options for parameterization of convective processes, turbulent transports, evolution of surface temperature and soil moisture, and soil-air interactions (Ruiz-Arias et al., 2013; Skamarock et al., 2008). WRF-ARW also contains a number of shortwave (*swrad*) and longwave (*lwrad*) radiation parameterizations for dealing with the radiative transfer processes in the atmosphere. These parameterizations are also shared with the Model for Prediction Across Scales (MPAS; Ha et al., 2017), which is intended to replace WRF-ARW. Although all these parameterizations are meant for simulation of *irradiances* at atmospheric levels, they are different in many ways including the way they deal with clouds and aerosols, required input data for solving the RTE, spectral range and definition of shortwave and longwave bands, number of spectral bands, complexity of the calculations, etc.

The fact that WRF-ARW is widely used by researchers for various purposes worldwide and contains radiative schemes with different features for simulating the radiative processes in

the atmosphere motivated us to use the *swrad* and *lwrad* parameterizations included in this model to investigate uncertainties which may arise from neglection of the transition zone in the radiative transfer processes simulated by the radiative schemes included in a meteorological model. To this aim, among all the *swrad* and *lwrad* parameterizations included in WRF-ARW we separated those which (i) are more detailed, and (ii) allow users to consider different treatments of clouds and aerosol from the model structure. Then, we isolated and adapted them for idealized one-dimensional vertical simulations (more information is given in chapters 4 and 5). This was done to give inputs to the radiation parameterizations under controlled conditions (regardless of the uncertainties associated with other parts of the model, such as microphysics). The isolated parameterizations include the Fu-Liou-Gu (FLG; Gu et al., 2011), Rapid Radiative Transfer Model for General Circulation Models (RRTMG; Iacono et al., 2008) and New Goddard (NGO; Chou & Suarez, 1999) shortwave and longwave schemes. These parameterizations were used to perform several idealized simulations under ideal "clear-sky", "cloud" and "aerosol" modes (sensitivity analysis): (i) considering cloud- and aerosol-free atmospheres as reference setups, (ii) adding homogeneous layers of cloud—resulting from different combinations of crystal/droplet sizes and liquid/ice water content—or aerosol—with different optical characteristics—to the reference setup, (iii) calculating the radiative effects due to the different cloud/aerosol layers. On the basis of results obtained from this sensitivity analysis, we quantified the uncertainties risen from different treatments of the transition zone (using the properties of clouds or/and aerosols to describe it). A summary of the source codes and main subroutines corresponding to each parameterization is given in Table 3.1. Information about the spectral bands of the parameterization and their corresponding limits is also provided in Figure 3.4.

Table 3.1. A summary of the source codes and main subroutines corresponding to each parameterization analyzed in the present thesis. (Source: own elaboration)

Parameterization	Main subroutine	Source code	No. of Spectral bands
$RRTMG_{sw}$	*RRTMG_SWRAD*	*phys/module_ra_rrtmg_sw.F*	14
$RRTMG_{lw}$	*RRTMG_LWRAD*	*phys/module_ra_rrtmg_lw.F*	16
NGO_{sw}	*goddardrad*	*Phys/module_ra_goddard.F*	11
NGO_{lw}	*goddardrad*	*Phys/module_ra_goddard.F*	10
FLG_{sw}	*RAD_FLG*	*Phys/module_ra_flg.F*	6
FLG_{lw}	*RAD_FLG*	*Phys/module_ra_flg.F*	12

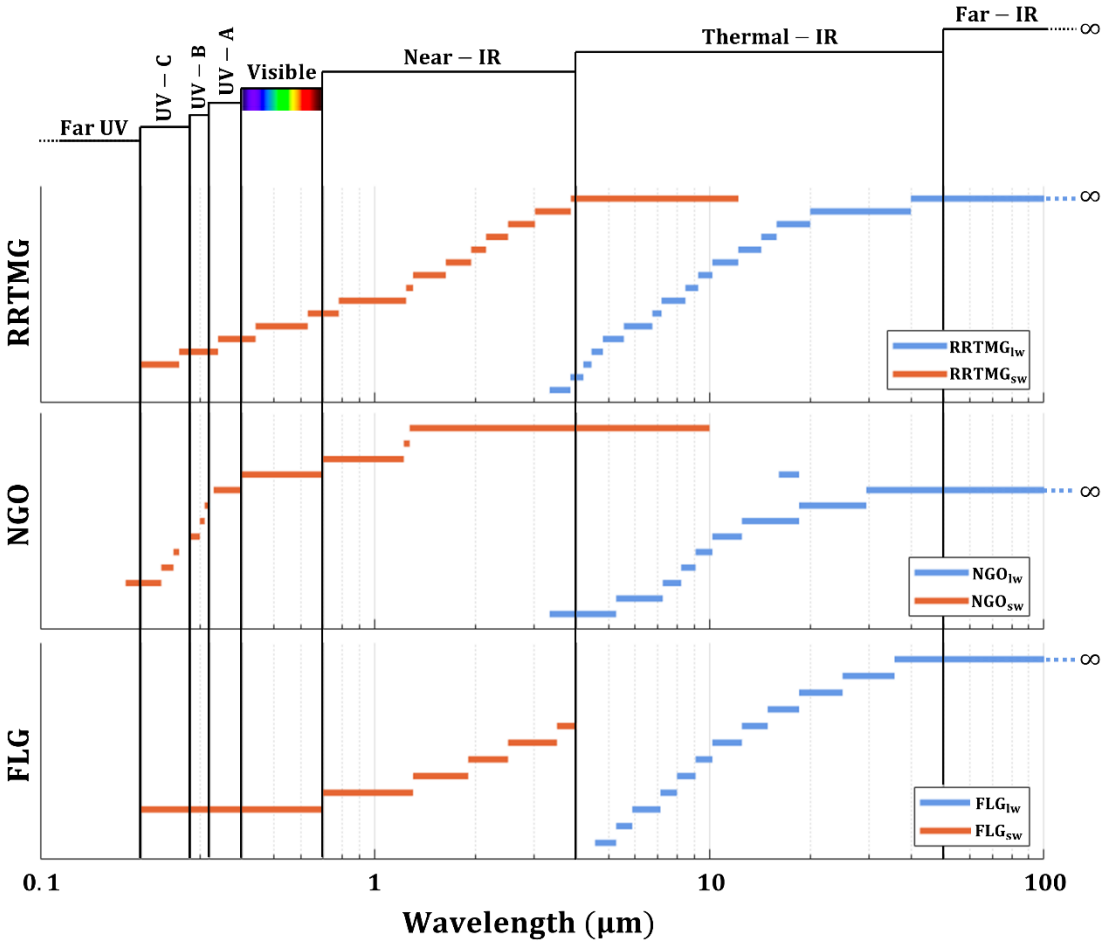

Figure 3.5. Distribution of spectral bands corresponding to the *swrad* and *lwrad* parameterizations analyzed in the present thesis. (Source: own elaboration)

Details about these parameterizations can be found in their corresponding references and the existing differences among them are given in chapters 3 and 4, but we also provide here a brief description on them:

- RRTMG uses the two stream practical improved flux method (Zdunkowski et al., 1980) for solving the RTE. In this parameterization, ice and liquid cloud optical depths are obtained

as a function of the corresponding input mixing ratios and effective crystal/droplet sizes following the method provided by Fu (1996) and Hu and Stamnes (1993), respectively. Furthermore, $RRTMG_{sw}$ considers the region between 0.20–12.20 μm (14 spectral bands) as the shortwave spectrum and the region between 3.33–∞ μm (16 spectral bands) wavelengths is considered as the longwave spectrum by $RRTMG_{lw}$.

- NGO solves the RTE by using the two stream δ-Eddington approximation method (Joseph et al., 1976) and computes the optical depth due to ice and liquid clouds based on Slingo and Schrecker (1982) method. The shortwave scheme of this parameterization (NGO_{sw}) divides the shortwave spectrum into 11 spectral bands which cover the wavelengths between 0.18–10.00 μm. The longwave spectrum for its longwave scheme (NGO_{lw}) starts from 3.33 μm and is divided into 10 spectral bands.

- In terms of FLG, RTE is solved through the δ-four stream approximation method provided by Liou et al. (1988), and it parameterizes ice and liquid cloud's optical depths based on the method described in Slingo (1989). Unlike the two other parameterizations mentioned above, there are no overlaps between the regions considered as shortwave and longwave spectrums by the FLG shortwave (FLG_{sw}) and longwave (FLG_{lw}) schemes. Specifically, the shortwave spectrum for FLG_{sw} is defined as the region between 0.20–4.00 μm (divided into 6 spectral bands) and the region starting from 4.55 μm is referred to as longwave spectrum (12 spectral bands) by FLG_{lw}.

All shortwave schemes listed above, simulate the *diffuse* and *direct* irradiances separately, and then compute the total irradiance as the addition of diffuse and direct components. However, these parameterizations involve different definitions of direct and diffuse irradiances: in case of NGO_{sw} and FLG_{sw}, direct irradiance is a summation of scattering in forward direction and direct beam, whereas for $RRTMG_{sw}$ the direct irradiance only refers to the direct beam. In the latter parameterization, scattering in all directions, including forward direction, is considered as part of the diffuse component. There are also differences in the way that the abovementioned longwave schemes deal with the radiative effects of the aerosols and clouds. Specifically, the parameterizations NGO_{lw} and FLG_{lw} deal with longwave scattering due to atmospheric particles (clouds and aerosols) and calculate their radiative effects based on their corresponding band averaged values of δ_λ, ω_λ and asymmetry factor

(g_λ). Contrarily, longwave scattering is neglected in $RRTMG_{lw}$ and thus cloud and aerosol optical depths (at each spectral band and layer) are the only relevant input to its RTE solver.

3.4 Satellite data

In chapter 6, we develop a method for quantification of the broadband longwave radiative effects of the transition zone at top of the atmosphere (TOA) over the ocean based on the instantaneous radiative measurements made by the spaceborne sensors CERES (Clouds and the Earth's Radiant Energy System) and MODIS (Moderate Resolution Imaging Radiometer). In this method, we have chosen to focus on longwave radiative effects, because what satellites observe regarding *lwrad* is basically "emitted" radiation from the surface and the atmosphere itself, while regarding *swrad* is the "reflected" (or scattered) radiation. Another reason is that *lwrad* is acting day and night, while *swrad* is only acting when Sun is present (half a day approx.). Furthermore, this method was developed for application over the oceans, in order to minimize the effect of spatial inhomogeneity of the surface characteristics (such as temperature and emissivity).

The CERES sensor is a three-channel scanning radiometer measuring the broadband outgoing shortwave (0.3-5 μm), window-region (8-12 μm) and longwave (5-100 μm) radiances at TOA with a spatial resolution of ~20 km at nadir (Loeb et al., 2001; Priestley et al., 2011). The Level-2 Single Scanner Footprint (SSF) product of this instrument provides information about the instantaneous outgoing broadband longwave radiances at TOA regardless of the sky condition (Loeb et al., 2018; Loeb et al., 2006). From the SSF Level-2 product, we used the daytime instantaneous TOA outgoing broadband longwave radiance observations of the CERES instrument onboard Aqua spacecraft ($\uparrow L_{CERES}$) along with the corresponding time, geolocation, viewing geometry and surface emissivity parameters.

In addition, several products from the MODIS instrument onboard the same satellite (Aqua) were used for identification of horizontally homogenous clear-sky and transition zone conditions within CERES footprints. Specifically, we used the ocean products: (1) geolocation (MYD03, MODIS Characterization Support Team (MCST), 2017); (2) Aerosol-Cloud-Mask and Aerosol Optical Depth (AOD) taken from the Level-2 Aerosol (MYD04, Levy et al., 2015); (3) Cloud Optical Depth (COD) from the Level-2 Cloud (MYD06, Platnick et al., 2015); and (4) Cloud Mask (MYD35, Ackerman & Frey, 2015). By combining these products, MODIS pixels

were classified into the classes “Difficult”, “Cloud”, “Aerosol”, “Clear”, “Lost A”, “Lost B”, “Lost C” at 1-km resolution (at nadir) following the procedure explained in Schwarz et al. (2017) and illustrated in Figure 3.6. Among them, the pixels labeled as “Lost” are assumed to correspond to the transition zone conditions. Indeed, for these pixels neither aerosol nor cloud optical property retrievals exist, yet they are classified as containing a cloud (Lost A), a non-cloud obstruction (Lost B), or were not processed at all in the cloud masking (Lost C).

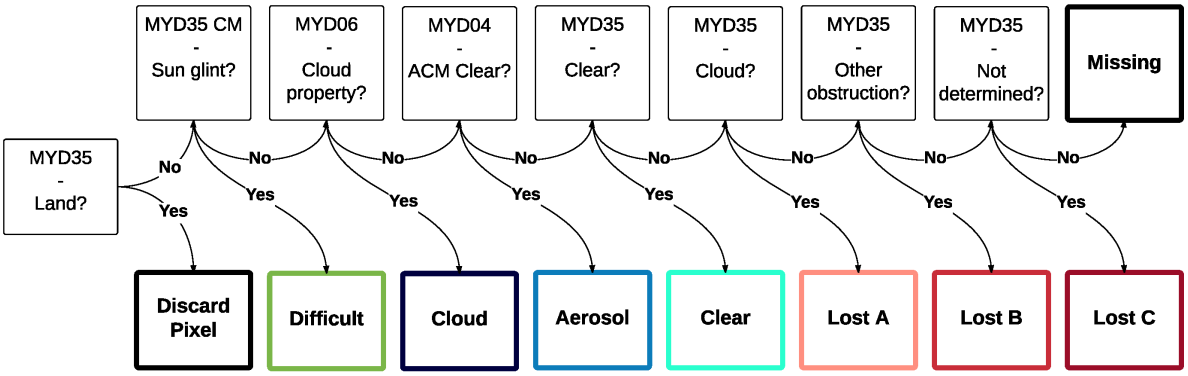

Figure 3.6. Summary of the Classification procedure applied to the Moderate-Resolution Imaging Spectro-Radiometer (MODIS) data (source: Schwarz et al., 2017; published under Creative Commons Attribution 4.0 International License). Note: the abbreviation “ACM” in this figure stands for “Aerosol Cloud Mask”.

For all CERES footprints we determined CERES viewing zenith angle (θ’’) from the CERES viewing zenith angle at surface (θ) provided in the CERES geolocation data according to Eq. 3.11:

$$\theta'' = \sin^{-1}\left(\frac{R_e \sin(\theta)}{R_e + h_{sat}}\right) \qquad \textit{Eq. 3.11}$$

where R_e and h_{sat} are the Earth radius (6371 km) and satellite altitude (705 km), respectively. To derive this equation, we have assumed the Earth as a spherical object and applied the law of sines as illustrated in Figure 3.7. We then approximated their cross-scan length of the CERES footprints ($l_{cross\text{-}scan}$; km), according to Eq. 3.12, assuming the Earth is flat on the footprint scale and the CERES footprints are rectangularly shaped (see Figure 3.8).

$$l_{cross-scan} = h_{sat}\left(tan(\theta'' + 0.8127°) - tan(\theta'' - 0.8127°)\right) \qquad \textit{Eq. 3.12}$$

The along-scan length of the footprints ($l_{along\text{-}scan}$) was taken equal to 20 km (nadir resolution). The processed MODIS data was then integrated from 1-km resolution to CERES native resolution according to the $l_{along\text{-}scan}$ and $l_{cross\text{-}scan}$ to determine the fraction of each class and the average values of COD and AOD in the CERES footprints, considering equal weights for all

MODIS pixels. Specifically, we first approximated the coordinates of the edges of CERES footprints and then looked for MODIS pixels confined within the area scanned by CERES. Afterwards, only CERES footprints meeting all the following conditions were used in the analysis: (i) solar zenith angles and CERES viewing zenith angles at surface lower than 60° (to mitigate the effect of uncertainties derived from viewing and solar geometries), (ii) no land MODIS pixels as determined using the MYD35 data are included, and (iii) number of ocean MODIS pixels more than or equal to 75% of the expected ~400 pixels falling within CERES field of view (FOV; to exclude FOVs located on the edges of the MODIS granules). Among the footprints meeting the mentioned criteria, those with a "Lost" fraction (all lost classes together) greater than or equal to 90% were classified as horizontally homogeneous transition zone footprints (the transition zone footprints selected this way, may contain up to 10% of cloud contamination). Also, those having AOD and COD equal to zero, "Lost" fraction less than 10%, and "Difficult" fraction less than 10% were classified as horizontally homogeneous clear-sky footprints.

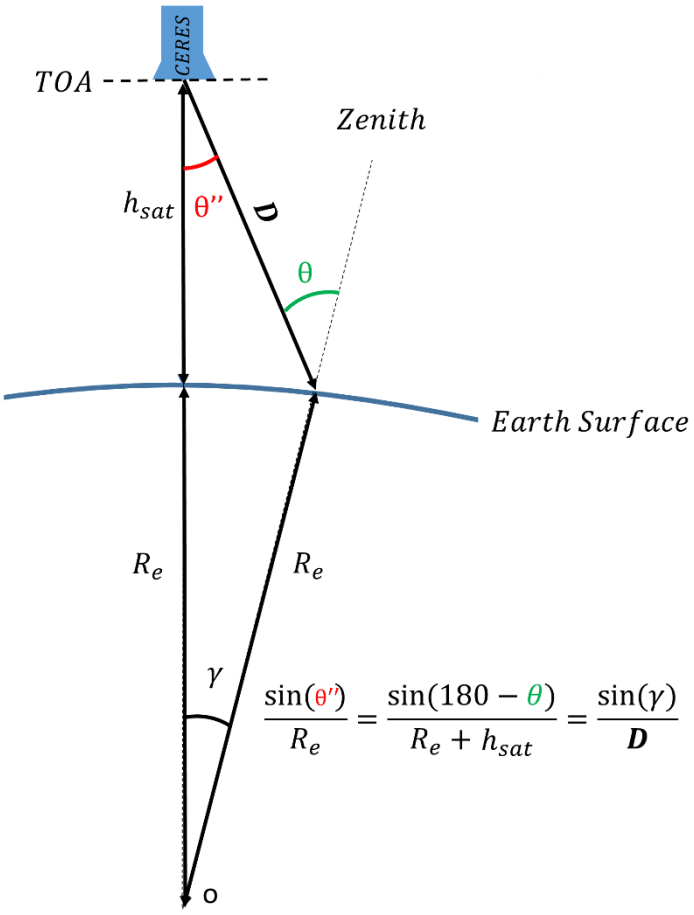

Figure 3.7. Schematic description of reasoning behind Eq. 3.11 (Source: own elaboration).

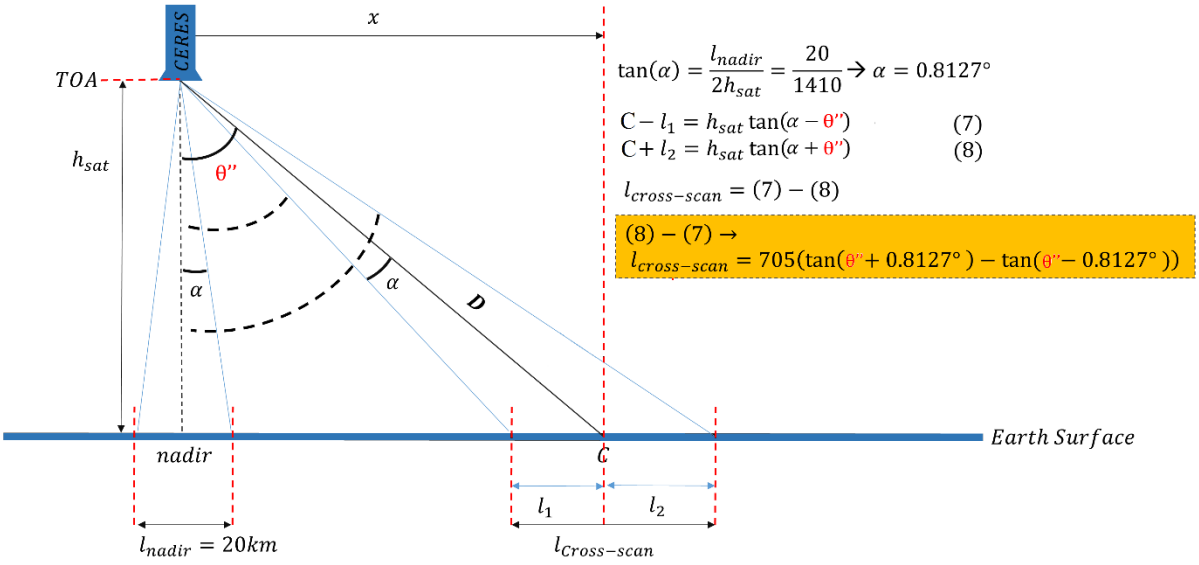

Figure 3.8. Schematic description of the reasoning behind Eq. 3.12 (Source: own elaboration). Point C in this figure indicates the longitude at the center of the CERES footprint.

3.5 Radiance Simulations

SBDART (Santa Barbara DISORT Atmospheric Radiative Transfer) is a FORTRAN computer code designed for the analysis of a wide variety of radiative transfer problems encountered in satellite remote sensing and atmospheric energy budget studies. The program is based on a collection of highly developed and reliable physical models, which have been developed by the atmospheric science community over the past few decades (Ricchiazzi et al., 1998). SBDART is based on LOWTRAN7 band models, which have a spectral resolution of 20 cm^{-1}. Furthermore, most of the code inputs have been initialized with default values, which allows the user to run the model by specifying only the input variables of interest. SBDART's main input file is called INPUT. This file contains a single NAMELIST input block also named INPUT. However, there are other input files that are sometimes required by SBDART, such as *atms.dat* file which contains data about the user defined atmospheric profiles.

We used SBDART to simulate the TOA upwelling broadband longwave (5-100 µm) clear-sky radiances ($\uparrow L_{RTM,clr}$) for the CERES viewing zenith angle (θ) for all transition zone and clear-sky footprints selected according to the criteria explained in section 3.4. The simulations were carried out by using atmospheric profiles (Hersbach et al., 2018a) and surface values (Hersbach et al., 2018b) provided by the fifth generation ECMWF reanalysis (ERA5), which render the data at 0.25°×0.25° spatial resolution and 1h time intervals. Specifically, we used

the profiles of specific humidity, geopotential, ozone mass mixing ratio, and temperature at all available pressure levels (1000 hPa-1 hPa) as well as mean sea level pressure and 2 m air temperature and dewpoint temperature were obtained. For each (clear-sky/transition-zone) footprint, the surface and atmospheric data of the closest ERA5 cell were combined with each other and linearly interpolated in time according to the CERES time of observation. The combined and interpolated profiles were then fed to SBDART for simulation of $\uparrow L_{RTM,clr}$.

The effect of all well-mixed atmospheric gases was taken into consideration. Specifically, the broadband sea surface emissivity and the CO_2 concentration in atmosphere were set to the constant values of 0.982 (equal to the estimated broadband longwave sea surface emissivity included in the CERES SSF data; Geier et al., 2003) and 388.71 ppm (which is the value corresponding to the year 2010; European Environmental Agency: https://www.eea.europa.eu/, last access: 13 May 2021), respectively. For the other gases the default concentration values included in SBDART model were used. For each individual clear-sky and transition zone footprint, SBDART model was ran with 20 zenithal streams and the spectral upwelling radiances (including the solar contribution, which actually is very low) were calculated in the range of 5-100 μm in steps of 0.2 μm. Then, the upwelling radiances at 30 km altitude at the SBDART computational zenithal angles were outputted and linearly interpolated to determine the magnitude of the upwelling radiance in the direction θ.

The simulated clear-sky radiances ($\uparrow L_{RTM,clr}$) were validated through comparing them with the $\uparrow L_{CERES}$ values corresponding to the clear-sky footprints ($\uparrow L_{CERES,clr}$). The comparison was made using the corresponding isotropic irradiances ($\pi\uparrow L_{CERES,clr}$ and $\pi\uparrow L_{RTM,clr}$), and was based on the linear correlation coefficient between the simulated and the measured values, as well as by analyzing the probability distribution, mean and variance of the differences. Eventually, the broadband longwave (5-100 μm) radiative effect on flux (assuming an isotropic distribution for the radiance) for the transition zone footprints (W m^{-2}) was calculated as the difference between the radiances measured by CERES ($\uparrow L_{CERES,trz}$) and the corresponding simulated clear-sky values ($\uparrow L_{RTM,clr}$).

Chapter 4

Transition Zone Radiative effects in Shortwave Radiation Parameterizations

This chapter is a transcript of the paper with slight changes:

Jahani, B., Calbó, J., & González, J. (2019). Transition zone radiative effects in shortwave radiation parameterizations: Case of weather research and forecasting model. *Journal of Geophysical Research: Atmospheres*, 124, 13,091– 13,104.
doi: https://doi.org/10.1029/2019JD031064

The changes applied consist of:

Modifying some symbols as well as figure and table labeling and numbering for the sake of consistency with the whole thesis document. In addition, the literature cited in this transcript has also been moved to the final chapter of this document (References), in order to have all used references together.

Summary

A number of studies have stated that the shift from a cloud-free to cloudy atmosphere (and vice versa) contains an additional phase, named “Transition (or twilight) Zone”. However, the information available about radiative effects of this phase is very limited. Consequently, in most meteorological and climate studies the area corresponding to the transition zone is considered as an area containing aerosol or optically thin clouds. This study investigates the differences in shortwave radiative effects driven from different treatments of the transition zone. To this aim, three of the shortwave radiation parameterizations (New Goddard, RRTMG and FLG) included in the Advanced Research Weather Research and Forecasting Model (WRF-ARW) were isolated and adapted for one-dimensional vertical simulations. These parameterizations were then utilized to perform simulations under ideal “cloud” and “aerosol” modes, for different values of (i) cloud optical depths resulting from different sizes of ice crystals or liquid droplets, and mixing ratios; and (ii) different aerosol optical depths combined with various aerosol types. The resulting shortwave broadband total, direct and diffuse irradiances at the Earth surface were analyzed. The uncertainties originated from different assumptions of a situation regarding to the transition zone are quite substantial for all the parameterizations. For all the parameterizations, direct and total irradiances are the least and most sensitive irradiances to different treatments of the transition zone, respectively. Differences in the radiative effects of transition zone dominantly result from the difference between the radiative effects of clouds and aerosols (different types), not from cloud type or droplet/crystal size.

4.1 Introduction

Solar radiation is a key element of the Earth atmosphere system and is involved in several natural processes. Furthermore, the amount of solar radiation reaching the Earth surface is mainly affected by aerosols and clouds, which are two particular cases of a single phenomenon, i.e. a suspension of particles in the air. However, the radiation-cloud-aerosol interactions are rather complex (Fan et al., 2016). Consequently, radiation, cloud and aerosol parameterizations may be considered as one of the most computationally demanding parts of the atmospheric, climate and weather forecasting models (Carslaw et al., 2013). Thus, to this date a number of efforts have been made by researchers for studying and improving the radiation, cloud and aerosol parameterizations in such models (Loeb et al., 2018; Ming & Held, 2018).

However, despite the existing differences in the origin and composition of clouds and aerosols, it is not always easy to clearly classify the type of suspension in the sky (González et al., 2017; Seinfeld et al., 2016). Indeed, the characteristics of the suspension sometimes lay on the border between those corresponding to a cloud and those corresponding to an atmospheric aerosol (Calbó et al., 2017). More precisely, the shift between cloudy to cloud-free atmosphere contains an additional phase named “Transition Zone” (also known as “Twilight Zone”), with characteristics that depend on both the nearby clouds and surrounding aerosols (Fuchs & Cermak, 2015; Koren et al., 2007). The situation gets even more complex when using data derived from measurements with relatively low temporal and/or spatial resolutions (Várnai & Marshak, 2011, 2015).

The transition zone may correspond to various processes including hydrated aerosols, cloud fragments sheared off from the adjacent clouds, decaying and incipient clouds, etc. (Koren et al., 2009). Moreover, studies show that the transition zone (as a property of a cloud field) may expand up to tens of kilometers away from the cloud field (Várnai & Marshak, 2011). According to Koren et al. (2007), almost 30-60% of the globe categorized as clear sky (cloud-free) can potentially correspond to this phase. Based on the total cloud and aerosol records of the Moderate Resolution Imaging Radiometer (MODIS) satellite sensor between 2007 and 2011, Schwarz et al. (2017) concluded that almost 20% of all pixels could be categorized as transition zone. Calbó et al. (2017) quantified that the frequency of the transition zone is about 10%, on the basis of three ground-based observation systems at two mid-latitude sites.

They also found that transition zone produces typically an optical depth of less than 0.32 (at 0.500 μm wavelength), but it might be found, at those sites, for optical depth as high as 2.00. All these papers underline the fact that a significant proportion of sky at any time is covered by a particle suspension with characteristics of the transition zone, which seems to play, consequently, a significant role in the energy balance of the Earth. Despite the importance of the transition zone, however, the currently available information about its radiative effects and the mechanisms at which it influences the total climate system is limited. In most meteorological, climate and weather forecasting studies and models, aerosols and clouds are commonly treated separately (as either dry aerosols or fully developed clouds), leaving no gap for the transition zone. This implies that, in the mentioned models, the condition of sky in each layer of a given grid cell is assumed to be either cloudy (fully or partially covered) or cloud-free (maybe containing aerosols), neglecting the transition zone.

The separate treatment of clouds and aerosols arises the question "how different the simulated radiative effects in a grid cell of a meteorological/weather forecasting model will be, if a situation corresponding to transition zone is assumed as cloud or aerosol?" Or in other words, "how important it is to study and deal with the radiative characteristics of the transition zone?" For this purpose, the present study aims to answer the mentioned questions by applying a sensitivity analysis to the shortwave radiation parameterizations included in a particular meteorological model, namely the Weather Research and Forecasting Model (WRF), which is being widely used by meteorology organizations and research institutes all around the world.

4.2 Materials and Methods

4.2.1 Model description

The advanced Research WRF (WRF-ARW) is a state-of-the-art open source mesoscale atmospheric model, developed by National Center for Atmospheric Research (NCAR) for both research and numerical weather prediction purposes (Powers et al., 2017). This model, which is probably the most popular meteorological (it also has a climatic version) model worldwide, has the capability to be used for a wide range of applications, such as real-time numerical weather prediction, data assimilation, parameterized-physics research, regional climate simulations, air quality modeling, atmosphere-ocean coupling,

and idealized simulations (Blossey et al., 2013; Jimenez et al., 2016; Lin et al., 2015; Moeng et al., 2007; Montornes et al., 2016; Wang et al., 2009; Yamaguchi & Feingold, 2012; Zhong et al., 2016). In addition, it can be ran at different domains and offers various options for parameterization of convective processes, turbulent transports, evolution of surface temperature and soil moisture, and soil-air interactions (Ruiz-Arias et al., 2013; Skamarock et al., 2008). Similarly, WRF-ARW employs different frameworks for parameterization of shortwave radiation (swrad). However, the way these parameterizations deal with clouds and aerosols varies from one to another. They are also different in terms of other factors, such as required input data, spectral range, number of spectral bands, complexity of the calculations, etc. (Montornès et al., 2015).

The swrad parameterizations included in the latest version of WRF-ARW (Version 4.0) consist of: Dudhia (Dudhia, 1989), Fu-Liou-Gu (FLG, Gu et al., 2011), Goddard, New Goddard (Chou & Suarez, 1999), CAM (Collins et al., 2006), RRTMG, RRTMG-fast, RRTMG-K (Baek, 2017; Iacono et al., 2008), GFDL (Fels & Schwarzkopf, 1981) and Held-Suarez relaxation (Chen et al., 1997). However, among them, the parameterizations which (i) are more detailed and (ii) allow the users to consider different treatments of clouds and aerosol were chosen for this study. Thus, selected parameterizations comprise RRTMG ($RRTMG_{sw}$), New Goddard (NGO_{sw}) and FLG (FLG_{sw}). In these parameterizations, diffuse and direct irradiances are simulated separately and then the total component is computed as the summation of diffuse and direct. However, these parameterizations involve different definitions of direct and diffuse irradiances: in the parameterizations NGO_{sw} and FLG_{sw}, direct irradiance is a summation of scattering in forward direction and (eventually attenuated by absorption) direct beam, whereas for $RRTMG_{sw}$ the direct irradiance only refers to the direct beam. In the latter parameterization, scattering in all directions is considered as part of the diffuse component. More information about these parameterizations can be found in Skamarock et al. (2008) and Montornès et al. (2015), but a brief description follows:

$RRTMG_{sw}$ uses the two stream practical improved flux method (Zdunkowski et al., 1980) for solving the Radiative Transfer Equation (RTE). Furthermore, it considers the region between 0.20 μm and 12.20 μm wavelengths as the shortwave spectrum and splits into 14 spectral bands: 3 UV, 2 PAR and 9 near-IR. In this parameterization, ice and liquid

cloud optical depths are obtained as a function of the corresponding input mixing ratios and effective crystal/droplet sizes following the method provided by Fu (1996) and Hu and Stamnes (1993), respectively.

NGO_{sw} solves the RTE by using the two stream δ-Eddington approximation method (Joseph et al., 1976). In this parameterization, the shortwave radiation wavelength ranges between 0.18 μm and 10.00 μm and it is divided into 11 spectral bands: 7 UV, 1 PAR and 3 near-IR. NGO_{sw} computes the optical depth due to ice and liquid clouds based on Slingo and Schrecker (1982) method.

In terms of FLG_{sw}, RTE is solved through the δ-four stream approximation method provided by Liou et al. (1988) and the region with wavelength between 0.20 μm and 4.00 μm is considered as shortwave spectrum. This parameterization splits this spectral region into 6 separate bands: 1 UV-PAR and 5 near-IR. FLG_{sw} parameterizes ice and liquid cloud's optical depths based on the method described in Slingo (1989).

These parametrizations have a different definition of the shortwave region. In addition, they also have a different distribution of spectral bands over the shortwave region. However, it should be noted that despite the shortwave region is extended up to 10.00 and 12.20 μm for parameterizations NGO_{sw} and $RRTMG_{sw}$, none of the three parameterizations chosen deals with emission. This means that the irradiances calculated by these parameterizations are only affected by scattering and absorption. In order to be able to assess the performance of the radiation parameterizations independently of the other schemes of WRF-ARW and design simulations under ideal conditions, the source codes of these parameterizations were isolated from the main model structure and adapted for one dimensional vertical simulations ("sand-box" approach). By doing so, the inputs to the radiation parameterizations were given to the parameterizations under controlled conditions (regardless of the uncertainties associated with other parts of the model, such as microphysics). Consequently, the final results obtained from the radiation parameterizations will be affected only by the radiation parameterization itself. These isolated parameterizations were then utilized to perform several simulations under ideal "cloud" and "aerosol" modes.

4.2.2 Experiment setup

To address the objectives of this study, conditions at mid-day for summer at mid-latitudes (46.8˚) were selected, resulting in a solar zenith angle of ≈ 30˚, and a standard mid-latitude summer time atmosphere was used (Anderson et al., 1986). A cloud- and aerosol-free (clean) atmosphere and a surface albedo of 0.14 was initially considered as a reference setup for all of the simulations. For all simulations an equal number of 78 atmospheric layers were considered, the model top was set at 30 km. However, based on the results obtained for this reference model configuration, the same analysis was carried out later for different values of solar zenith angle and surface albedo (a summary of results obtained for these additional configurations is provided in Section 4.4). Figure 4.1 shows the vertical profiles of air temperature (T) and water vapor mixing ratio (qv) in the reference atmosphere.

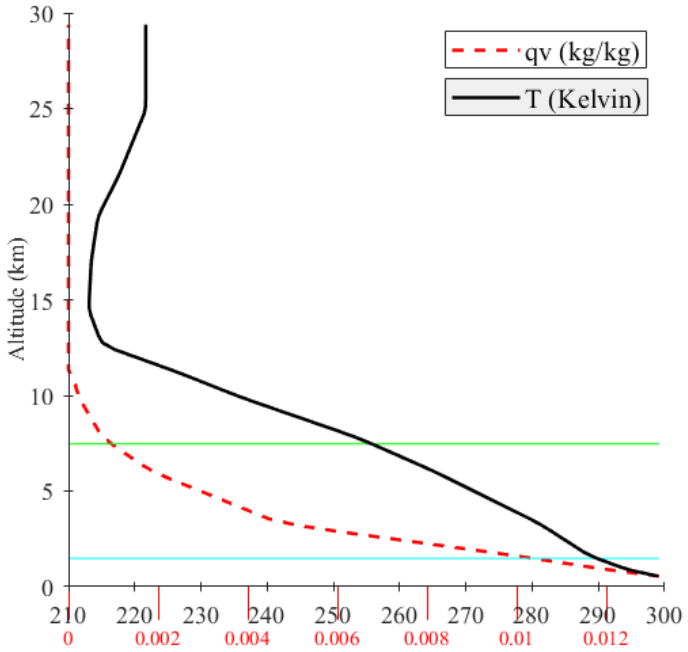

Figure 4.1. Vertical profiles of temperature T, (K, solid black line) and water vapor mixing ratio qv (kg/kg, red dashed line) used in the reference atmosphere (note: the blue and green line represent the average altitude of the liquid and ice clouds layers, respectively). (Source: Jahani et al., 2019)

The isolated parameterizations were used to simulate the shortwave broadband direct (horizontally projected), diffuse and total irradiances at Earth surface by adding to the reference setup (i) ice and liquid clouds with different optical depths (τ) resulting from different crystal and droplet sizes and water contents; and (ii) aerosols with different τs

combined with various aerosol types. In all these simulations the cloud/aerosol τ was considered to vary between 0.01 and 2.00. This range of τ covers low and high values of τ which can potentially represent a situation regarding to the transition zone. Also, it contains the typical range of τ for the transition zone that Calbó et al. (2017) found for two sites located in unpolluted regions.

The cloud altitude for the liquid and ice clouds was considered to be ~1.5 km and ~7.5 km, respectively. The effective radius of cloud ice crystals was considered to vary between 10 and 120 µm. Similarly, the effective radius of cloud droplets was considered to vary between 2.5 and 15 µm. These cases comprise 11 combinations (4 ice and 4 liquid clouds, and 3 aerosol types) for each considered τ. As each of the parameterizations selected uses different methods and coefficients for calculation of cloud τ, the cloud τ for all crystal and droplet sizes were obtained through trial and error: fixing droplet/crystal size and increasing/decreasing water/ice mixing ratio until the desired τ (at the band that contains the 0.550 µm wavelength) with a maximum error of ±1% is obtained.

The aerosol types used in this study consist of three pre-described aerosol models which are common among all parameterizations selected: (1) urban; (2) continental; and (3) marine. Among them, the marine and urban aerosols are the most reflective and absorbing aerosols, respectively. In these parameterizations, the aerosol τ at 0.550 µm and the desired aerosol type are given to the parameterization as an input. Then, based on the aerosol type selected, the parameterizations use the pre-described aerosol models included in them to distribute the aerosols' optical properties (τ, single scattering albedo and asymmetry factor) for all of the spectral bands along the column of the atmosphere. For all parameterizations and aerosol types, aerosols are mostly concentrated in the lower layers (< 3 km) of the atmosphere, decaying exponentially with height. It is worth mentioning that the other optical characteristics of these aerosol types and their distribution along the column of the atmosphere are defined differently by each parameterization: there are minor differences between $RRTMG_{sw}$ and NGO_{sw}, while those of FLG_{sw} are remarkably different compared with the other parameterizations. The information regarding to the values and distributions of aerosol single scattering albedo (SSA) and asymmetry factor (ASY) of the three parameterizations at the spectral bands

containing the 0.550 μm wavelength have been extracted from the source codes of the parameterizations and provided in Figure 4.2.

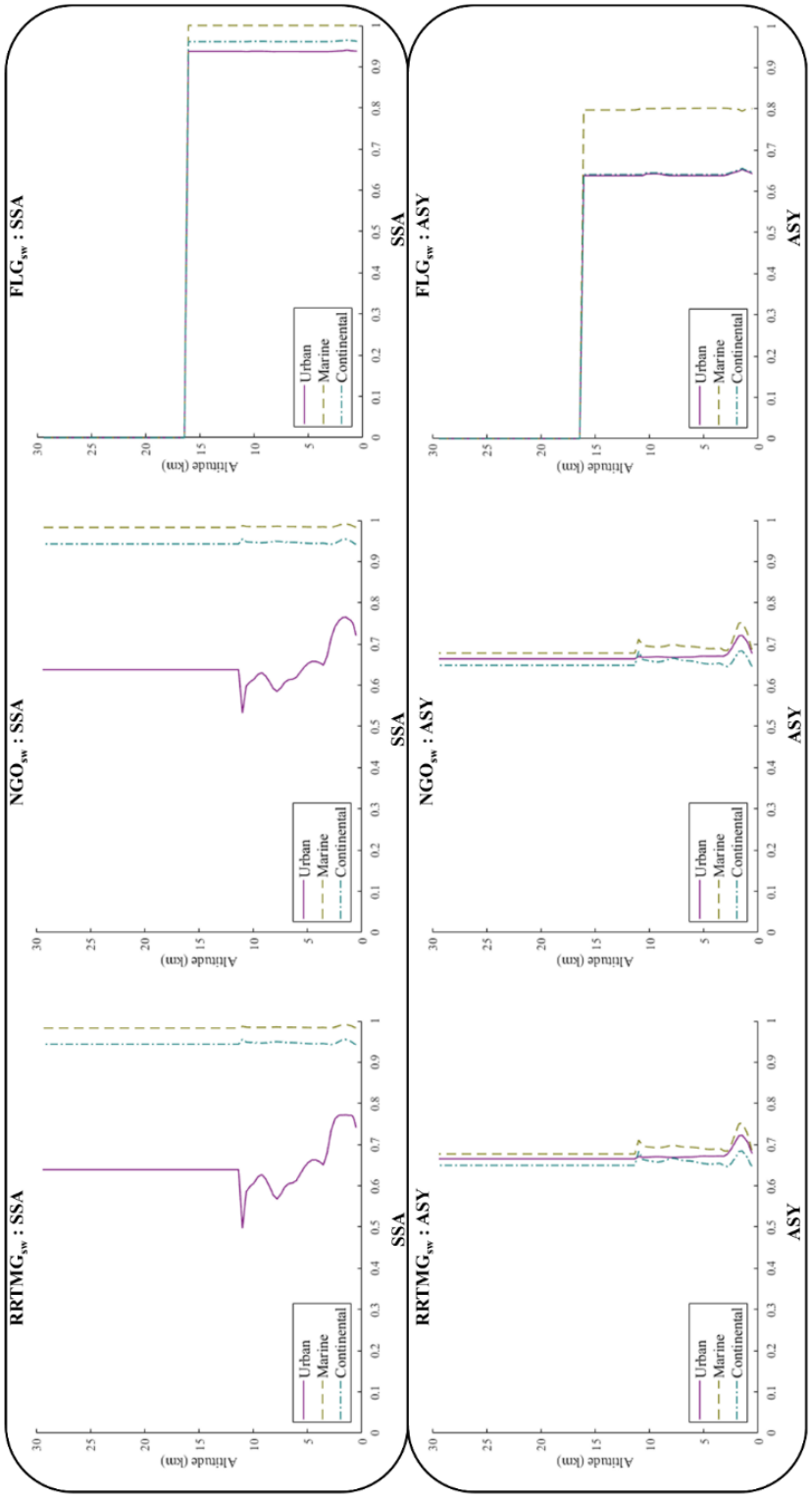

Figure 4. 2. Vertical profiles of SSA (top panel) and ASY (bottom panel) for the pre-described urban, continental and marine aerosol models included in the parameterizations RRTMG$_{sw}$, NGO$_{sw}$ and FLG$_{sw}$. (Source: Jahani et al., 2019)

4.2.3 Quantification of radiative effects and sensitivity

In order to be able to have a clear insight about the differences among irradiances, which may only arise from different treatments of the transition zone (i.e., description as cloud or as aerosol), and eliminate the effect of other factors which may affect the broadband direct, diffuse and total irradiances at Earth surface (ozone, trace gases, water vapor, etc.), the radiative effects for the mentioned irradiances under each model run were calculated through Eq. 4.1:

$$RE_{\alpha,irr,par}(\tau) = E_{\alpha,irr,par}(\tau) - E_{irr,par}(0) \qquad \textit{Eq. 4.1}$$

where $RE_{\alpha,irr,par}(\tau)$ (W m^{-2}) is the radiative effect for irradiance *irr* (total, direct, diffuse) for the αth run (α=1-11) for the parameterization *par* at a given τ. $E_{\alpha,irr,par}(\tau)$ (W m^{-2}) is the computed irradiance *irr* for the *α*th run of the parameterization *par* at a given τ; $E_{irr,par}(0)$ stands for the irradiance *irr* computed by the parameterization *par* under the reference configuration (cloud- and aerosol-free atmosphere, τ=0). These radiative effects were then utilized in the further analysis.

Nevertheless, in order to be able to provide comparisons among the radiative effects and to quantify the ranges at which they may vary for different treatments of the transition zone (a comparison between ice clouds and aerosols, I-a; and another between liquid clouds and aerosols, L-a), two additional indices; the Radiative Effect Range (ΔRE, W m^{-2}) and the Mid-range Radiative Effect ($\overline{RE}$), were proposed:

$$\Delta RE_{irr,par}(\tau) = Max(RE_{\alpha,irr,par}(\tau)) - min(RE_{\alpha,irr,par}(\tau)) \qquad \textit{Eq. 4.2}$$

$$\overline{RE}_{irr,par}(\tau) = [Max(RE_{\alpha,irr,par}(\tau)) + min(RE_{\alpha,irr,par}(\tau))] / 2 \qquad \textit{Eq. 4.3}$$

where $\Delta RE_{irr,par}(\tau)$ and $\overline{RE}_{irr,par}(\tau)$ (W m^{-2}) take into account the dispersion of all radiative effects for the cases I-a (3 aerosol types and 4 ice clouds, α=3+4) and L-a (3 aerosol types and 4 liquid clouds, α=3+4), produced by the parameterization *par*, for the irradiance *irr* at a given τ. It should be noted that hereafter the range will also be called "sensitivity", as this measure of the dispersion of results for a given τ indicates the error that may be involved with using one particular treatment of the transition zone. Here, $\overline{RE}$ has been calculated as an average of the minimum and maximum REs for (i) simplicity and (ii) in order to avoid giving extra weight to the values produced by cloud or by aerosol

treatment. This way, $\overline{\mathrm{RE}}$ is just in the mid point between the max and min RE values at a given τ, so in the middle of the range of values where the actual RE should lay. Therefore, this mid-range value is appropriate to be used for normalizing the range (see below).

However, due to the differences in the magnitude of the radiative effects (mainly depending on τ), Eqs. 4.2-4.3 fail to show the importance of the sensitivity in relation to the corresponding parameterizations. For this reason, a relative index, the Relative Radiative Effect Sensitivity (RΔRE, %, Eq. 4.4) was introduced as well:

$$\mathrm{R\Delta RE}_{\mathrm{irr,par}}(\tau) = 100 \times [\Delta \mathrm{RE}_{\mathrm{irr,par}}(\tau) \,/\, |\overline{\mathrm{RE}}_{\mathrm{irr,par}}(\tau)|] \qquad \textit{Eq. 4.4}$$

Moreover, in order to represent the relative sensitivity in a bulk single number for the whole range of τs, the Mean Relative Radiative Effect Sensitivity ($\overline{\mathrm{R\Delta RE}}$, Eq. 4.5) was also defined as follows:

$$\overline{\mathrm{R\Delta RE}}_{\mathrm{irr,par}} = \frac{1}{\tau_{\max} - \tau_{\min}} \times \int_{\tau_{min}}^{\tau_{max}} \mathrm{R\Delta RE}_{\mathrm{irr,par}}(\tau)\, d\tau \qquad \textit{Eq. 4.5}$$

Thus, variables $\mathrm{R\Delta RE}_{\mathrm{irr,par}}(\tau)$ and $\overline{\mathrm{R\Delta RE}}_{\mathrm{irr,par}}$ (%) provide quantitate information about the ΔRE regarding to each parameterization in relation to the corresponding radiative effect simulated by the parameterization for a given and for the whole range of τ, respectively. In some way, these values are useful as a first estimation of the uncertainty that is involved when dealing with radiative effects of a transition zone situation.

4.3 Results

4.3.1 Radiative effects (RE)

An overall picture about the variations of direct ($\mathrm{RE_{dir}}$), diffuse ($\mathrm{RE_{dif}}$) and total ($\mathrm{RE_t}$) radiative effects of the atmosphere resulting from different treatments of transition zone, based on the model simulations, is provided in Figure 4.3. In this figure, the upper panel shows comparison between the REs of ice clouds and aerosols (I-a), and the lower panel shows the comparison between the REs of liquid clouds and aerosols (L-a). Furthermore, the lines of the same type and color correspond to the maximum and minimum possible values of $\mathrm{RE_{dir}}$, $\mathrm{RE_{dif}}$ and $\mathrm{RE_t}$ due to aerosols, ice and liquid clouds for τ between 0.01 and 2.00, based on each parameterization. Therefore, for each case (I-a and L-a) the distance between the lowest and highest lines of the same type is the range

of dispersion (ΔRE) of the simulated values of RE_{dir}, RE_{dif} and RE_t, based on the different treatments of the transition zone. According to this figure, for all parameterizations and for both comparison cases, the increment in the aerosol/cloud τ leads to reduction and enhancement of direct and diffuse irradiances, respectively, resulting in a decrease in total irradiance. In addition, the declining rate of RE_{dir} versus τ seems to be higher in $RRTMG_{sw}$ compared to the two other parameterizations. The lines for $RRTMG_{sw}$ given in Figure 4.3 are more concave, meaning that the decrease is particularly steeper for lower τ (<1.00). For the two other parameterizations, RE_{dir} appears to have almost similar rate of variation versus τ. This may be due to the difference in the definition of direct irradiance among the parameterizations; as above mentioned, direct irradiance is defined as the summation of direct beam and forward scattering in NGO_{sw} and FLG_{sw}, while in $RRTMG_{sw}$, direct irradiance only refers to the direct beam. Furthermore, from Figure 4.3 it can be seen that the effect of droplet/crystal size on the simulated RE_{dir} and RE_{dif} seem to be different depending on the parameterization utilized. Its effect, however, is generally smaller on RE_t for all the parameterizations.

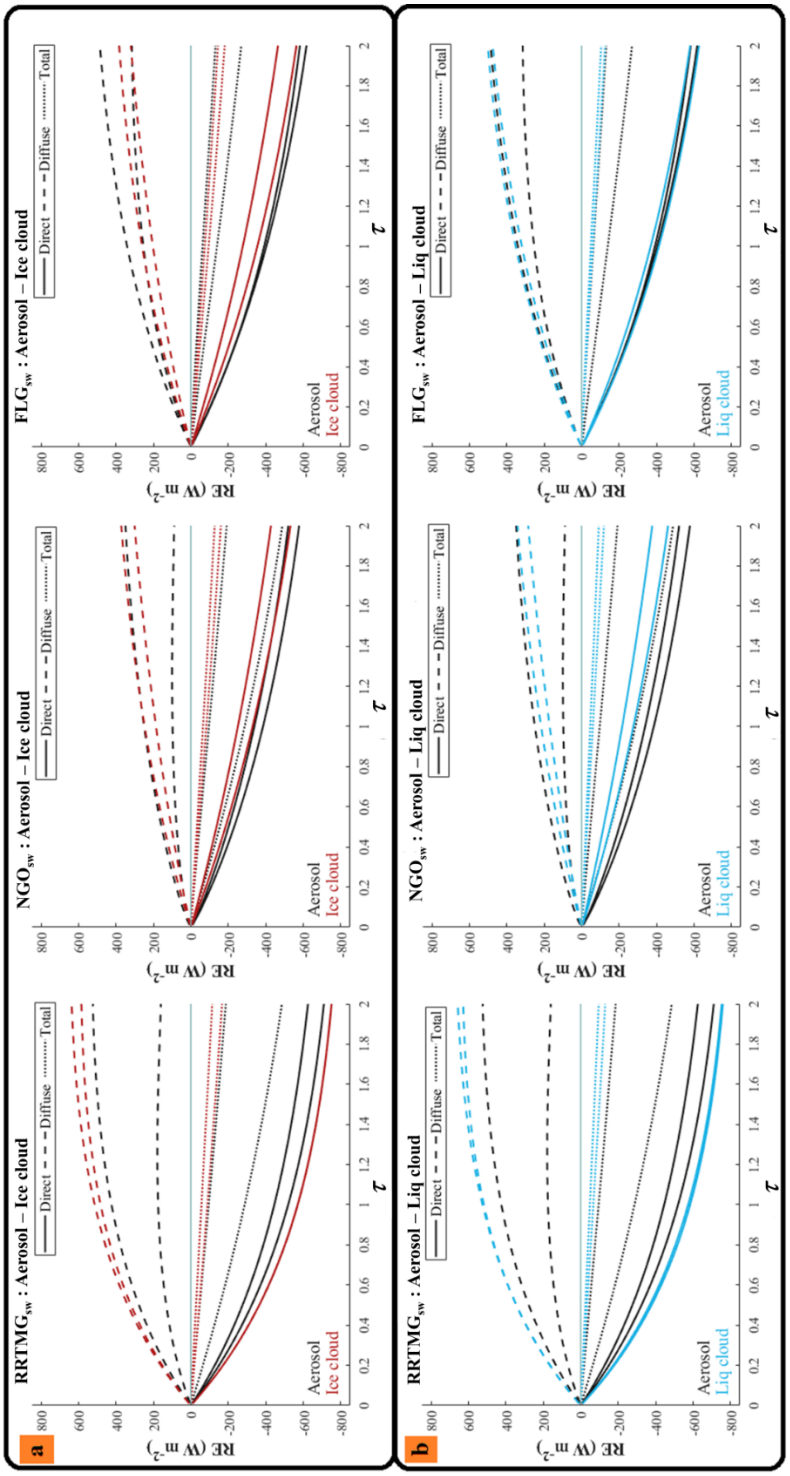

Figure 4.3. Minimum and Maximum values of RE_{dir}, RE_{dif} and RE_t of the atmosphere resulted from different treatments of transition zone versus τ (0.01- 2.00), based on NGO_{sw}, $RRTMG_{sw}$ and FLG_{sw} simulations for cases I-a (panel "a") and L-a (panel "b"). (Source: Jahani et al., 2019)

According to this figure, there is a substantial difference among the REs (all components) simulated by the parameterization FLG_{sw} for the liquid and ice clouds. This difference can be more visibly seen in RE_{dif} compared to other components of solar radiation. Furthermore, based on this parameterization liquid clouds have higher RE_{dir} and RE_{dif} (absolute values) compared to the ice clouds. Also, the effect of particle (crystal/droplet) size (the distance between the highest and lowest values) is larger for ice clouds, compared to liquid clouds This may be due to the larger range of ice crystal sizes considered in our simulations compared to liquid droplets, because larger particles imply enhanced forward scattering (Bohren & Huffman, 1998; Petty, 1958), and thus more (less) radiation in the direct (diffuse) component. In contrast, the parameterization FLG_{sw} projects very similar RE_{dir} for the three different aerosol types, so only at the higher τs the differences are visible in Figure 4.3. Moreover, the magnitude of RE_{dir} simulated by FLG_{sw} for aerosols is also similar to that of the liquid clouds with large droplet size, in particular at the lower τs. However, there are more differences among the RE_{dif} simulated by this parameterization for the three aerosol types. According to the simulations of this parameterization, the RE_{dif} of aerosols may be similar to that of ice cloud or liquid cloud, depending on the aerosol type. However, the magnitude of RE_t corresponding to aerosols (depending on the aerosol type) can either be similar to or greater (in absolute sense) than that of clouds.

In case of the parameterization NGO_{sw}, although it produces some differences between ice and liquid clouds, it projects the same RE_{dir} and RE_{dif} for liquid clouds with small droplet sizes and ice clouds with large crystal sizes at the same τ (Figure 4.3). This parameterization produces lower RE_{dir} and RE_{dif} (absolute values) for the liquid clouds compared to the ice clouds, unlike FLG_{sw}. Contrarily, and similar to FLG_{sw}, this parameterization produces distinct RE_t for ice and liquid clouds. The effect of particle (crystal/droplet) size is, however, smaller compared to FLG_{sw}. Also, for $\tau<0.50$ the RE_{dif} simulated by this parameterization for the aerosols is very similar to that of the clouds. However, for $\tau>0.50$ RE_{dif} simulated by NGO_{sw} for aerosols (depending on the type) may either be very similar or very different from that of both cloud types. Although the RE_{dir} simulated by this parameterization for the aerosols is generally greater than that of the clouds, however, it projects similar RE_{dir} for clouds with small crystal sizes and a particular

type of aerosols (continental). In terms of total radiation, Figure 4.3 shows a vast difference among the REs of clouds and aerosols simulated by the parameterization NGO_{sw}, even at very low τ (0.10): those corresponding to the aerosols are greater (in absolute sense) than those of the clouds.

Unlike the two other parameterizations discussed, $RRTMG_{sw}$ produces almost the same RE_{dir} for different types of ice and liquid clouds resulting from different droplet/crystal sizes (Figure 4.3). This implies that the RE_{dir} simulated by the parameterization $RRTMG_{sw}$ is not very sensitive to different treatments of clouds, at least at this limited range of low τ. However, it is worth mentioning that $RRTMG_{sw}$ projects a higher extinction rate of RE_{dir} for clouds compared to the two other parameterizations studied: for example, at τ=1.00, RE_{dir} for both liquid and ice clouds is approximately 575 W m^{-2}. The simulated values of RE_{dif} show that the parameterization $RRTMG_{sw}$ considers some differences between the two cloud types, which do not appear to be substantial, though. In addition, it can also be seen that cloud particle size has more influence on the RE_{dif} simulated by $RRTMG_{sw}$ for ice clouds, compared with that of liquid clouds. In case of total irradiance, although the parameterization $RRTMG_{sw}$ produces differences between the RE_t of the two cloud types, it simulates similar RE_t for the liquid clouds with small droplet sizes and ice clouds with large crystal sizes. Moreover, similar to diffuse irradiance, cloud particle size seems to have more influence on the RE_t regarding to ice clouds, compared to that of liquid clouds. In contrast, from the data represented in Figure 4.3 it can be seen that the parameterization $RRTMG_{sw}$ considers a vast difference between the RE (all components) of different aerosol types compared to the cloud types. This fact shows that the parameterization $RRTMG_{sw}$ is more sensitive to aerosol characteristics compared to those of clouds. Also, it produces less RE_{dif} and RE_{dir} (in absolute sense) for aerosols compared to clouds, which combined produce, however, a greater effect (in absolute sense) on the total irradiance. It is worth mentioning that this difference between the RE of clouds and aerosols increases with τ.

4.3.2 Sensitivities (ΔRE)

The values of ΔRE_{dir}, ΔRE_{dif} and ΔRE_t for each of the parameterizations versus τ are provided in Figure 4.4. Based on the $\overline{R\Delta RE}$ values also shown in Figure 4.4, it can be

affirmed that in all the parameterizations studied, RE_{dir} and RE_t are the least and most sensitive variables to different treatments of transition zone. However, in an absolute sense, for the parameterizations $RRTMG_{sw}$ and FLG_{sw}, RE_{dif} is the most sensitive component. It is worth mentioning that despite the direct component is the least sensitive to the transition zone treatment, ΔRE_{dir} still seems to be notable ($\overline{R\Delta RE}_{dir,I-a}$= 44, 25 and 38%, $\overline{R\Delta RE}_{dir,L-a}$= 57, 27 and 11% for parameterizations NGO_{sw}, $RRTMG_{sw}$ and FLG_{sw}, respectively).

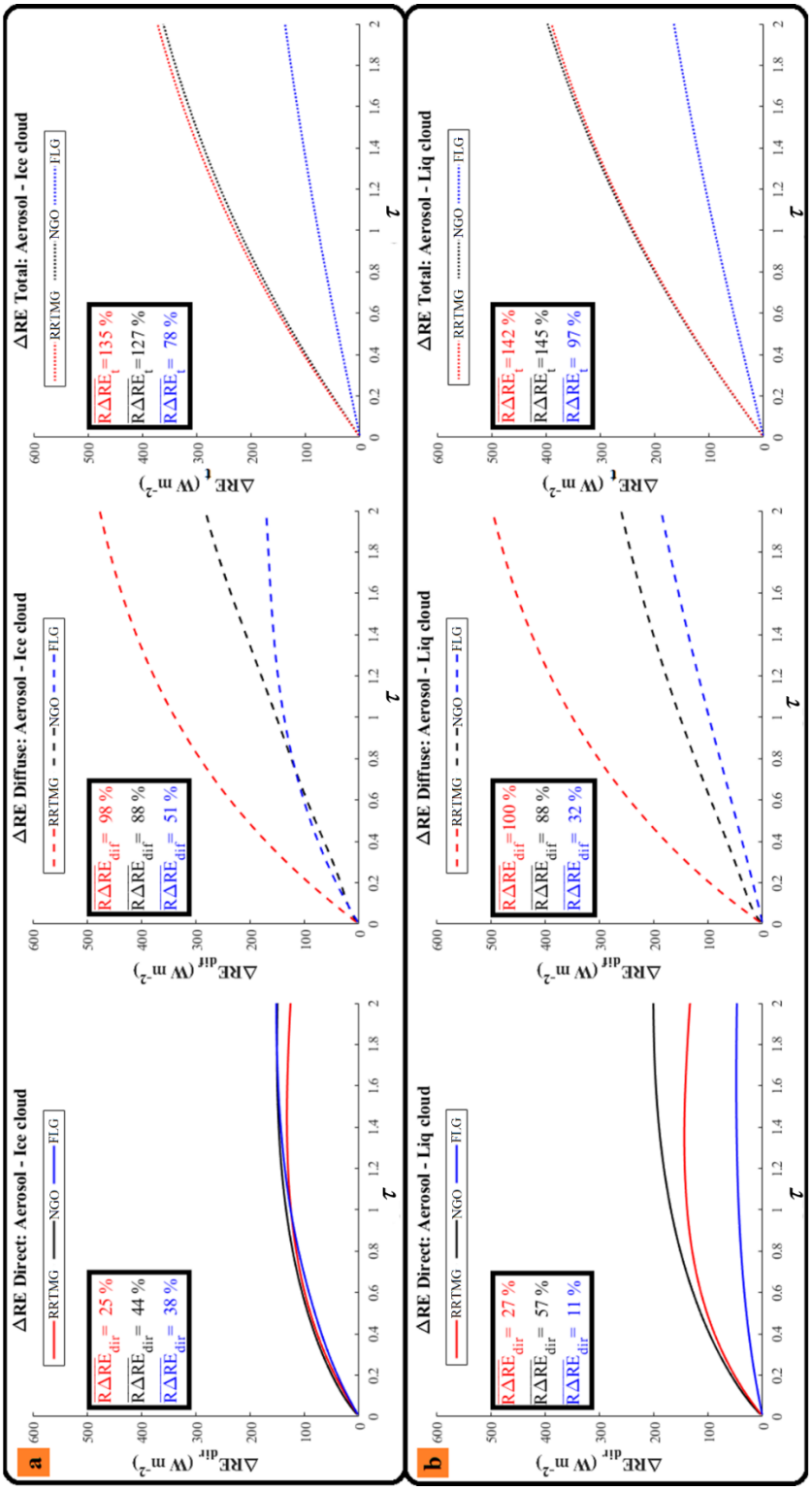

Figure 4.4. values of ΔRE_{dir}, ΔRE_{dif} and ΔRE_t versus τ (0.01- 2.00), based on $RRTMG_{sw}$, NGO_{sw} and FLG_{sw} simulations for cases I-a (panel "a") and L-a (panel "b"). Note: the values of $\overline{R\Delta RE}_{dir}$, $\overline{R\Delta RE}_{dif}$ and $\overline{R\Delta RE}_t$ with respect to each parameterization are also presented in this figure. (Source: Jahani et al., 2019)

As shown in Figure 4.4, the values of $\Delta RE_{dir,I\text{-}a}$ and $\Delta RE_{dir,L\text{-}a}$ resulted from the simulations of the three parameterizations nonlinearly vary with τ. In case of the parameterizations NGO_{sw} and FLG_{sw}, $\Delta RE_{dir,Ia}$ and $\Delta RE_{dir,La}$ continuously increases with τ for the whole range of τ studied. This increase, however, is steeper for lower τ (<1.00). In contrast, for $RRTMG_{sw}$, Figure 4.4 shows an increase and a slight decline in $\Delta RE_{dir,Ia}$ and $\Delta RE_{dir,L\text{-}a}$ for τs ranged 0.01-1.00 and 1.00-2.00, respectively. The rapid extinction of the direct component in $RRTMG_{sw}$ (specially for lower range of τ) may be a possible reason for this particular behavior observed in $\Delta RE_{dir,Ia}$. From Figure 4.4 it can also be seen that there are slight differences among values of $\Delta RE_{dir,I\text{-}a}$ resulted from the simulations of all parameterizations. For $\Delta RE_{dir,L\text{-}a}$, however, there are more substantial differences among the parameterizations. This means that although all the parameterizations are almost equally sensitive to different treatment of the transition zone under the case I-a, there are quite vast differences among their sensitivities under the case L-a. This difference can be more visibly seen in the parameterization FLG_{sw}. In case of this parameterization, $\Delta RE_{dir,Ia}$ varies between 2 and 152 W m^{-2}, whereas $\Delta RE_{dir,L\text{-}a}$ varies between 1 and 48 W m^{-2} for the range of τ studied. In contrast, for NGO_{sw} the values of $\Delta RE_{dir,L\text{-}a}$ (4-201 W m^{-2}) are higher than those of $\Delta RE_{dir,I\text{-}a}$ (3-150 W m^{-2}). Unlike the two other parameterizations, $RRTMG_{sw}$ is almost equally sensitive under both cases ($\Delta RE_{dir,L\text{-}a}$ and $\Delta RE_{dir,I\text{-}a}$ show similar values).

According to Figure 4.4, although the ΔRE_{dif} regarding to all parameterizations increases with τ for both cases, the values corresponding to the case I-a are slightly greater than those of L-a. Implying that there are very small differences among the models sensitivities in simulation of diffuse irradiance for both cases. This figure also shows that $\Delta RE_{dif,I\text{-}a}$ and $\Delta RE_{dif,L\text{-}a}$ values resulting from $RRTMG_{sw}$ simulations increase nonlinearly with τ and their magnitudes at any τ are clearly higher than those of the two other parameterizations. In addition, these values are also higher than the corresponding values of ΔRE_{dir} resulting from $RRTMG_{sw}$ simulations, which imply higher sensitivity in diffuse compared to the direct. More precisely, different treatments of transition zone under the case I-a seem to lead to a wider range of results for the diffuse component of solar radiation compared to direct for the parameterization $RRTMG_{sw}$. In case of the parameterization FLG_{sw}, despite $\Delta RE_{dif,I\text{-}a}$ and $\Delta RE_{dif,L\text{-}a}$ have almost the same values for

the range of τ studied, they have different variation patterns; $\Delta RE_{dif,I\text{-}a}$ varies nonlinearly and the other linearly. The magnitude of the $\Delta RE_{dif,I\text{-}a}$ resulted from the simulations of the parameterization FLG_{sw} more or less varies in the same range as $\Delta RE_{dir,I\text{-}a}$ does (specially for τ<1.00). But, comparing them with the corresponding mid-point radiative effects, the relative sensitivity of this parameterization to simulation of the diffuse component at the transition zone is higher than the direct ($\overline{R\Delta RE}_{dif,I-a}$ = 51%, $\overline{R\Delta RE}_{dir,I-a}$= 38%). This figure also shows a substantial difference between the $\Delta RE_{dir,La}$ and $\Delta RE_{dif,L\text{-}a}$ resulted from FLG_{sw} simulations. For the parameterization NGO_{sw}, in contrast, the ΔREs for both cases vary linearly and they have very similar values in the range of τ studied. In both cases (I-a and L-a), the ΔRE_{dif} values resulting from NGO_{sw} simulations are greater than those of ΔRE_{dir}, but this difference can be more clearly be seen in the case I-a.

In case of total irradiance, as Figure 4.4 shows both $\Delta RE_{t,I\text{-}a}$ and $\Delta RE_{t,L\text{-}a}$ values with respect to all parameterizations vary nonlinearly for the range of τ studied. This nonlinear behavior can be more clearly seen for τs greater than 1.00. Based on Figure 4.4, at any given τ, despite the differences observed in the diffuse and direct irradiances simulated by the parameterizations $RRTMG_{sw}$ and NGO_{sw}, the summation of these two components produces mostly the same values of $\Delta RE_{t,I\text{-}a}$ and $\Delta RE_{t,L\text{-}a}$ for both parameterizations. This implies that the parameterizations NGO_{sw} and $RRTMG_{sw}$ have a similar sensitivity to simulation of the total irradiance in the transition. The data regarding to $\overline{R\Delta RE}$ given in Figure 4.4 also proves this fact. From Figure 4.4 it can also be seen that there is a substantial difference between the values of $\Delta RE_{t,I\text{-}a}$ and $\Delta RE_{t,L\text{-}a}$ resulted from the simulations of FLG_{sw} and those of the two other parameterizations. More precisely, at any given τ, the ΔRE_t of NGO_{sw} and $RRTMG_{sw}$ are more than twice as much as that of FLG_{sw}. This implies that the total irradiance simulated by FLG_{sw} is much less sensitive to different treatments of the transition zone under both cases compared with the two other parameterizations.

4.4 Discussion

The simulations of all the parameterizations studied show that for all the treatments (different clouds and aerosol types) RE_{dir} and RE_t decrease (i.e. reach negative values that are

greater in absolute terms) and RE_{dif} increases with τ, which is to be expected due to enhanced absorption and scattering at higher τs. However, REs (at any given τ) for each treatment and the rate at which they vary versus τ may be different depending on the parameterization utilized. Similarly, the ΔRE (all components) involved with the simulation of the radiative effect of a situation corresponding to the transition zone is different depending on the parameterization utilized. The differences in the treatment of forward scattering, number of spectral bands and range of shortwave spectral region considered by the parameterizations, the methods used for solving the RTE and for cloud/aerosol parameterization as well as the code accuracy (Huang & Wang, 2019) may be reasons for these differences detected among the parameterizations. Indeed, Table 4.1 shows the irradiances simulated by the three parameterizations under the reference (aerosol- and cloud-free) configuration, and the remarkable difference among parameterizations is obvious, so confirming that some of the former reasons play an important role.

The parameterization $RRTMG_{sw}$ gives mostly similar REs for ice and liquid clouds with different particle sizes (especially in direct irradiance). However, it gives very different REs for different aerosol types. In addition, the parameterization $RRTMG_{sw}$ simulates completely different REs for clouds and aerosols. More precisely, despite RE_{dir} with respect to aerosols is slightly lower than that of clouds (in terms of the absolute values), the resulting RE_t regarding to aerosols is much less (i.e., greater in absolute terms) than that of clouds. This may mainly be due to the way diffuse component is described by this parameterization for clouds and aerosols. In other words, the parameterization $RRTMG_{sw}$ seems to project quite different rates of scattering for aerosols and clouds at any τ. According to the simulations of this parameterization, the difference in the RE take the lowest and highest values for direct ($\overline{\mathrm{R\Delta RE}}_{\mathrm{dir,I-a}}$=25% and $\overline{\mathrm{R\Delta RE}}_{\mathrm{dir,L-a}}$ = 27%) and total ($\overline{\mathrm{R\Delta RE}}_{\mathrm{t,I-a}}$ =135% and $\overline{\mathrm{R\Delta RE}}_{\mathrm{t,L-a}}$ =142%) irradiances, respectively. This notable uncertainty observed in the total irradiance, mainly originates from the uncertainty associated with simulation of diffuse irradiance at the transition zone ($\overline{\mathrm{R\Delta RE}}_{\mathrm{dif,I-a}}$= 98% and $\overline{\mathrm{R\Delta RE}}_{\mathrm{dif,L-a}}$= 100%). If we assume the whole atmosphere as one atmospheric layer, according to the Eq. 4.3 given in Menang (2018) the shortwave heating rate (H, K day^{-1}) for the whole column of the reference atmosphere (ΔP= 956hPa) based on $RRTMG_{sw}$ simulations would be equal to 2.10 K day^{-1}. Accordingly, the different treatment of the transition zone at τ=1.00 will result in a H dispersion range (ΔH) of about 2.50 and 2.43 K

day^{-1} for the cases I-a and L-a, respectively. Furthermore, these differences in the RE of transition zone result from the difference between the RE of clouds and aerosols, not from different cloud droplet/crystal size and water/ice content. This means that according to $RRTMG_{sw}$ simulations, by assuming the fact that the RE of transition zone is the same as that of a layer of (i) cloud, (ii) aerosol or (iii) mixture of both, the uncertainty involved with not considering the actual RE of the transition zone can be rather high, especially for diffuse and total irradiances. It is, however, worth mentioning that it is generally believed that total irradiance is less sensitive to aerosol optical properties compared to direct and diffuse irradiances (Ruiz-Arias et al., 2013) and that some numerical weather prediction models do not consider aerosols in the simulation of RE (Jimenez et al., 2016).

Unlike $RRTMG_{sw}$, there are distinct differences among the direct and total REs simulated by the parameterization NGO_{sw} for ice and liquid clouds with different particle sizes. For diffuse component, however, this parameterization projects small differences among the REs of ice and liquid clouds. The projected differences among the REs of clouds of different type with different particle sizes were expected due to the fact that this parameterization was in principle developed for studying the role of clouds and their interactions with radiation in climate and hydrological systems and later the impact of aerosols was added to it (Tao et al., 2009). Based on NGO_{sw} simulations, a substantial difference in the REs resulted from different treatments of a situation corresponding to transition zone can be seen in almost all of the irradiances evaluated. This difference, however, can be more notably seen in total irradiance ($\overline{\mathrm{R\Delta RE}}_{\mathrm{dir,L-a}}$=57%, $\overline{\mathrm{R\Delta RE}}_{\mathrm{dif,L-a}}$=88% and $\overline{\mathrm{R\Delta RE}}_{\mathrm{t,L-a}}$=145%). According to the simulations of this parameterization, the H regarding to the reference atmosphere is 1.87 K day^{-1} and the corresponding values of ΔH for I-a and L-a at τ=1.00 are 2.48 and 2.41 K day^{-1}. The differences observed in the RE_{dif} and RE_t of transition zone are generally due to the difference in the REs regarding aerosols and clouds (similar to $RRTMG_{sw}$), but the difference observed in RE_{dir} seems to be mainly owing to difference in the REs of the clouds of different type with various particle sizes. It is worth mentioning that the parameterization NGO_{sw} may produce mostly similar RE_{dif} for clouds and aerosols of marine and urban origins. However, there is a distinct difference among the RE_{dir} and RE_t simulated for clouds and aerosols.

The parameterization FLG_{sw} is less sensitive to different treatments of the transition zone compared with the two other parameterizations. But still it has a relatively high sensitivity to

different treatments of the transition zone ($\overline{\mathrm{R\Delta RE}}_{\mathrm{t,L-a}}$= 97% and $\overline{\mathrm{R\Delta RE}}_{\mathrm{t,I-a}}$=78%). According to FLG_{sw} simulation, H for the reference atmosphere is equal to 1.77 K day^{-1} and the corresponding values of ΔH for I-a and L-a at τ=1.00 are 0.76 and 0.67 K day^{-1}. The parameterization FLG_{sw} also reveals a distinct difference among the ice and liquid clouds (for all of the irradiances). It also projects different REs for clouds of the same type but with different particle sizes. The difference among the REs regarding to the two cloud types is larger in diffuse and total compared to the direct. The RE_{dir} regarding to aerosols (all types) is very similar to those of liquid clouds. Also, the RE_{dif} regarding to the liquid clouds simulated by this parameterization has a value similar to that of the marine aerosols. A similar pattern is also visible in RE_t; for τ between 0.01 and 2.00, the RE_t simulated by FLG_{sw} for the ice and liquid clouds is very similar to that of marine aerosols.

All results shown and discussed so far correspond to a particular atmospheric profile, Sun position and ground albedo. In order not to be restricted to these specifications, the same analysis was carried out for a solar zenith angle of about $60°$, and for surface albedo of 0.04 and 0.40. Figure 4.5 provides a comparison among the values of $\overline{\mathrm{R\Delta RE}}_{\mathrm{dir}}$, $\overline{\mathrm{R\Delta RE}}_{\mathrm{dif}}$ and $\overline{\mathrm{R\Delta RE}}_{\mathrm{t}}$ resulted from the simulations of the parameterizations NGO_{sw}, $RRTMG_{sw}$ and FLG_{sw} under the mentioned conditions. In this figure the former configuration (solar zenith angle $\approx 30^{\circ}$ and surface albedo=0.14) is considered as the reference setup. Information regarding to direct, diffuse and total irradiances simulated by the parameterizations for the aerosol- and cloud-free atmosphere setups for these additional cases (solar zenith angle of about 60°, and for surface albedo of 0.04 and 0.40) is given in Table 4.1. Again, it should be noted the important differences among the three radiation schemes, as previously noted for the reference setup.

Table 4.1. Direct, diffuse and total irradiances (W m^{-2}) simulated by the parameterizations NGO_{sw} (N.G.), $RRTMG_{sw}$ and FLG_{sw} for reference aerosol- and cloud-free atmosphere configurations: (i) solar zenith angle ~30˚ and surface albedo=0.14 (**ref**), (ii) solar zenith angle ~30° and surface albedo=0.04 (**ALB_4**), (iii) solar zenith angle ~30° and surface albedo=0.40 (**ALB_40**), and (iv) solar zenith angle ~60° and surface albedo= 0.14 (**SZA_60**). (Source: Jahani et al., 2019)

Configuration	Direct			Diffuse			Total		
	N.G.	$RRTMG_{sw}$	FLG_{sw}	N.G.	$RRTMG_{sw}$	FLG_{sw}	N.G.	$RRTMG_{sw}$	FLG_{sw}
ref	848	835	872	55	55	61	903	890	933
ALB_4	848	835	872	47	50	54	897	884	926
ALB_40	848	835	872	71	70	81	919	905	953
SZA_60	414	405	427	45	45	49	459	450	476

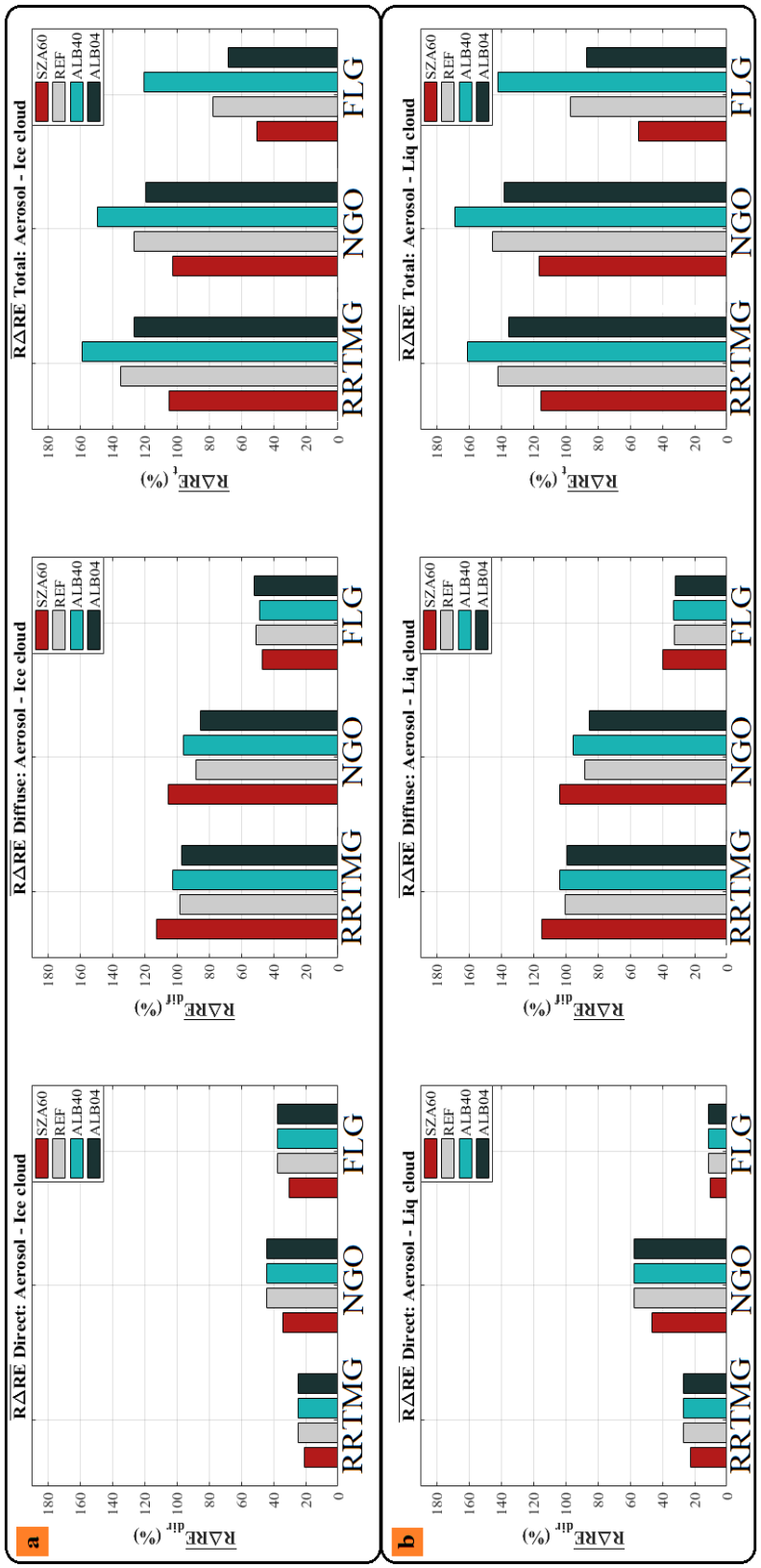

Figure 4.5. The values of $\overline{R\Delta RE}_{dir}$ (direct, left), $\overline{R\Delta RE}_{dif}$ (diffuse, middle) and $\overline{R\Delta RE}_{t}$ (total, right) resulted from $RRTMG_{sw}$, NGO_{sw} and FLG_{sw} simulations for the cases I-a (panel "a") and L-a (panel "b") for (i) the reference setup (REF, gray), (ii) solar zenith angle~60° and surface albedo= 0.14 (SZA_60, red) and (iii) solar zenith angle~30° and surface albedo=0.04 (ALB_4, dark green), and (iv) solar zenith angle~30° and surface albedo=0.40 (ALB_40, light green). (Source: Jahani et al., 2019)

Figure 4.5 suggests that despite the uncertainties involved with different treatments of the transition zone change depending on the solar zenith angle and surface albedo, they still remain substantial. It also shows that in almost all cases (all except the direct and diffuse irradiances simulated by FLG_{sw}) all the parameterizations studied have slightly higher sensitivities under the case L-a than I-a. From the information provided in Figure 4.5, it can be realized for all parameterizations, under all model configurations (different solar zenith angles and surface albedos) total irradiance is the most sensitive irradiance to different treatments of the transition zone. Given the facts that (i) most weather prediction models internally need the total irradiance in the model's energy budget (Jimenez et al., 2016) and (ii) a large proportion of the cloudless atmosphere may potentially represent the transition zone (Koren et al., 2007; Schwarz et al., 2017), we can speculate that the confusion involved with the cloud-aerosol transition zone may introduce large biases in other parts of the models.

Based on Figure 4.5, for all configurations evaluated, the parameterizations NGO_{sw} and $RRTMG_{sw}$, respectively, showed the highest and lowest sensitivity in the direct component. In terms of diffuse irradiance, (under all configurations) parameterizations $RRTMG_{sw}$ and FLG_{sw}, respectively, had the highest and lowest sensitivity to different treatments of the transition zone. The difference between the $\overline{\mathrm{R\Delta RE}}_{\mathrm{dif}}$ with respect to NGO_{sw} and $RRTMG_{sw}$ under different configurations, however, is very small. These two parameterizations also present similar (and high) sensitivity to different treatments of the transition zone in total irradiance.

Figure 4.5 also shows that the change in surface albedo has no effect on the sensitivity in direct irradiance, which is to be expected because physically surface albedo has no influence on the direct beam, unlike what happens on diffuse (and therefore, on total) irradiances. For the parametrizations $RRTMG_{sw}$ and NGO_{sw} the sensitivity in simulation of RE_{dif} increases and decreases by rising and reducing the value of surface albedo, respectively. The change associated with the change in surface albedo, however, is quite small, but slightly more noticeable in NGO_{sw} simulations. The change in the surface albedo has a reverse and similar effect in the sensitivity of the parameterization FLG_{sw} under the cases I-a and L-a, respectively. This adverse effect is due to the fact that for the range of τ studied, the change in the surface albedo has a very little effect on the ΔRE_{dif} compared to $\overline{\mathrm{RE}}_{\mathrm{dif}}$. At τ=1, for instance the values of ΔRE_{dif} obtained from FLG_{sw} simulations for surface albedos of 0.04 and 0.40 for the case I-

a are equal to 136 and 142 W m^{-2}, respectively. At the same τ, the corresponding values of $\overline{RE}_{dif}$ are 262 and 299 W m^{-2}, respectively. However, in case of the parameterizations $RRTMG_{sw}$ and NGO_{sw}, the situation is reverse. In case of the total irradiance, Figure 4.5 shows that all parameterizations for both cases have a higher and lower sensitivities to different treatments of the transition zone for larger and smaller values of surface albedo, respectively.

From the data provided in Figure 4.5 it can also be seen that all of the parameterizations for both cases have a lower sensitivity in simulation of direct and total irradiances at a higher solar zenith angle. Accordingly, all of the parameterizations under both cases (except FLG_{sw} under the case I-a) have a higher sensitivity to different treatments of the transition zone.

4.5 Conclusions

The main objective of the present study was to investigate the differences in the broadband shortwave RE (Radiative Effect on surface irradiance) simulated by a meteorological/weather forecasting model, if a situation corresponding to the cloud-aerosol transition zone is assumed as either cloud or aerosol. To this aim, the shortwave parameterizations NGO_{sw}, $RRTMG_{sw}$ and FLG_{sw} included in the model WRF-ARW (Advanced Research - Weather Research and Forecasting) were isolated and adapted for ideal one-dimensional vertical simulations. These parameterizations were then utilized to perform a number of simulations under ideal “cloud” and “aerosol” modes, for different values of (i) cloud optical depths resulting from different sizes of crystals/droplets and mixing ratios (to describe water or ice content); and (ii) different aerosol optical depths combined with various aerosol types. These tests were carried out for two cases: the transition zone between ice clouds and aerosols (I-a) and between Liquid clouds and aerosols (L-a). The results obtained in this study can be summarized as follows:

- As expected, for all the parameterizations, increasing cloud/aerosol particle optical depth leads to increasing (negative) effect in direct radiation component and increasing (positive) effect in diffuse component. The effect on the direct component dominates over the effect in diffuse, thus leading to a negative effect in total radiation. However, there are differences among the radiative effects simulated by the parameterizations, which can be more dominantly seen in diffuse irradiance, compared to other radiation components.

- Although there are differences among the radiative effects simulated by the parameterizations, the sensitivity involved with different assumptions of a situation regarding to the transition zone is quite substantial for all of them and it increases with optical depth. Based on the simulations performed for different solar zenith angles and surface albedos, regardless of the parameterizations utilized, different assumptions about the transition zone will lead to a mean relative radiative effect sensitivity ($\overline{\mathrm{R\Delta RE}}$) of 10-57, 32-115 and 50-169% in simulation of direct, diffuse and total irradiances (see Figure 4.5).

- Among the parameterizations studied, FLG_{sw} was the least sensitive parameterization to different treatments of the transition zone for simulating diffuse and total irradiances ($\overline{\mathrm{R\Delta RE}}_{\mathrm{dif}}$=32-52% and $\overline{\mathrm{R\Delta RE}}_{\mathrm{t}}$=50-141%). In simulation of diffuse irradiance, the highest sensitivity was observed in the parameterizations $RRTMG_{sw}$ ($\overline{\mathrm{R\Delta RE}}_{\mathrm{dif}}$=105-160%). On the other hand, NGO_{sw} shows the highest sensitivity in simulations of direct irradiance ($\overline{\mathrm{R\Delta RE}}_{\mathrm{dir}}$ =34-57%). Despite parameterizations NGO_{sw} and $RRTMG_{sw}$ show different sensitivities (i.e., induce different uncertainties) to simulation of direct and diffuse irradiances, they have an almost similar (and high) sensitivity in the resulting total irradiance ($\overline{\mathrm{R\Delta RE}}_{\mathrm{t}}$ ranges between 102-169% and 105-161% for parameterizations NGO_{sw} and $RRTMG_{sw}$, respectively).

- For all the parameterizations and under all tested model configurations (different solar zenith angles and surface albedos) direct and total irradiances were the least and most sensitive irradiances to different treatments of the transition zone, respectively.

- The previously mentioned sensitivities, i.e. differences in the radiative effect of the transition zone depending on the assumed treatment, dominantly result from the difference between results for clouds and aerosols (different types), not from cloud type or droplet/crystal size.

These results show that different treatments of the transition zone may lead to substantial uncertainties in simulation of direct, total and diffuse irradiances and underline the importance of investigating the radiative effects of the transition zone, as the radiation field is of essential importance in meteorological and climate models. This means assuming the state of sky as either cloudy or cloud-free (neglecting the transition zone) may introduce large

uncertainties to estimation of shortwave radiation reaching the Earth surface and thus the surface energy balance. This simplified assumption about the state of sky also leads to a large difference in the atmospheric shortwave heating rate which will influence the dynamics of the meteorological model. Results also suggest that the magnitude of these uncertainties is higher when parameterizations which cope with RTE (Radiative Transfer Equation) in more detail ($RRTMG_{sw}$ and NGO_{sw}) are employed. Indeed, although complex (detailed) parameterizations are expected to have better performance and more accurate estimations, they are very sensitive to input variables. So that, in a situation corresponding to the transition zone (where the characteristics of the particle suspension are not well defined), an inaccurate assumption about these characteristics may lead to large uncertainties in the simulations when $RRTMG_{sw}$ or NGO_{sw} are applied ($\overline{R\Delta RE}_t$>102%,). Whereas, the uncertainties obtained from different assumptions of the transition zone are smaller (but still substantial, $\overline{R\Delta RE}_t$>50%) when the simpler parameterization FLG_{sw} is utilized. These findings encourage further investigation on the transition zone from different aspects: (i) developing automated methods for detection of a situation regarding to transition zone (based on surface/satellite measurements) to facilitate studying the its actual radiative effects, (ii) the role and effects of transition zone in the Earth climate system, (iii) exploring the radiative effects of the transition zone in the longwave range, (iv) influence of not considering the transition zone on model dynamics.

Chapter 5

Transition Zone Radiative effects in Longwave Radiation Parameterizations

This chapter is a transcript of the paper:

Jahani, B., Calbó, J., & González, J.A. (2020). Quantifying Transition Zone Radiative Effects in Longwave Radiation Parameterizations. *Geophysical Research Letters 47 (22), e2020GL090408*. doi: https://doi.org/10.1029/2020GL090408

The changes applied consist of:

Modifying some symbols as well as figure and table labeling and numbering for the sake of consistency with the whole thesis document. In addition, the literature cited in this transcript has also been moved to the final chapter of this document (References), in order to have all used references together.

Summary

The change in the state of sky from cloudy to cloudless (or vice versa) comprises an additional phase called "transition zone", in which the characteristics of the particle suspension lay between those corresponding to pure clouds and atmospheric aerosols. This phase, however, is usually considered, in atmospheric monitoring and modelling, as an area containing either aerosol or thin clouds. A sensitivity analysis has been performed to assess the longwave radiative effects resulting from different approximations to the transition zone for three radiation parameterizations included in the Weather Research and Forecasting Model. The parameterizations produce important differences (up to 60 Wm^{-2}) between radiative effects of optically thin layers of aerosols and clouds (as surrogates for transition zone suspensions) in the longwave region, both at the top and bottom of the atmosphere. Also, differences are greater if the suspension of particles is located at higher altitudes, but smaller in high humidity conditions.

5.1 Introduction

Aerosols and clouds, as two particular cases of a single phenomenon (i.e. a suspension of particles in the air) are important components in the climate system. They significantly affect the Earth energy budget by scattering, absorbing and emitting radiation in the atmosphere. Although aerosols and clouds interact and affect each other's properties, their radiative properties and effects are usually treated separately in climate, meteorological and weather forecasting studies (Redemann et al., 2009; Várnai et al., 2017; Spencer et al., 2019). Thus, in such studies usually a discrimination between the cloudy and non-cloudy sky (which contains a certain aerosol load) is required.

In theory, there are distinct differences between characteristics and origin of fully developed clouds and aerosols, which makes it possible to distinguish them from each other (Platnick et al., 2003; Liu et al., 2009; Michalsky et al., 2010). However, what is categorized as a cloud based on one method may be categorized differently based on another. Additionally, there are some conditions at which regardless of the method utilized, discrimination among them becomes challenging (Wollner et al., 2014; Fuchs & Cermak, 2015; Calbó et al., 2017). Specifically, the change in the state of sky from cloudy to cloudless (or vice versa) occurs gradually, and it comprises an additional phase called "transition zone" (or "twilight zone"). At this phase, the microphysical and radiative characteristics of the suspended particles in the atmosphere are in transition between those corresponding to a pure cloud and those corresponding to pure atmospheric aerosols (Koren et al., 2007, 2009). Based on three ground-based observation systems at two mid-latitude sites, Calbó et al. (2017) found that the transition zone produces typically an optical depth of less than 0.32 (at 0.500 μm wavelength), but it might be found for optical depth as high as 2.00. The transition zone may correspond to different processes/suspensions: hydration and dehydration of aerosols, cloud fragments sheared off from the adjacent clouds, decaying and incipient clouds, pockets of high humidity that oscillate near saturation (Koren et al., 2009). It has been found that at any time, a large proportion of sky contains particle suspensions with characteristics of the transition zone (Charlson et al., 2007; Koren et al., 2009; Várnai & Marshak, 2011; Wollner et al., 2014; Calbó et al., 2017; Schwarz et al., 2017). Nevertheless, the vast area that potentially may represent the transition zone is usually neglected and assumed as an area that contains either aerosols or optically thin clouds. In other words, radiative and optical properties

corresponding to clear- or cloudy-sky are misleadingly used to characterize such transition zone conditions.

This simplified assumption about the state of the sky rises the question “how different the radiative effects will be, if an atmospheric layer containing a suspension of particles corresponding to transition zone is assumed as a cloud or as an aerosol layer?” It was found by Jahani et al. (2019) that under ideal conditions, this assumption may lead to substantial differences in the broadband surface shortwave radiative effects simulated by the radiation parameterizations included in the Advanced Research Weather Research and Forecasting model (WRF-ARW). The uncertainties risen from different approximations (describing a situation corresponding to the transition zone as cloud or as aerosol) in the longwave region, however, remain undescribed to our knowledge. For this reason, the current study aims to quantify these uncertainties by applying a sensitivity analysis, for some of the longwave radiation (*lwrad*) parameterizations included in WRF-ARW.

5.2 Materials and Methods

5.2.1 Model Description

WRF-ARW is a widely used mesoscale atmospheric model, developed for both research and operational weather forecasting purposes (Powers et al., 2017). There are seven *lwrad* parameterizations included in this model. These parameterizations are also shared with the Model for Prediction Across Scales (MPAS, Ha et al., 2017), which is intended to replace WRF. Among them, three parameterizations which are capable of dealing with aerosol radiative effects in the longwave band were separated from the model structure and adapted for idealized one-dimensional vertical simulations (“sandbox” approach): Fu-Liou-Gu (FLG_{lw}, Gu et al., 2011), Rapid Radiative Transfer Model for General Circulation Models ($RRTMG_{lw}$, Iacono et al., 2008) and New Goddard (NGO_{lw}, Chou & Suarez, 1999). These parameterizations were then used to simulate the downwelling longwave irradiance ($E\downarrow$) and the upwelling longwave irradiance ($E\uparrow$) at the model levels, including ground surface ($E_{bot}\downarrow$), and top of the atmosphere ($E_{top}\uparrow$). Throughout this paper, we give positive and negative sign to the physically downwelling and upwelling irradiances, respectively.

In the parameterization FLG_{lw}, the longwave region is divided into 12 spectral bands starting from 4.55 µm. In the case of the parameterizations $RRTMG_{lw}$ and NGO_{lw}, the longwave region starts from 3.33 µm and is divided into 16 and 10 spectral bands, respectively. These *lwrad* parameterizations use different methods for solving the Radiative Transfer Equation (*RTE*) and obtaining cloud optical properties. These methods are the same as the ones used by their corresponding shortwave schemes, which are described in Chou & Suarez (1999), Iacono et al. (2008) and Gu et al. (2011) respectively. These parameterizations are also different when dealing with the radiative effects of the aerosols and clouds. The parameterizations NGO_{lw} and FLG_{lw} deal with longwave scattering due to atmospheric particles (clouds and aerosols) and calculate their radiative effects based on their extinction coefficient (δ), single scattering albedo (ω) and asymmetry factor (g). In these two parameterizations, the band averaged values of δ, ω and g (at each layer) corresponding to aerosols are directly inputted to the *RTE* solver, whereas the band averaged cloud optical properties (δ, ω and g) at each level are calculated based on the input values of droplet/crystal effective radii, liquid/ice water mixing ratio and temperature, using the cloud parameterizations included in the *lwrad* parameterizations. In $RRTMG_{lw}$, however, cloud and aerosol optical depths (at each spectral band and layer) are the only relevant input to the *RTE* solver. Indeed, in $RRTMG_{lw}$, the atmosphere is assumed as a non-scattering medium (ω=0) and the diffusivity angle for all of the atmospheric components is assumed to be the same and is calculated (at each spectral band and layer) as a function of water vapor content.

5.2.2 Experiment setup

The methodology adopted for quantifying the uncertainties risen from different approximations (as cloud or aerosol) to the transition zone in the *lwrad* parameterizations consists of: (i) considering cloud- and aerosol-free atmospheres as reference setups, (ii) using the isolated radiation parameterizations to simulate longwave irradiances (upwelling and downwelling) by adding homogeneous layers of cloud –resulting from different combinations of crystal/droplet sizes and liquid/ice water content– or aerosol –with different optical characteristics– to the reference setup, (iii) calculating the radiative effects (RE, W m^{-2}) due to the different cloud/aerosol layers, (iv) analyzing differences in the simulated REs for both $E_{bot}\downarrow$ (hereafter denoted as $RE_{bot}\downarrow$)

and $E_{top}\uparrow$ ($RE_{top}\uparrow$). Here, the term "uncertainty" is defined as the range of REs resulting from describing a situation corresponding to the transition zone as cloud or as aerosol. This methodology is based on the assumption that the radiative effects of the particles with the characteristics of the transition zone are between those corresponding to aerosols and clouds and thus, the uncertainty calculated this way should be greater than (and hence cover) the difference between the transition zone and pure cloud or aerosol suspensions.

In a cloud- and aerosol-free atmosphere the *lwrad* transfer is dominated by the tropospheric water vapor, due to the spectral extent of its absorbing properties (Clough & Iacono, 1995). Additionally, the amount of *lwrad* emitted by the atmospheric particles/molecules and by the Earth surface is highly affected by temperature. For these reasons, the present study was carried out under both winter and summer conditions. To this aim, the standard mid-latitude cloud- and aerosol-free summer and winter atmosphere profiles given in Anderson et al. (1986), were considered as the reference setups. For other atmospheric gases (O_3, CO_2, …), the precribed profiles included in the parameterizations were used. In all simulations, the model surface and top were set at 0 and 30 km respectively and the atmospheric column was divided in 30 layers with equal physical thickness (1 km for each layer). The surface emissivity was fixed to 0.97.

The clouds considered in this study consist of: (i) ice clouds (physical thickness: 1 km, altitude: between 7-8 km) with crystal effective radii (r_e) ranging between 10 and 120 µm, and (ii) liquid clouds (physical thickness: 1 km, altitude: between 1-2 km) with droplet r_e ranging between 2.5 and 15 µm. The aerosols used consist of six typical aerosol models described in OPAC (Optical Properties of Aerosols and Clouds) aerosol data base (Hess et al., 1998), at different hydration stages (relative humidity: 70-99%): (i) urban; (ii) continental-clean; (iii) continental-average; (vi) continental-polluted; (v) maritime-clean; and (vi) maritime-polluted. The spectral data regarding to aerosol optical properties (extinction coefficient, δ_λ; single scattering albedo, ω_λ; asymmetry factor, g_λ) obtained from OPAC (provided in 61 wavelengths between 0.25-40.00 µm) was then transformed to band averaged values according to the spectral bands of the parameterizations. Figure 5.1 illustrates the spectral optical characteristics corresponding to the example of continental-average, maritime-clean and urban aerosol models at relative humidities

equal to 70 and 99%. In this figure, δ_λ values correspond to the particle concentrations which produce an optical depth at the 0.550 μm wavelength (τ) equal to 1.00 (assuming a physical thickness of 1 km). This figure shows that the continental-average and urban aerosol models described in Hess et al. (1998) have similar optical properties, specially at higher hydration levels. This is mainly because both aerosol models are a composition of three aerosol components: insoluble, soot and water-soluble (with only slight different volumetric mixing ratios at the hydrations levels illustrated here) and for both models, the absorption and the scattering cross sections are dominated by the components water-soluble and insoluble, respectively. The size distribution of the particles in these two aerosol models are also similar, but different compared to the maritime-clean aerosol model. The aerosols were placed in single layers with altitudes between 7-8 km and between 1-2 km (physical thickness for the layers at both altitudes: 1 km) for comparison with ice (comparison I-a) and liquid (comparison L-a) clouds, respectively.

In all simulations, the τ assigned to either cloud or aerosol layers (here τ only refers to cloud/aerosol and does not account for the other atmospheric components) was considered to vary between 0.01 and 2.00. This range of τ covers low and high values of τ which can potentially represent a transition zone situation (Calbó et al., 2017) and is also consistent with the range considered in Jahani et al. (2019). For the aerosol layers, the variation in τ was addressed through changing total number concentration of the aerosol particles until obtaining the desired τ (at the band that contains the 0.550 μm wavelength). The values of τ at other spectral bands were determined by multiplying the τ at 0.550 μm by the ratio between τ at the desired band and that at 0.550 μm in the original OPAC data-base. In case of the cloud layers, as each parameterization uses different methods for determination of the cloud optical properties (these methods are different in many ways, including number of bins considered for r_e, size distribution of the droplets/crystals in the cloud, data bases utilized, etc.), for each droplet/crystal size, cloud τ was obtained through trial and error: fixing droplet/crystal size and increasing/decreasing water/ice mixing ratio until obtaining the desired τ (at the band that contains the 0.550 μm wavelength) with a maximum error of ±1%.

The radiative effect of each of the mentioned cloud/aerosol layers on any irradiance *irr* (downwelling or upwelling) at any model level, simulated by each parameterization *par*, for a given τ, ($RE_{irr,par}(\tau)$) was calculated according to Eq. 5.1:

$$RE_{irr,par}(\tau) = E_{irr,par}(\tau) - E_{irr,par}(0) \qquad \textit{Eq. 5.1}$$

The irradiance $E_{irr,par}(0)$ corresponds to the simulation for the reference setups (i.e., clean and clear, summer and winter, atmospheres).

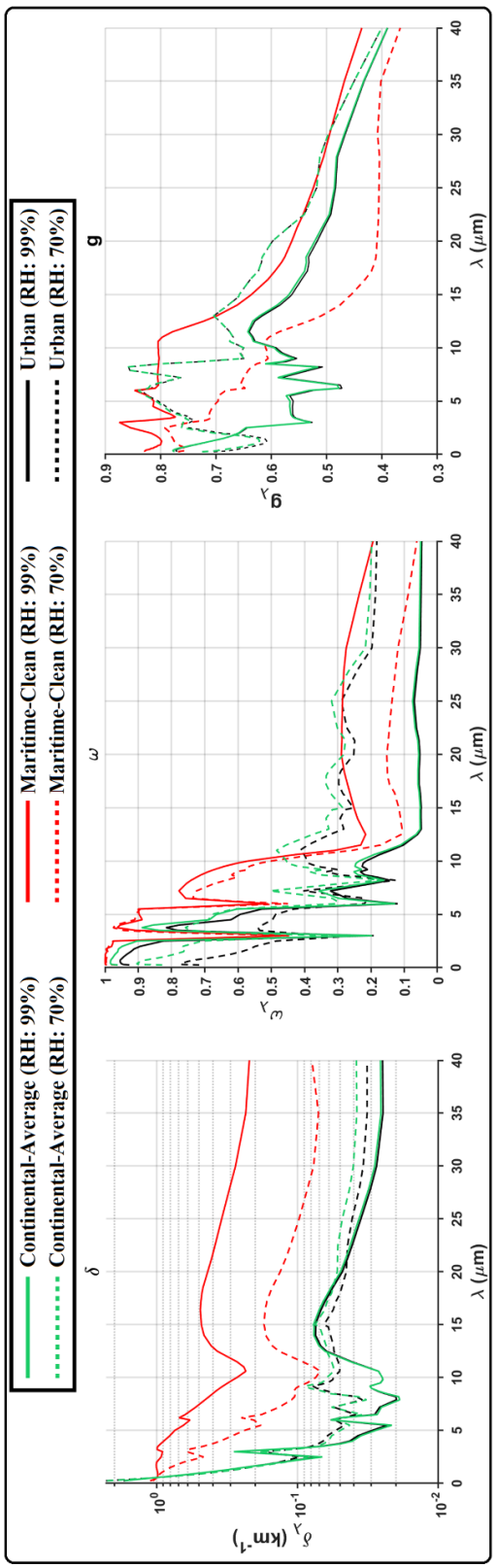

Figure 5.1. Spectral optical characteristics (extinction coefficient, δ_λ; single scattering albedo, ω_λ; asymmetry factor, g_λ) corresponding to continental-average, maritime-clean and urban aerosol models at relative humidities equal to 70 and 99% as described in (Hess et al., 1998) for $\tau_{0.550}$ =1.00. (Source: Jahani et al., 2020)

5.3 Radiative Effects

Vertical profiles of the downwelling ($E\downarrow$, positive values) and upwelling ($E\uparrow$, negative values) longwave irradiances simulated by the parameterizations NGO_{lw}, FLG_{lw} and $RRTMG_{lw}$ under reference setups are provided in Figure 5.2. According to Figure 5.2, both $E_{top}\uparrow$ and $E_{bot}\downarrow$ are much larger (in absolute sense) in summer than in winter, because of higher temperatures and larger water vapor amount in the whole atmosphere. Furthermore, as expected for both summer and winter setups, most changes in $E\uparrow$ and $E\downarrow$ occur in the troposphere (i.e. below 12-15 km). This figure also reveals that the differences among the irradiances simulated by FLG_{lw} and NGO_{lw} are very tiny (<3.8 Wm^{-2}), while larger differences are visible with those simulated by $RRTMG_{lw}$. Specifically, $RRTMG_{lw}$ simulates less (absolute) $E\uparrow$ and more $E\downarrow$ compared with FLG_{lw} and NGO_{lw}. The reason for this difference, to a large extent, is the different treatment of diffusivity angle: in $RRTMG_{lw}$ is computed for all atmospheric components as a function of total column water vapor content (Iacono et al., 2008), whereas in FLG_{lw} and NGO_{lw}, it is determined according their asymmetry factor.

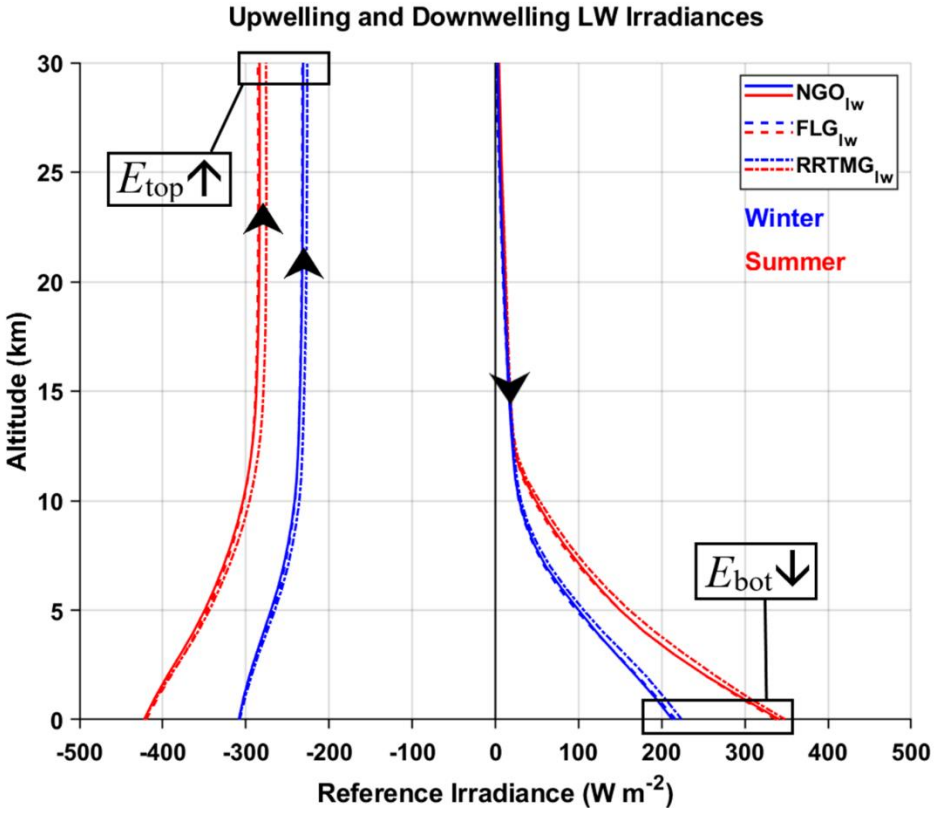

Figure 5.2. Vertical profiles of the downwelling ($E\downarrow$) and upwelling ($E\uparrow$) *lwrad* simulated by the parameterizations NGO_{lw}, FLG_{lw} and $RRTMG_{lw}$ for the summer (red lines) and winter (blue lines) reference setups. (Source: Jahani et al., 2020)

Figure 5.3 shows the values of $RE_{bot}\downarrow$ and $RE_{top}\uparrow$ resulting from different approximations to the transition zone (describing a situation corresponding to the transition zone as cloud or as aerosol) for τ = 0.01-2.00, based on the three parameterizations. In this figure, the upper panel is dedicated to the comparison between the RE of high (ice) clouds and aerosols (comparison I-a), and the lower panel to the comparison between the RE of low (liquid) clouds and aerosols (comparison L-a). In each single plot, the lines of the same type and color mark the maximum and minimum possible values of $RE_{bot}\downarrow$ (blue) and $RE_{top}\uparrow$ (black) due to different cloud (dashed lines) or aerosol (solid lines) approximations. In each single plot, the lower and upper colored areas represent the uncertainty (associated with describing a situation corresponding to the transition zone as cloud or aerosol), which we define here as the range ($\Delta RE_{bot}\downarrow$, blue) of the values of $RE_{bot}\downarrow$ (actually accounting for the uncertainty in $E_{bot}\downarrow$) and the range ($\Delta RE_{top}\uparrow$, pink) of the values of $RE_{top}\uparrow$ (accounting for the uncertainty in $E_{top}\uparrow$). For all parameterizations, adding a cloud/aerosol layer with any τ results in positive $RE_{bot}\downarrow$ and $RE_{top}\uparrow$. In other words, it causes an increase in $E_{bot}\downarrow$ (positive sign, as downwelling) but a reduction in $E_{top}\uparrow$ (negative sign, as upwelling) compared to their corresponding reference irradiances. The increase in $E_{bot}\downarrow$ is due to the downward emission from cloud/aerosol layer, which (despite being far from a blackbody, as the amount of suspended particles is relatively small given the low range of τ considered) is performed at a temperature higher than the brightness temperature of the clear atmosphere. The reduction in the absolute value of $E_{top}\uparrow$ is because the upward emission of the layer is performed at a temperature which is lower than that of the ground, and also due to the fact that cloud/aerosol layer is absorbing some of the $E\uparrow$ emitted by the surface.

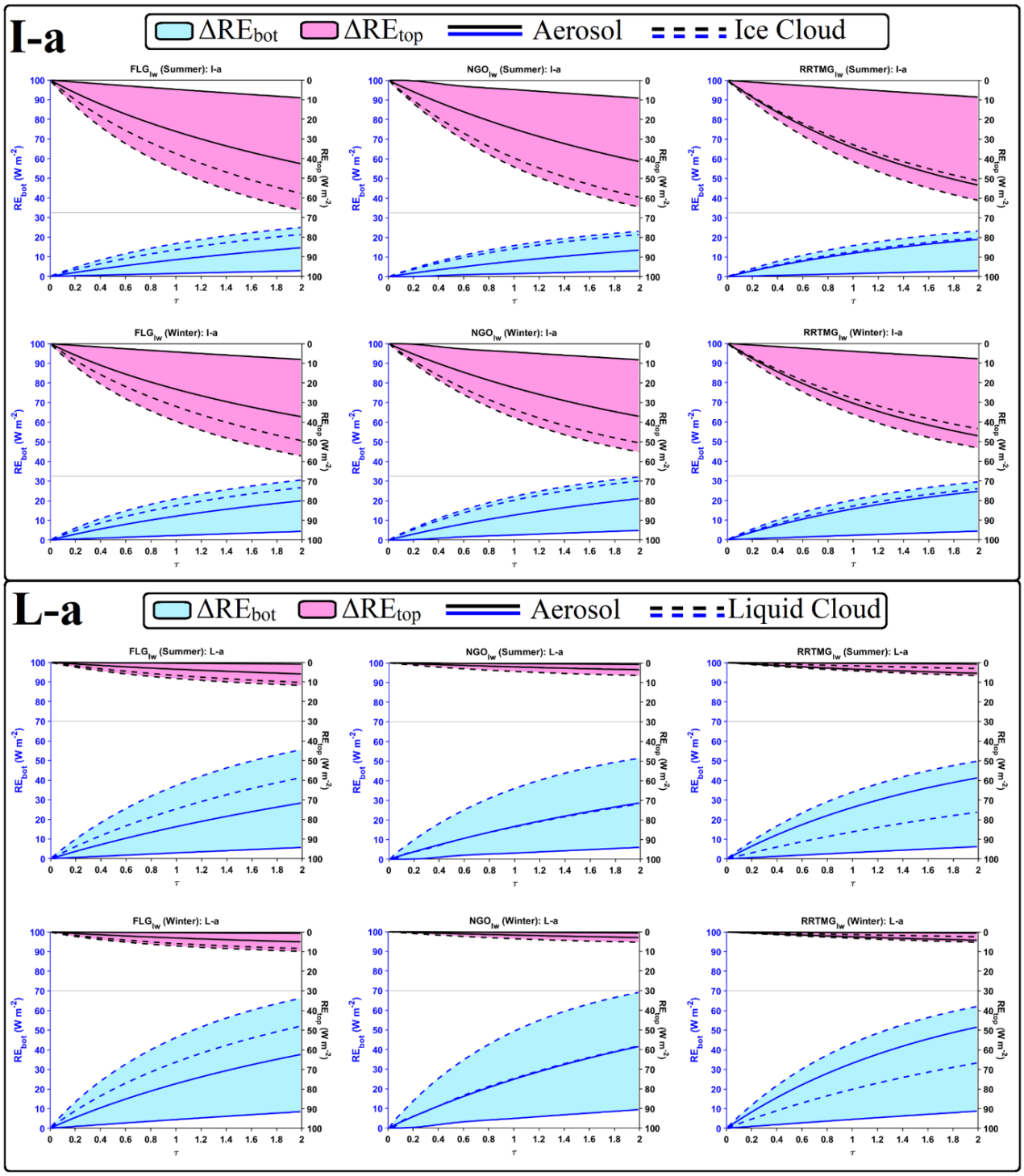

Figure 5.3. The simulated values of $RE_{bot}\downarrow$ (blue lines, left axis) and $RE_{top}\uparrow$ (black lines, right axis) resulted from different approximations to the transition zone versus $\tau_{0.550}$ (0.01-2.00) for winter and summer atmospheric profiles based on FLG_{lw}, NGO_{lw} and $RRTMG_{lw}$ simulations. (note: upper panel corresponds to the case "I-a" and the lower panel to "L-a"). (Source: Jahani et al., 2020)

In Figure 5.3 some small differences between the cloud REs simulated by the parameterizations FLG_{lw} and NGO_{lw} are evident. They originate from the difference in the methods used by the parameterizations for solving the RTE, obtaining the cloud optical properties, as well as the number and limits of the spectral bands used. However, despite these differences, the results obtained from FLG_{lw} and NGO_{lw} show that, under all tested conditions, there are distinct and important differences between the REs of aerosols and clouds in the longwave region, which are evident in both $RE_{bot}\downarrow$ and $RE_{top}\uparrow$. This means that assuming a condition corresponding to the transition zone as cloud or aerosol may cause large uncertainties (up to 60.0 Wm^{-2} for τ = 2.00, the largest optical depth studied here) in the simulation of $RE_{bot}\downarrow$ and $RE_{top}\uparrow$. This uncertainty seems to be small compared to what was reported in Jahani et al. (2019) for the shortwave radiation. However, it is a rather noticeable value when compared to the $E_{bot}\downarrow$ (217-338 Wm^{-2}) and $E_{top}\uparrow$ (232-286 Wm^{-2}) for the reference setups (Figure 5.2), which are the result of the emission and absorption by atmospheric gases. According to Figure 5.3, even at a relatively low τ of 0.1, $\Delta RE_{bot}\downarrow$ ranges (depending on layer height and season) between 2.2-6.6 Wm^{-2} and 2.2-7.2 Wm^{-2} based on FLG_{lw} and NGO_{lw} simulations, respectively. At the same τ, $\Delta RE_{top}\uparrow$ comprises 1.2-6.5 Wm^{-2} and 0.5-6.1 Wm^{-2} based on FLG_{lw} and NGO_{lw} simulations, respectively. However, it is worth mentioning that results obtained from NGO_{lw} show that there are cases where REs of clouds and aerosols may overlap: liquid clouds with small droplets (r_e: 2.5 µm) and highly hydrated maritime aerosols (relative humidity: 99%; r_e: 2.3-3.0 µm).

The results obtained from $RRTMG_{lw}$, however, are somewhat different from those obtained from FLG_{lw} and NGO_{lw}. According to $RRTMG_{lw}$ simulations, large hydrated aerosols (r_e: 2.3-3.0 µm) produce REs similar to ice/liquid clouds with crystal/droplet r_e as large as 10.0 µm, which results in a smaller range of RE and thus lower uncertainties compared to FLG_{lw} and NGO_{lw} (< 45.0 Wm^{-2} for τ = 2.00). This is mainly because $RRTMG_{lw}$ deals with *lwrad* in less details compared with FLG_{lw} and NGO_{lw}. Specifically, in this parameterization, longwave scattering due to clouds and aerosols is neglected (ω=0), and the spectral behavior of the extinction coefficient is considered as the only source of difference among clouds and aerosols of different type. Due to the simplicity of $RRTMG_{lw}$ in dealing with *lwrad* in comparison with the two other parameterizations, hereafter discussion about transition zone REs will mainly be addressed according to the results obtained from FLG_{lw} and NGO_{lw}.

Figure 5.3 also shows that for the range of τ studied and in both seasons, the values of $RE_{top}\uparrow$ and $\Delta RE_{top}\uparrow$ simulated under the case I-a are always greater than those of the case L-a. This is consistent with the results of Mishra et al. (2015) and Mitchell & Finnegan (2009) and means that the higher the layer (where cloud-aerosol confusion happens) is, the greater the uncertainties in the simulation of $E_{top}\uparrow$ are. Thus, as the amount of $E\downarrow$ at the top of the atmosphere is negligible, transition zone conditions at high altitudes will contribute to larger uncertainties in the determination of the longwave radiative forcing and the atmospheric cooling rate. Correspondingly, the $\Delta RE_{bot}\downarrow$ simulated by both parameterizations under the case L-a is always greater than that of the case I-a. Detailed information about the vertical behavior of RE at different levels of the atmosphere (in particular at the levels just above and below the cloud/aerosol layers) for the example of $\tau = 1.00$ is provided in Figure 5.4. According to this figure, the values of ΔREs (both upwelling and downwelling) at top and base of the cloud/aerosol layers are indeed greater under case I-a compared to L-a. The reason for smaller $RE_{bot}\downarrow$ in the case I-a is that the emitted radiation needs to pass through a (physically and optically) thicker path in the troposphere and thus is subjected to a greater absorption. As a result, the $E\downarrow$ emitted under I-a cases is more strongly attenuated. Furthermore, as Figure 5.4 shows, for both comparison cases the absorption is even stronger in the layers beneath the cloud/aerosol layers in summer, which is due to larger amount of water vapor in the summer setup (Clough & Iacono, 1995).

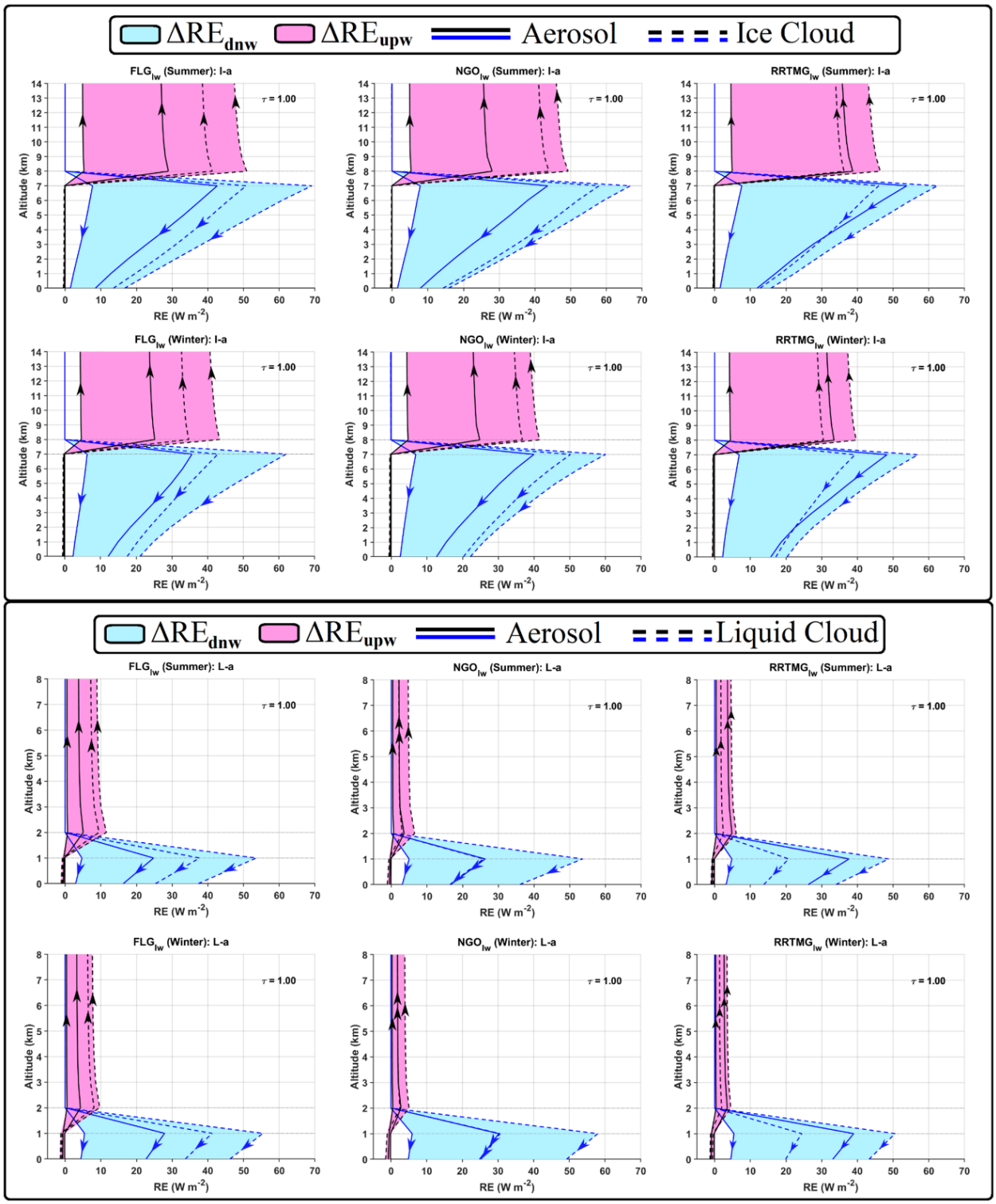

Figure 5.4. Vertical profiles of RE (downwelling: blue lines, upwelling: black lines) for winter and summer atmospheric profiles based on FLG_{lw}, NGO_{lw} and $RRTMG_{lw}$ simulations at $\tau_{0.550}$ = 1.00 for I-a (upper panel) and L-a (lower panel) comparison cases (note: the vertical scale of the figures in the lower and upper panel is not the same). The areas colored in blue and pink mark the uncertainty (associated with describing a situation corresponding to the transition zone as cloud or aerosol) in the downwelling and upwelling irradiances, respectively. (Source: Jahani et al., 2020)

5.4 Conclusions and discussions

This study has shown that for the range of τ studied (0.01-2.00), there are some differences between parameterizations NGO_{lw} and FLG_{lw} regarding the magnitude of the simulated irradiances, which however, lead to very similar radiative effect ranges (ΔREs, used as an approximation to uncertainties). $RRTMG_{lw}$, on its side, produces somewhat different irradiances, which result in slightly lower radiative effect ranges. For all parameterizations, when adding a cloud/aerosol layer (with any τ), $E_{top}\uparrow$ decreases (in absolute value), because the upward emission of the layer is performed at a temperature which is lower than that of the ground and $E_{bot}\downarrow$ increases (due to the downward emission from cloud/aerosol layer), resulting in positive $RE_{bot}\downarrow$ and $RE_{top}\uparrow$. The REs simulated by NGO_{lw} and FLG_{lw} show that, under all tested conditions, there are distinct and important differences between the REs of aerosol and clouds in the longwave region, which may result in uncertainties up to ~60 Wm^{-2} at τ = 2.00. Even at very small τ of 0.10, assuming a situation corresponding to the transition zone as cloud or aerosol may lead to a noticeable amount of $\Delta RE_{top}\uparrow$ (0.5-6.5 Wm^{-2}, values depending on layer height and season) and $\Delta RE_{bot}\downarrow$ (2.2-7.2 Wm^{-2}). Although this uncertainty has been computed from physical modelling and refers only to local and temporary effects, it deserve to receive attention, because transition zone conditions may affect a vast area of the global atmosphere, therefore a significant proportion of sky at any time is covered with such a particle suspension according with several studies (Calbó et al., 2017; Fuchs & Cermak, 2015; Koren et al., 2007; Schwarz et al., 2017). This amount of uncertainty over a large area may add incertitude to, or explain a part of the doubts associated with, the description of global energy balance and its evolution in combination with the effects of other atmospheric components, such as the well-mixed anthropogenic greenhouse gases (which have produced a global scale radiative forcing of 2.83 ± 0.29 Wm^{-2} over 1750-2011; Myhre et al., 2013).

The results also suggest that different approximations to the transition zone for a suspension of particles at higher altitudes have large impacts on the energy budget in the whole column of the atmosphere. In contrast, different approximations to the transition zone at lower altitudes mainly affects the surface energy budget. The results obtained in this study underline the importance of the transition zone in the longwave spectral region and show that different approximations (as cloud or aerosol) to the transition zone may introduce relatively large uncertainties to our understanding about the energy balance in the

atmosphere. This is so because a discrimination about the cloudy and cloud-free skies is required in climate studies, but in many of them the area corresponding to the transition zone is either categorized as cloud or aerosol. It should be noted that these uncertainties are not limited to observational studies, because the data obtained from observations are used for running the atmospheric models. This means that even if a certain model is capable of treating clouds and aerosols as continuum fields, the error in the initial input data may introduce large uncertainties to how energy is transferred in different layers of the model, which, through heating/cooling rates, may significantly affect the model dynamics. Also, a comparison between the simulations of the three parameterizations show that even though the interactions between clouds and aerosols may be well defined in the microphysical schemes of a weather forecasting model, the interactions of the supensions of particles (clouds, aerosols -more or less hydrated-) with radiation may be defined differently in the radiation schemes: in NGO_{lw}, liquid clouds with small droplets (r_e: 2.5 µm) and highly hydrated maritime aerosols (r_e: 2.2.3-3.0 µm) produce very similar REs; whereas, in FLG_{lw}, there is no overlap between the REs of the aerosols and clouds; and in $RRTMG_{lw}$ the REs simulated for large hydrated aerosols (r_e: 2.3-3.0 µm) are similar to those of ice and liquid clouds with crystal/droplet sizes as large as 10.0 µm.

These findings and those obtained by Jahani et al. (2019) for the shortwave region encourage studying the links between these differences in the shortwave and longwave REs and model dynamics. These uncertainties associated with the transition zone REs show the need of defining an additional intermediate phase between the cloudy and clear skies; alternatively, a continuous treatment of such suspensions of particles (from pure, dry aerosols to typical clouds), as well as their co-existence in some situations could also be habilitated in the radiation parameterizations. This may be done through introducing a new set of optical properties for transition zone in models based on the observations, an interpolation between the radiative/optical properties of hydrated aerosols and clouds (some adjusted size distributions laying between those typical of aerosol and those typical for clouds), or including in the parameterizations the aerosol optical properties for relative humidities close to and above saturation. All of these proposals, however, may eventually require defining an index (or a set of indices) to decide about the phase of the particles (aerosol, transition zone and cloud). Also, studying the radiative behavior of particle suspensions at the transition zone, as

well as exploring the size distribution and the composition of particles in the regions around the clouds based on in-situ measurements may help researchers to identify such cases. Moreover, it should be noticed that the present study is rather theoretical and limited to (i) two mid-latitude atmospheric profiles, (ii) six aerosol types (with characteristics that may be incompatible with their vertical position and relative humidity < 100%), (iii) homogeneous vertical layers of clouds and aerosols. Thus, the transition zone REs under real conditions (including three-dimensional effects) as well as their effect on the climate system, still need to be further investigated.

Chapter 6

Transition Zone Actual longwave radiative effects Based on Satellite Observations

This chapter is a transcript of the pre-print paper:

Jahani, B., Andersen, H., Calbó, J., González, J.A., Cermak, J. (2021) Longwave Radiative Effect of the Cloud-Aerosol Transition Zone Based on CERES Observations. *Atmospheric Chemistry and Physics Discussions*. doi: https://doi.org/10.5194/acp-2021-421

The changes applied consist of:

Modifying some symbols as well as figure and table labeling and numbering for the sake of consistency with the whole thesis document. In addition, the literature cited in this transcript has also been moved to the final chapter of this document (References), in order to have all used references together.

Summary

This study presents an approach for quantification of cloud-aerosol transition zone broadband longwave radiative effects at the top of the atmosphere (TOA) during daytime over the ocean, based on satellite observations and radiative transfer simulation. Specifically, we used several products from MODIS (Moderate Resolution Imaging Spectroradiometer) and CERES (Clouds and the Earth's Radiant Energy System) sensors for identification and selection of CERES footprints with horizontally homogeneous transition zone and clear-sky conditions. For the selected transition zone footprints, radiative effect was calculated as the difference between the instantaneous CERES TOA upwelling broadband longwave radiance observations and corresponding clear-sky radiance simulations. The clear-sky radiances were simulated using the Santa Barbara DISORT Atmospheric Radiative Transfer model fed by the hourly ERA5 reanalysis (fifth generation ECMWF reanalysis) atmospheric and surface data. The CERES radiance observations corresponding to the clear-sky footprints detected were also used for validating the simulated clear-sky radiances. We tested this approach using the radiative measurements made by the MODIS and CERES instruments onboard Aqua platform over the south-eastern Atlantic Ocean during August 2010. For the studied period and domain, transition zone radiative effect (given in flux units) is on average equal to 8.0 $\pm$ 3.7 W m^{-2} (heating effect; median: 5.4 W m^{-2}), although cases with radiative effects as large as 50 W m^{-2} were found.

6.1 Introduction

Cloud and aerosol are the particular names for two specific particle suspensions in the atmosphere, which have been widely studied but continue to contribute the largest uncertainty to estimates and interpretations of the Earth's changing energy budget (Boucher et al., 2013). One of the sources of this uncertainty is the fact that they are univocally differentiated in the atmospheric science, whereas clouds and aerosols co-exist and often interact with each other, making it hard to study the effects of one regardless of the other. For instance, aerosols in the vicinity of clouds are usually hydrated in part, and their size distribution and thus their optical characteristics change relative to their dry counterpart (Várnai & Marshak, 2011). On the other hand, aerosols also affect cloud optical and microphysical properties through acting as cloud condensation nuclei and ice nucleating particles (Rosenfeld et al., 2014). Moreover, the decision on what a cloud is, or in other words where the boundaries of the clouds should be put, is a point of debate (Bar-Or et al., 2011; Calbó et al., 2017; Eytan et al., 2020; Fuchs & Cermak, 2015) and a suspension detected as cloud by one method may be labeled differently by another. This is due to the presence of a phase called the transition zone (or twilight zone) between the cloudy and so-called cloud-free skies, at which the characteristics of the suspension lay between those corresponding to the adjacent clouds and the surrounding aerosol (Koren et al., 2007; Várnai et al., 2013). This phase consists of a mixture of liquid droplets and humidified to dry aerosols, and involves various processes such as cloud dissipation/formation, aerosol hydration/dehydration, shearing of cloud fragments, clouds becoming undetectable, etc. (Eytan et al., 2020; Koren et al., 2009).

Observations have shown that transition zone occurs often over large areas. According to Koren et al. (2007), at any time almost 30-60% of the global atmosphere categorized as clear sky (cloud-free) can potentially contain this phase, which may expand up to 30 kilometers away from the detectable clouds (Bar-Or et al., 2011). On the basis of three ground-based observation systems, Calbó et al. (2017) quantified, at two mid-latitude sites, that the frequency of the transition zone was about 10%. A global analysis based on MODIS (Moderate Resolution Imaging Spectroradiometer) products performed by Schwarz et al. (2017) also suggests a frequency of 20% for the occurrence of the transition zone.

If the area covered with the suspension of particles with the characteristics of the transition zone is so vast, the question “what role does the transition zone play in the determination of the Earth’s energy budget?” takes a great importance. However, as the information available about the transition zone and its interactions with radiation (in both longwave and shortwave bands) is very limited, the area corresponding to the transition zone in climatic, meteorological, and atmospheric studies and models is usually considered as an area containing either aerosols or optically thin clouds. This means that either radiative properties of clouds or those of aerosols are used to describe the radiative properties of the transition zone. Based upon sensitivity analysis performed using radiative transfer parameterizations, two recent studies (Jahani et al. 2019, 2020) showed that this assumption may lead to substantial differences in the simulated broadband shortwave and longwave radiative effects. According to these studies, for some particular situations, at an optical depth of 0.1 (at 0.550 μm) the differences at surface and top of the atmosphere may be as large as 7.5 and 28 W m^{-2} in broadband longwave and total shortwave, respectively. Based upon an observational and statistical study, Eytan et al. (2020) estimated the top of the atmosphere (TOA) radiative effect of the transition zone around shallow warm clouds in the atmospheric window region (8.4-12.2 μm). They found that over the oceans on average the transition zone radiative effect in the mentioned spectral region is about 0.75 W m^{-2} (although they found cases with average radiative effects as large as 4 W m^{-2}), which is equal to the radiative forcing resulting from increasing atmospheric CO_2 by 75 ppm. The overall radiative effects of the transition zone are likely to be higher, as the radiative effect estimations given in the latter study correspond to a lower bound of the effect and are limited to the low-level (warm) transition zone conditions. These results highlight the importance of the characterization of the transition zone as well as of quantifying the role it plays in the determination of Earth’s energy budget.

Although the transition zone is frequently neglected in cloud-aerosol related studies, the above numbers and the vast area that potentially may contain the transition zone state give importance to the necessity of further exploring it. For this reason, within the frame of the study, a method for the quantification of the broadband longwave radiative effects of the transition zone at TOA over the ocean on the basis of instantaneous satellite observations and radiative transfer calculations is presented. This method is then applied over the South-

Eastern Atlantic Ocean, where cloudy conditions are frequent and hence transition zone conditions are also expected to be frequently observed.

6.2 Methods

6.2.1 Satellite Observations

The CERES (Clouds and the Earth's Radiant Energy System) sensor is a three-channel scanning radiometer measuring the broadband outgoing shortwave (0.3-5 µm), window-region (8-12 µm) and longwave (5-100 µm) radiances at TOA with a spatial resolution of ~20 km at nadir (Loeb et al., 2001; Priestley et al., 2011). The Level-2 Single Scanner Footprint (SSF) product of this instrument provides information about the instantaneous outgoing broadband longwave radiances at TOA regardless of the sky condition (Loeb et al., 2018; Loeb et al., 2006). From the SSF Level-2 product, we obtained the entire daytime instantaneous TOA outgoing broadband longwave radiance observations of the CERES instrument onboard Aqua spacecraft ($\uparrow L_{CERES}$) along with the corresponding time, geolocation, viewing geometry and surface emissivity parameters for August 2010 for the region comprised within 21° W-21° E and 10° N-50° S.

In addition, several products from the MODIS (Moderate Resolution Imaging Spectroradiometer) instrument onboard the same satellite (Aqua) were used for identification of horizontally homogenous clear-sky and transition zone conditions within CERES footprints. Specifically, we used the ocean products: (1) geolocation (MYD03, MODIS Characterization Support Team (MCST), 2017); (2) Aerosol-Cloud-Mask and Aerosol Optical Depth (AOD) taken from the Level-2 Aerosol (MYD04, Levy et al., 2015); (3) Cloud Optical Depth (COD) from the Level-2 Cloud (MYD06, Platnick et al., 2015); and (4) Cloud Mask (MYD35, Ackerman & Frey, 2015). These products were obtained for all MODIS-Aqua granules that contain data in the region 0° E-15° E and 10° S-30° S during August 2010, which their data spreads over the area between 21° W-21° E and 10° N-50° S. By combining these products, MODIS pixels were classified into the classes "Difficult", "Cloud", "Aerosol", "Clear", "Lost A", "Lost B", "Lost C" at 1-km resolution (at nadir) following the procedure explained in Schwarz et al. (2017). Among them, the pixels labeled as "Lost" are assumed to correspond to the transition zone conditions. Indeed, for these pixels neither aerosol nor cloud optical property retrievals exist, yet they are

classified as containing a cloud (Lost A), a non-cloud obstruction (Lost B), or were not processed at all in the cloud masking (Lost C).

The processed MODIS data was then integrated from 1-km resolution to CERES native resolution to determine the fraction of each class and the average values of COD and AOD in the CERES footprints, considering equal weights for all MODIS pixels. Afterwards, only CERES footprints meeting all the following conditions were used in the analysis: (i) solar zenith angles and CERES viewing zenith angles at surface lower than 60° (to mitigate the effect of uncertainties derived from viewing and solar geometries), (ii) no land MODIS pixels as determined using the MYD35 data is included, and (iii) number of ocean MODIS pixels more than or equal to 75% of the expected ~400 pixels falling within CERES field of view (FOV; to exclude FOVs located on the edges of the MODIS granules). Among the remaining footprints, those with a "Lost" fraction (all lost classes together) greater than or equal to 90% were classified as horizontally homogeneous transition zone footprints (the transition zone footprints selected this way, may contain up to 10% of cloud contamination). Also, those having AOD and COD equal to zero, "Lost" fraction less than 10%, and "Difficult" fraction less than 10% were classified as horizontally homogeneous clear-sky footprints. Based on this classification criterion, a total number of 5441 clear-sky and 3783 transition zone footprints were detected over the South-Eastern Atlantic Ocean in August 2010. The spatial distribution of these footprints is presented in Figure 6.1.

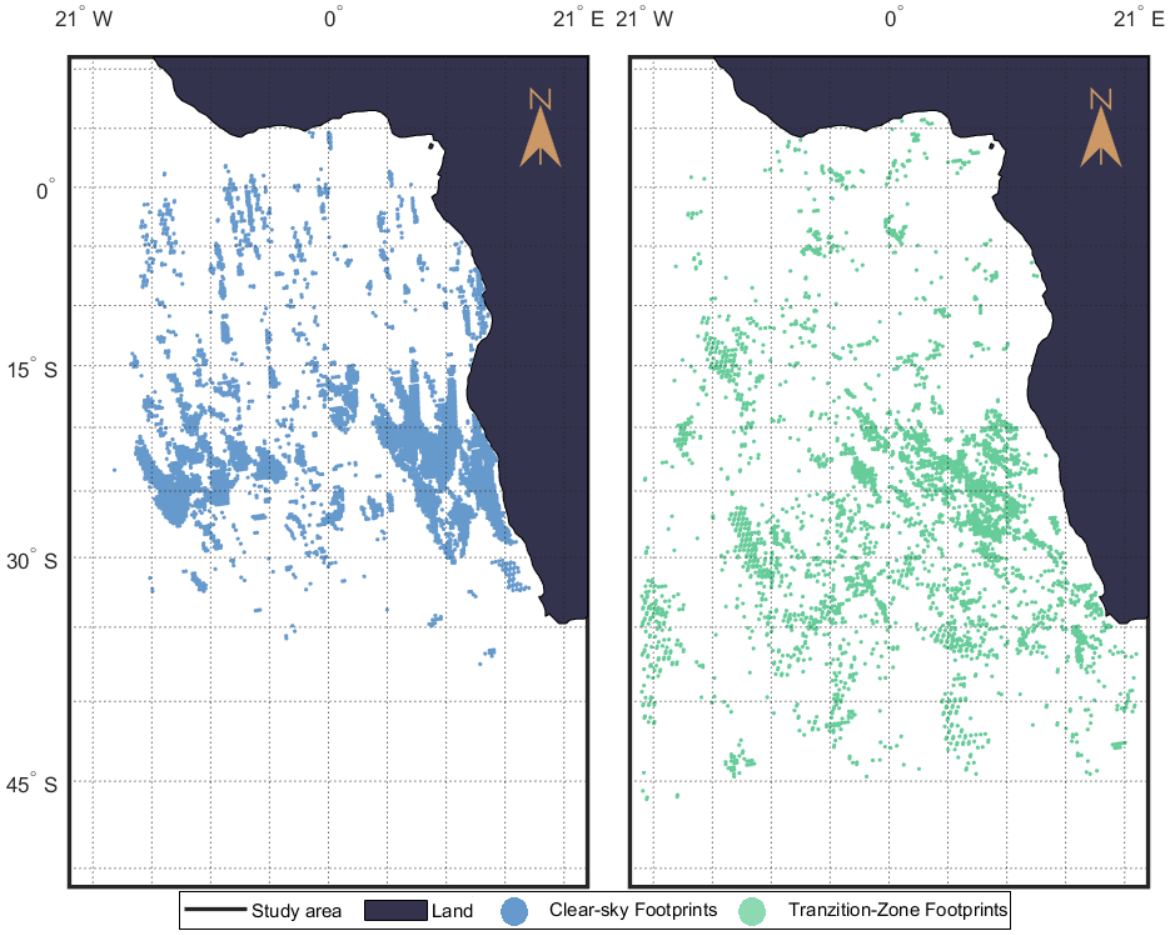

Figure 6.1. Spatial distribution of the clear-sky and transition zone CERES footprints detected within the study area (21° W-21° E, 10° N-50° S) in August 2010. (Source: Jahani et al., 2021)

6.2.2 Clear-sky simulations

For all transition zone and clear-sky footprints selected according to the criteria explained in section 6.2.1, the TOA upwelling broadband longwave (5-100 µm) clear-sky radiances ($\uparrow L_{RTM,clr}$) for the CERES viewing zenith angle (θ) were simulated using the Santa Barbara DISORT Atmospheric Radiative Transfer model (SBDART, Ricchiazzi et al., 1998), considering the effect of all atmospheric gases. The simulations were carried out by using atmospheric profiles (Hersbach et al., 2018a) and surface (Hersbach et al., 2018b) values provided by the fifth generation ECMWF reanalysis (ERA5), which render the data at 0.25°×0.25° spatial resolution and 1h time intervals. Specifically, profiles of specific humidity, geopotential height, ozone mass mixing ratio, and temperature at all available pressure levels (1000 hPa-1 hPa), as well as mean sea level pressure and 2 m air temperature and dewpoint temperature were used. For each (clear-sky/transition-zone)

footprint, the surface and atmospheric data of the closest ERA5 cell were combined with each other and linearly interpolated in time according to the CERES time of observation. The combined and interpolated profiles were then fed to SBDART for simulation of $\uparrow L_{RTM,clr}$. In these simulations, the broadband sea surface emissivity and the CO_2 concentration in atmosphere were set to the constant values of 0.982 (equal to the estimated broadband longwave sea surface emissivity included in the CERES SSF data; Geier et al., 2003) and 388.71 ppm (which is the value corresponding to the year 2010; European Environmental Agency: https://www.eea.europa.eu/, last access: 13 May 2021), respectively. As for the other gases the default concentration values included in SBDART model were used. For each individual clear-sky and transition zone footprint, SBDART model was ran with 20 zenithal streams and the spectral upwelling radiances (including the solar contribution, which actually is very low) were calculated in the range of 5-100 μm in steps of 0.2 μm. Then, the upwelling radiances at 30 km altitude at the SBDART computational zenithal angles were outputted and linearly interpolated to determine the magnitude of the upwelling radiance in the direction θ. Throughout this paper, we give negative sign to the physically upwelling radiances.

The simulated clear-sky radiances ($\uparrow L_{RTM,clr}$) were then validated through comparing them with the $\uparrow L_{CERES}$ values corresponding to the clear-sky footprints ($\uparrow L_{CERES,clr}$). The comparison was made using the corresponding isotropic irradiances ($\pi\uparrow L_{CERES,clr}$ and $\pi\uparrow L_{RTM,clr}$), and was based on the linear correlation coefficient between the simulated and the measured values, as well as by analyzing the probability distribution, mean and variance of the differences. First, for each individual clear-sky footprint, the difference between the calculated and observed clear-sky upward irradiances (ε_{clr}, W m^{-2}) was determined according to Eq. 6.1:

$$\varepsilon_{clr} = \pi\uparrow L_{RTM,clr} - \pi\uparrow L_{CERES,clr} \qquad \textit{Eq. 6.1}$$

Second, outliers were removed from the dataset by applying the quartiles method. Thus, among all clear-sky footprints (5441 footprints), those with a ε_{clr} more than 1.5 interquartile ranges above the upper quartile or below the lower quartile (197 footprints) were discarded. Statistical analysis of the ε_{clr} values corresponding to the remaining clear-sky footprints showed that $\pi\uparrow L_{RTM,clr}$ and $\pi\uparrow L_{CERES,clr}$ values are strongly correlated

(r^2 = 0.96) and that ε_{clr} values are normally distributed around the mean value (hereafter denoted as $\bar{\varepsilon}_{clr}$) of about 8.0 W m^{-2} with a standard deviation of about 1.9 W m^{-2}. The probability distribution of the ε_{clr} values around $\bar{\varepsilon}_{clr}$ and the scatter plot of $\pi\uparrow L_{CERES,clr}$ versus $\pi\uparrow L_{RTM,clr}$ values shifted by $\bar{\varepsilon}_{clr}$ are provided in Figure 6.2.

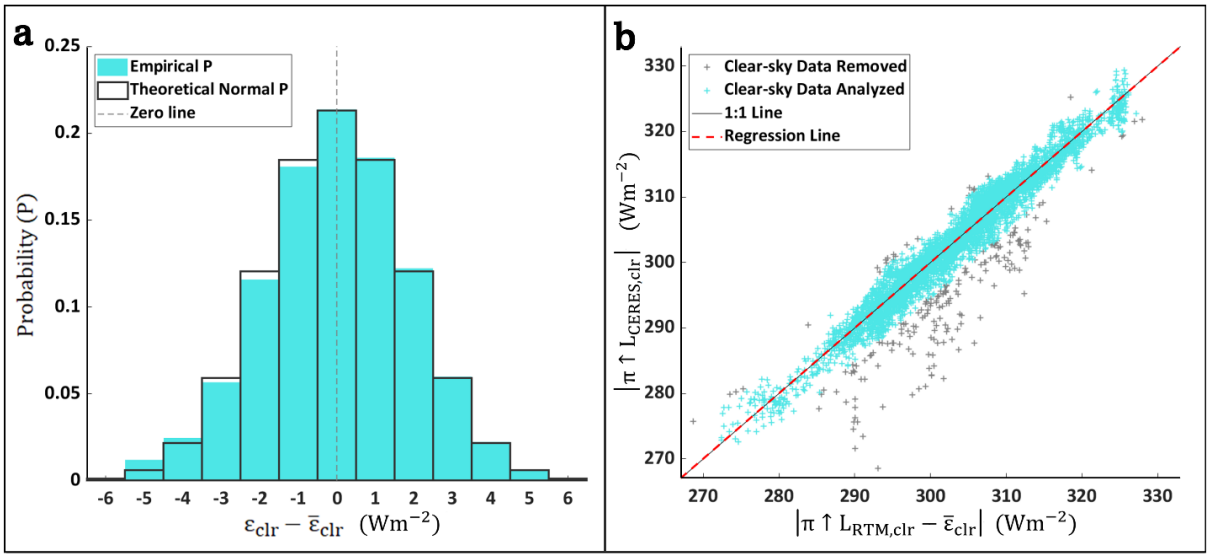

Figure 6.2. (a) Empirical (solid turquoise fill) and fitted theoretical normal (black lines) probability distributions of ε_{clr} around $\bar{\varepsilon}_{clr}$, (b) scatter plots of $\pi\uparrow L_{CERES,clr}$ versus $\pi\uparrow L_{RTM,clr}$ values shifted by $\bar{\varepsilon}_{clr}$ in absolute sense. In panel b, the gray points show the (outlier) data points discarded based on the quartile method. (Source: Jahani et al., 2021)

The facts that ε_{clr} values are normally distributed around $\bar{\varepsilon}_{clr}$ and that clear-sky observations and simulations are strongly correlated (and with a slope of the linear fit very close to 1) confirm that $\pi\uparrow L_{RTM,clr}$ values are systematically biased by about 8.0 W m^{-2} ($\bar{\varepsilon}_{clr}$) in comparison with the $\pi\uparrow L_{CERES,clr}$ values. As the upwelling irradiances/radiances are negative by definition, the bias found indicates an underestimation of the simulation in absolute terms. Also, the distribution of ε_{clr} values shows that a random disagreement of about ±3.7 W m^{-2} at 95% confidence level (two-tailed, $\varepsilon_{clr,95}$) exists between the clear-sky observations and simulations. The bias and the random disagreement must be due to the combined effect of the uncertainties associated with the data utilized and the assumptions made in the radiative transfer simulations (such as plane parallel atmosphere assumption, number of streams used in the calculations), the spectral resolution at which the radiative transfer calculations were performed (SBDART is based on LOWTRAN band models, and it was found by Wacker et al., (2009) that the spectrally integrated clear-sky downwelling longwave irradiances

simulated by LOWTRAN models is systematically 6 Wm^{-2} lower in comparison with line-by-line models or using the high resolution MODTRAN correlated-k bands), temporal and spatial matching of the ERA5 profiles with the CERES footprints, and the uncertainties associated with measuring the $\uparrow L_{CERES}$. According to Loeb et al. (2001), up to 0.2% of error with a standard deviation of 0.1% is associated with $\uparrow L_{CERES}$ which is indeed measured by subtracting the radiances received at the shortwave and total channels of the sensor with the appropriate spectral correction coefficients (not directly measured). Some proportion of this error could also be due to the longwave radiation scattered from the adjacent CERES footprints, which should be rather small as the magnitude of scattering by atmospheric particles for the wavelengths between 5 and 100 µm is rather neglectable. We tested the sensitivity of ε_{clr} values to the input surface temperature, water vapor mixing ratio profile, surface emissivity parameters, as well as the number of zenithal streams used in the radiative transfer calculations. We found that, as expected, ε_{clr} values vary considerably with very small changes in surface temperature (increasing/decreasing surface temperature by 1K will increase/reduce $\bar{\varepsilon}_{clr}$ by about 60%), whereas the effect of other parameters is very small. Given the fact that the temperature may notably vary in the first 2 meters of the atmosphere, the possible bias and uncertainties associated with the ERA5 surface data utilized could possibly explain some parts of the disagreements (bias and uncertainty) observed between $\pi\uparrow L_{CERES,clr}$ and $\pi\uparrow L_{RTM,clr}$.

6.2.3 Transition Zone Radiative Effects

The broadband longwave (5-100 µm) radiative effect on flux (assuming an isotropic distribution for the radiance) for the transition zone footprints (RE_{trz}, W m^{-2}) was calculated as the difference between the radiances measured by CERES ($\uparrow L_{CERES,trz}$) and the corresponding simulated clear-sky values ($\uparrow L_{RTM,clr}$) according to Eq. 6.2:

$$RE_{trz} = \pi \uparrow L_{CERES,trz} - \left(\pi \uparrow L_{RTM,clr} - \bar{\varepsilon}_{clr}\right) \qquad \textit{Eq. 6.2}$$

In this equation, $\bar{\varepsilon}_{clr}$ is included for canceling the systematic bias in the estimation of $\uparrow L_{RTM,clr}$ (see Section 6.2.2). According to the uncertainty assessment described in section 6.2.2, a random error of about $\pm$3.7 W m^{-2} (at 95% confidence level) is associated with the RE_{trz} values calculated this way. Worth mentioning that as in the present study we

have given negative sign to the physically upwelling radiances, a positive and negative RE_{trz} will imply heating and cooling effects, respectively. Also, it should be noted that RE_{trz} values determined this way are indeed RE on radiance, despite they are presented in irradiance units (W m^{-2}) assuming isotropic radiance.

6.3 Results and Discussion

Figure 6.3 shows the probability distribution of the RE_{trz} values obtained from analyzing the 3783 transition zone CERES footprints detected over the South-East Atlantic region during August 2010 based on the criteria and methods explained in section 6.2. In this figure, the left and right axis show the cumulative and absolute empirical probabilities of RE_{trz}, respectively. The box plot given in this figure also summarizes the RE_{trz} values calculated for all transition zone footprints. The bar chart shows the mean frequency of the three MODIS lost classes (A, B and C) in the CERES transition zone footprints analyzed. From this figure it can be seen that "Lost A" is the most frequent class among all the "Lost" classes, followed by "Lost B" and "Lost C", which is in line with the results of Schwarz et al. (2017). The absolute probability of the RE_{trz} values provided in Figure 6.3 shows that for the studied period and domain the RE_{trz} values extend from -4 to 50 W m^{-2} and follow a right-skewed distribution with a mean and median of about 8.0 and 5.4 W m^{-2}, respectively. Among these values, a vast majority (84%) of them are positive. This implies that, as expected, for the vast majority of the transition zone CERES footprints analyzed, the outgoing longwave radiation at TOA was smaller than what it would have been if no suspension was present (as in the present study the upwelling radiances have been indicated with negative signs). In other words, the results show that at most of these footprints, a suspension of particles exists which cannot be classified as cloud or aerosol, but it is clearly interacting with the longwave radiation emitted from the sea surface and causing a reduction in the outgoing longwave radiation at TOA (heating effect). The information provided in Figure 6.3 also shows that for around 60% of the cases analyzed, the magnitude of the interactions of this suspension is indeed greater than that of the uncertainties associated with the methodology adopted ($\pm$3.7 W m^{-2}). These facts prove that the radiative effects shown in Figure 6.3 are not coincidental; contrarily, they must be due to the transition zone particle suspension. They also prove that the transition zone occurs over a vast area which makes it possible to observe its TOA radiative signature in radiative measurements at a spatial resolution as coarse as that of CERES. The heating effects

corresponding to the transition zone footprints with the magnitude of RE_{trz} greater than that of the method uncertainty must be due to the absorption of the longwave radiation emitted from the sea surface by the transition zone particles and the subsequent emission by the same particles at a temperature which is considerably cooler than that of the sea surface.

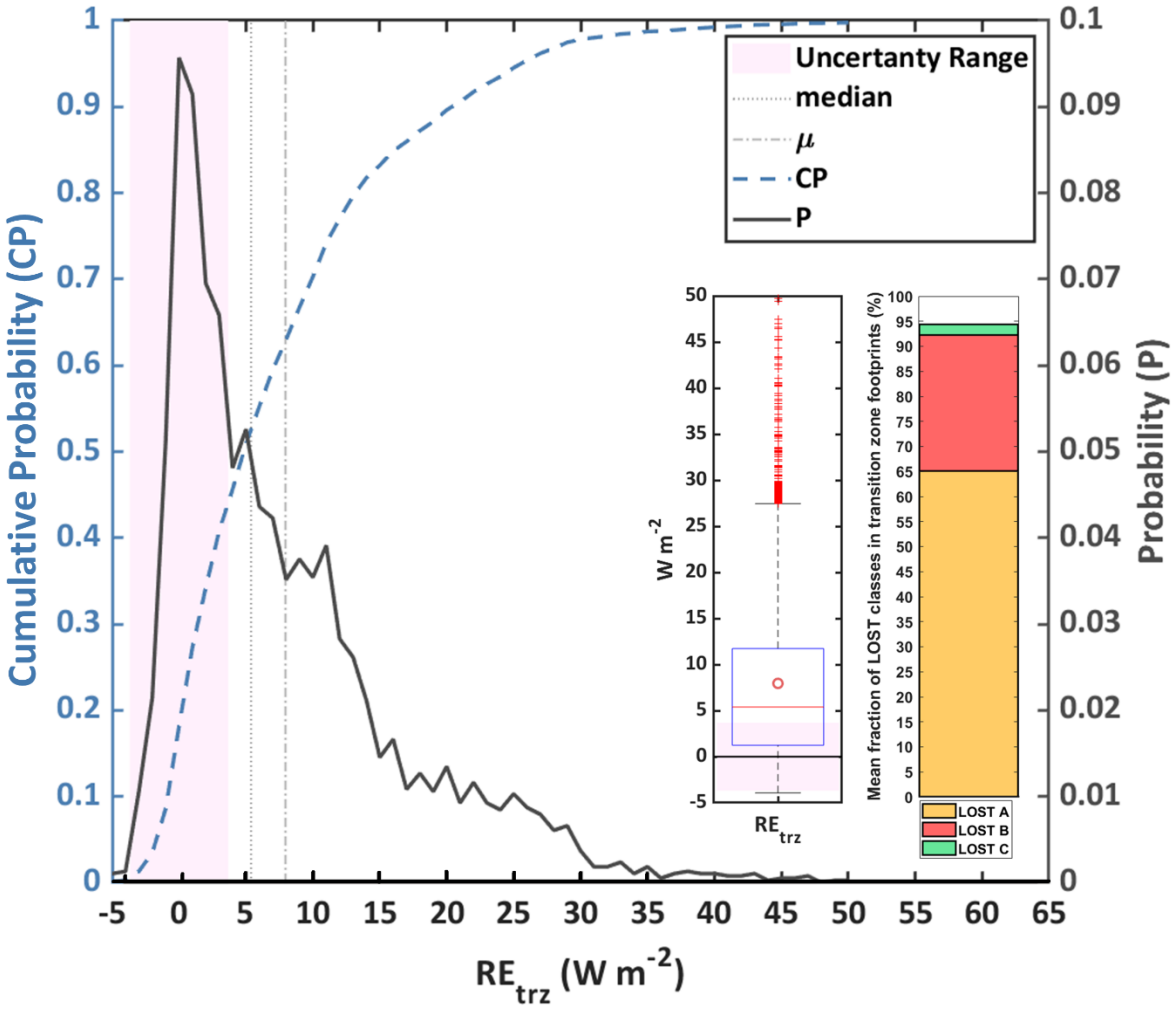

Figure 6.3. Empirical cumulative (left axis) and absolute (right axis) probability distributions of the RE_{trz} calculated for the 3783 transition zone footprints selected in the South-East Atlantic Ocean during August 2010. In this figure, the RE_{trz} bins are 1 W m^{-2} wide and centered at each enter number. The area colored in pink shows the uncertainty range, which was obtained through validating the $\pi\uparrow L_{RTM,clr}$ against $\pi\uparrow L_{CERES,clr}$ (for more information refer to Figure 6.2-a). The box plot and bar chart show dispersion of the RE_{trz} values and mean fraction of the "Lost" classes in the transition zone footprints analyzed, respectively. (note: in this figure, μ stands for mean of RE_{trz}, Source: Jahani et al., 2021)

The fact that the probability distribution of the RE_{trz} values is right-skewed and has a tail extending up to 50 W m^{-2}, also indicates that the REs calculated in the present study are due to particle suspensions between cloud-free and cloudy skies with different micro- and macro-physical characteristics, which is to be expected and is consistent with what is referred to as the transition zone: a phase of particles between the cloudy and so-called cloud-free skies, at

which the characteristics of the suspension lay between those corresponding to the adjacent clouds and the surrounding aerosols (Koren et al., 2007; Várnai et al., 2013). Among all RE_{trz} values illustrated in Figure 6.3, for example, almost 41% of them are within the uncertainty range ($-3.7 \leq RE_{trz} \leq 3.7$ W m^{-2}). These REs, which comprise almost all (98%) negative and 30% of the positive RE_{trz} values, could potentially represent transition zone conditions with characteristics very close to clear-sky condition (relatively low concentration of particles), or those at which the upward emission by transition zone suspension is performed at temperatures close to the sea surface temperature. Whereas the extreme values at the right tail of the distribution (RE_{trz} values greater than 27.6 W m^{-2}, shown with red marks in the boxplot given in Figure 6.3, that is the 3.7% highest values) correspond to transition zone footprints which are contaminated with the edges of optically thick clouds, as the transition zone footprint selection criteria applied in the present study allows up to 10% contribution from other classes (see section 6.2.1).

The difference between the temperatures at which the emission is performed (dT, K), specifically between the sea surface and the top of a parcel of an atmospheric particle suspension, plays a primary role in the longwave RE of this suspension at TOA. It also provides some descriptive information about the characteristics of the particle suspension. To be able to further characterize the transition zone conditions detected within the study area, dT was approximated for each transition zone footprint. In this approximation sea surface temperature was taken equal to the ERA5 reanalysis 2 m air temperature corresponding to the closest ERA5 grid cell linearly interpolated in time according to the time of observation (i.e., the temperature used in the clear-sky simulations). Transition zone suspension top temperature was assumed equal to CERES SSF levels 2 instantaneous cloud top temperature (Minnis et al., 2011). This assumption was made because this parameter is indeed the average of MODIS cloud top temperature retrievals made for the cloudy MODIS pixels (determined by the MODIS cloud mask) falling within CERES FOV. It should be noted that in case of the transition zone footprints, according to the bar chart provided in Figure 6.3, 65% of the MODIS pixels were labeled as “Lost A”, and that for “Lost A” pixels, cloud top temperature was retrieved, as they were initially labeled as cloud by the cloud mask. In other words, for the transition zone footprints, the temperature of the top of the suspension is the result of averaging cloud top temperature retrieved for both the “Lost A” pixels and the potential

cloudy pixels falling within the remaining ≤ 10% of the FOV (see section 6.2.1 for more information).

Figure 6.4 shows the values of RE_{trz} as a function of dT. In this figure, black filled circular markers, yellow crosses and vertical blue lines show the mean and median and standard deviation of the RE_{trz} values corresponding to each dT bin, respectively. The horizontal black lines also indicate the width of each dT bin. The information provided in this figure shows that RE_{trz} is strongly correlated with dT and it increases with dT, which confirms the abovementioned statement regarding the relationship between RE and temperature at which the LW radiation is emitted. From this figure it can also be seen that dT for the transition zone footprints analyzed in the present study varies between -1.5 and 31 K. This implies that the transition zone footprints selected and analyzed in the present study in fact represent transition zone conditions at different altitudes (i.e., dT increases with altitude) and with different characteristics. The transition zone footprints with relatively small dT values (specifically those falling in the first four dT bins shown in Figure 5.4), for example, could potentially represent transition zone conditions near the sea surface with characteristics similar to those of the low clouds. According to Figure 6.4, RE_{trz} corresponding to these latter footprints, which comprise around 85% of the footprints that their RE_{trz} falls within the uncertainty range (see Figure 6.3), is on average about 0.8 W m^{-2}. This number is closely in agreement with what was found by Eytan et al. (2020) as the globally averaged magnitude of RE_{trz} around the warm low cloud fields (~0.75 W m^{-2}), even though the method adopted by them is quite different to what is proposed in the present study. Specifically, in Eytan et al. (2020) distance from the nearest cloud (Koren et al., 2007) was used as a statistical measure for the likelihood of finding twilight conditions and RE_{trz} was calculated based on mean TOA MODIS radiance observations. In contrast, the methodology proposed in the present study is based on instantaneous satellite observations and radiative transfer calculations. Furthermore, the fact that the dT corresponding to the present study transition zone footprints varies between -1.5 and 31 K shows that the methodology proposed in the present study is capable of capturing the radiative signatures of transition zone conditions with a broad range of characteristics at CERES measurement spatial resolution and thus can be applied for studying REs of transition zone conditions with different characteristics.

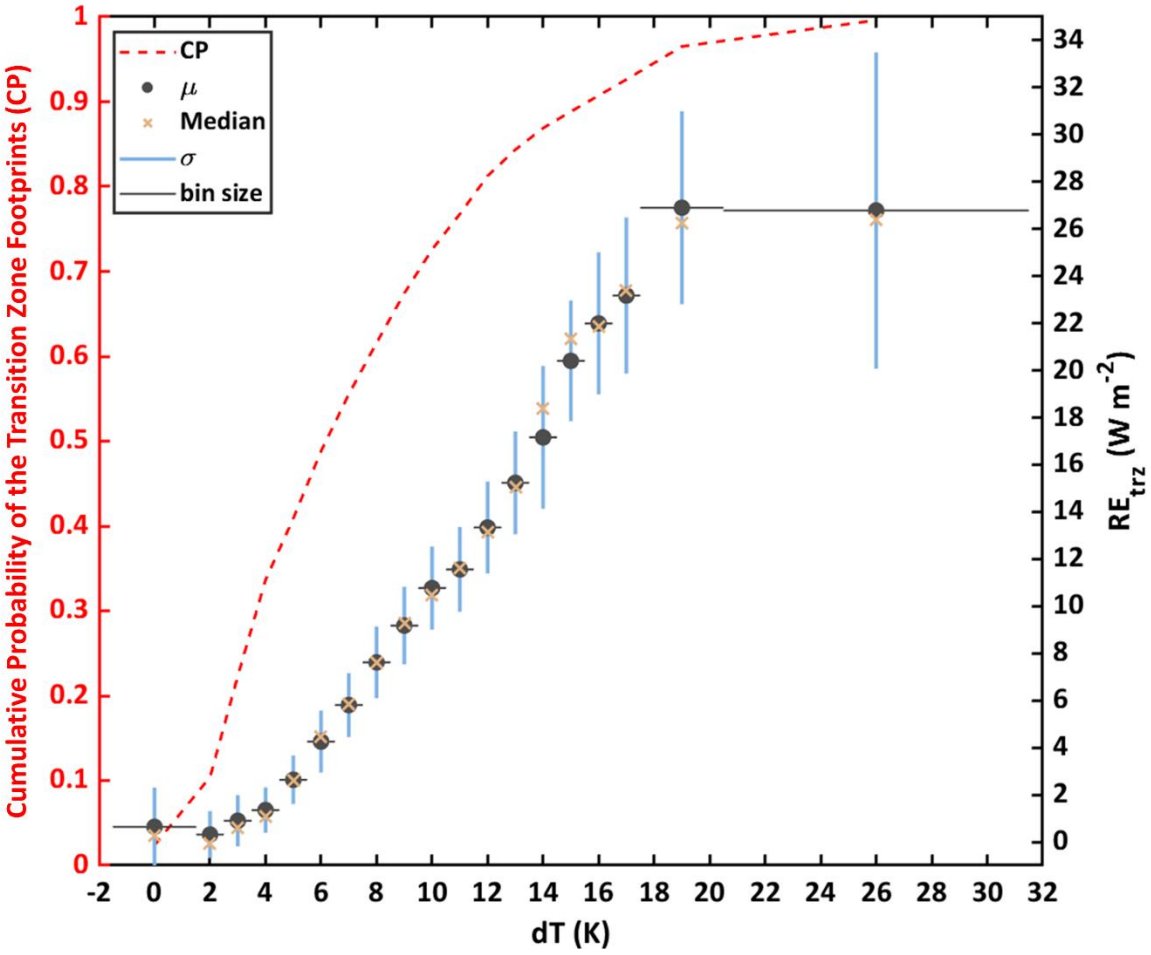

Figure 6.4. Cumulative probability (left axis) and RE_{trz} (right) of the transition zone footprints analyzed as a function of dT. The vertical blue lines, black circles and yellow crosses indicate the standard deviation (σ), mean (μ) and median of the RE_{trz} values in each dT bin, respectively. The horizontal black lines show the width of each dT bin. The r^2 values given in this figure show the determination coefficients between mean (and median) values of RE_{trz} corresponding to the dT bins and dT. (Source: Jahani et al., 2021)

6.4 Summary, Conclusions, and implications for atmospheric research

In the present study, a method for quantification of the broadband longwave radiative effects of the transition zone at TOA (RE_{trz}) during daytime over the ocean based on satellite observations and radiative transfer simulations was proposed. Specifically, RE_{trz} was computed as the difference between the longwave irradiance as measured by CERES (Clouds and the Earth's Radiant Energy System) and the clear-sky irradiance as computed by Santa Barbara DISORT Atmospheric Radiative Transfer (SBDART) model run for the same place and moment, with the input data from ERA5 reanalysis. The identification of the transition zone conditions (CERES footprints) is based on MODIS (Moderate Resolution Imaging Spectroradiometer) products following the Schwarz et al. (2017) method, and 3783 cases

have been found for the analyzed area in the SE Atlantic Ocean for August 2010. The uncertainty of the method for RE estimation was assessed by means of applying the same approach on clear-sky regions. This approach was applied to the data recorded by the CERES and MODIS sensors onboard Aqua platform during August 2010 over the South-East Atlantic Ocean. The results obtained from this analysis can be summarized as follows:

- The transition zone occurs over vast areas which makes it possible to observe its TOA radiative signature in radiative measurements at a spatial resolution as coarse as that of CERES.
- The methodology proposed in the present study is capable of quantifying the radiative effects of transition conditions with a wide range of characteristics with an accuracy of about ± 3.7 W m^{-2} at 95% confidence level, based on instantaneous satellite measurements and radiative transfer simulations.
- For the studied period and domain, RE_{trz} is on average equal to 8.0 W m^{-2} (heating effect; median: 5.4 W m^{-2}), although cases with RE_{trz} with magnitudes as large as 50 W m^{-2} were observed.
- Low-level transition zone conditions (determined based on the difference between the layer top and surface temperature) on average produce a RE of about 0.8 W m^{-2}.

These results and those found by other studies show that the transition zone is indeed an important phase of particle suspensions in the atmosphere with a notable radiative signature in the longwave region, which deserves to be further investigated. The methodology presented in the current study provides the opportunity to gather information about the longwave radiative effects of homogeneous transition zone conditions with different characteristics. This information can be useful for characterizing the transition zone as an additional intermediate phase of particle suspension (class) between cloudy and cloud-free skies (containing aerosols or not) in the remote sensing algorithms, as well as in climatic, meteorological, and atmospheric studies. Nevertheless, this approach only provides information about the longwave radiative effects of the transition zone and the RE_{trz} values given in the present study were obtained by analyzing only one month of data at a particular study area. To be able to understand the role that the transition zone plays in the determination of the Earth's energy budget and the climate system, it is required to study the

transition zone radiative effects in both longwave and shortwave spectral bands over larger domains and longer time spans. These aspects should be the matter of future research efforts.

Chapter 7
Discussions

Summary

In chapters 4 to 6, we have developed different frameworks to enrich the information available about the transition zone radiative effects and their representation in the atmospheric models. The information about the methodologies adopted and the results obtained from each of these individual analyses are provided in the corresponding chapters. Here, we recover the points of topics individually discussed in the previous chapters and further discuss them.

This chapter is divided into two subsections. In the first one we approach the transition zone form a modeling perspective and discuss the uncertainties associated with neglecting the transition zone in the radiative transfer parameterizations included in WRF-ARW. The second subsection involves discussing the experimental efforts that we have made for developing methods for detection of transition zone conditions on the basis of the spaceborne and/or surface radiometers and using them to quantify the transition zone radiative effects.

7.1 Uncertainties Originating from Transition Zone Neglection in Radiative Transfer Simulations

To quantify the uncertainties risen from different approximations to the transition zone in a meteorological/weather-forecasting model (describing a situation corresponding to the transition zone as cloud or as aerosol), we isolated several *swrad* and *lwrad* parameterizations from the model WRF-ARW and adapted them for ideal one-dimensional vertical simulations. These parameterizations which comprise the shortwave and longwave schemes of NGO, RRTMG, FLG parameterizations are different in various senses: they have different definition of shortwave and longwave bands and direct and diffuse irradiances, follow different methodologies for dealing with the radiative transfer in the atmosphere as well as parameterizing cloud optical properties from the input microphysical characteristics. The isolated parameterizations were then utilized to perform several sets of simulations under ideal "cloud" and "aerosol" modes. This was done through adding layers of cloud and aerosol with different characteristics and calculating the REs (i.e. the difference with the irradiances produced by typical clean atmospheres) produced by them based on the irradiances simulated by the parameterizations.

The results obtained from these analyses showed that there are important and distinct differences between the REs of clouds and aerosols simulated by the parameterizations which are more complex and deal with the radiative transfer as well as with the interactions of clouds and aerosols with radiation in more detail ($RRTMG_{sw}$, NGO_{sw}, FLG_{lw}). In other words, clouds and aerosols are well differentiated in these parameterizations and for clouds and aerosols with the same τ and size of particles they simulate different REs. This means that they are sensitive to type (composition) of suspension, as they are also to the effective size and concentration of particles. Thus, when these parameterizations are used, the different treatments of the transition zone (assigning the characteristics of the clouds and aerosols to the transition zone) can introduce large uncertainties to the simulated broadband irradiances in both shortwave and longwave bands. This could influence the dynamics in the meteorological model, as they may cause large differences in the estimated atmospheric shortwave heating and longwave cooling rates. These uncertainties are even very notable at very small optical depths and increase with τ. For example, based on the tested configurations, different treatments of the transition zone can cause up to 27.0 W m^{-2} (7.2 W

m^{-2}) of uncertainty in the simulated downwelling surface shortwave (longwave) irradiances at a very low τ of 0.10 and up to about 400 W m^{-2} (60 W m^{-2}) at the τ of 2.00 (see Figures 4.4 and 5.3 for more information). However, it should be noted that these values correspond to the range of uncertainties (not absolute values) which may arise from different treatments of the transition zone and thus cannot be summed up with each other. Also, as the interest of this thesis lies in analyzing in depth the effects of different treatments of the transition zone on the simulated shortwave and longwave irradiances, we are using slightly different experimental setups in chapters 4 and 5, which makes it rather complicated and maybe incorrect to sum up the results given in these two chapters. An interesting future proposal towards understanding the overall uncertainties associated with different treatments of the transition zone, could be to analyze the differences in the simulated net REs (i.e., the balance between downwelling and upwelling shortwave and longwave fluxes). This could be best addressed through performing simulations using a single RTM capable of treating the transfer of *swrad* and *lwrad* in the atmosphere in full detail (rather than radiation parameterization) in both shortwave and longwave bands.

Also, important to mention that although these uncertainties have been computed from physical modeling and refer only to local and temporary effects, they deserve to receive attention, because according to several studies, at any time a significant proportion of sky is potentially covered with such a particle suspension (Calbó et al., 2017; Fuchs & Cermak, 2015; Schwarz et al., 2017; Wollner et al., 2014). This means that these uncertainties may be introduced to the radiative estimations made over vast areas. One possible proposal for dealing with the transition zone REs for such models is defining an additional intermediate phase between the cloudy and clear skies. This may be done through introducing in models a new set of optical properties for transition zone, based on the observations or an interpolation between the radiative/optical properties of hydrated aerosols and clouds (such as some adjusted size distributions laying between those typical of aerosol and those typical for clouds).

The results presented in chapters 4 and 5 also show that the radiative parameterizations FLG_{sw} and NGO_{lw} simulate rather similar REs for particle suspensions with the same effective sizes at concentrations producing the same optical depths (at 0.550 µm wavelength) regardless of the type (i.e. aerosol, ice cloud, liquid cloud). The reason for this similarity in the

REs simulated for clouds and aerosols with similar effective radius could be due to the assumption adopted for parametrizing the cloud optical properties in these radiative schemes as well as the method utilized for solving the RTE and irradiance simulations. Although these simulations are probably less accurate compared with those made by the more complex parameterizations, they could indeed be useful tools for addressing the transition zone REs through continuous treatment of the particle suspensions (from pure aerosols to fully developed clouds). However, doing so at the cost of simplifying the particle-radiation interactions and loosing accuracy may not be the best favorable option. That is because simplification will decrease the difference between the REs simulated for clouds and aerosols, so apparently reducing the range of uncertainty involved in transition zone cases. This apparent lower uncertainty would be probably due to the decrease in the accuracy of the of the radiative transfer calculations, which is not very convenient, as a lot of efforts have been (and are being) made towards more accurate simulations and measurements. Instead, this can be addressed through development/improvement of Spectral (Bin) Microphysical models/parameterizations (Grabowski & Thomas, 2021; Khain et al., 2015) which can properly determine the evolution of the microphysical and optical properties of the suspensions as they get humidified or dehumidified. The advantage of these models is that they calculate the particle size distribution by solving explicitly the microphysical equations (on several tens to several hundreds of mass bins) rather than assuming a semiempirical size distribution for the hydrometeors. Such models, however, have the disadvantage of being highly computational demanding, and may increase the computation time if used in climate/meteorological models.

The abovementioned two proposals, however, will yet require defining an index (or a set of indices) to discriminate the phase of the particle suspension (aerosol, transition zone, and cloud). To be able to come up with some criteria for performing this discrimination and implication of transition zone optical properties in the models, it is essential to continue studying the radiative behavior of the transition zone particle suspension, as well as exploring the size distribution and the composition of particles in the regions around the clouds based on in situ measurements. That is because the models are eventually designed based on the data obtained from observations.

Another possible practice for dealing with the transition zone REs in atmospheric, meteorological or climate models could be ensemble modeling (Kotu & Deshpande, 2019). In this context, ensemble modeling refers to simulating/predicting the radiative transfer processes in the atmosphere based on sets of simulations performed under different model configurations/setups. For example, running WRF-ARW multiple times for the same domain and time frame but using different microphysical setups and presenting the magnitude of the radiative process at the domain and time of interest as the average of the simulations performed under all model setups may address the REs of the transition zone. That is because what labeled as cloud by one microphysical algorithm may be labeled as cloud-free by another and thus the average of radiative processes simulated under both conditions may represent that of the conditions in between (transition zone).

7.2 Experimental Efforts Towards the Transition Zone Radiative Effects Quantification

The importance of the transition zone and the uncertainties that its neglection can introduce to the estimation of the energy budget encouraged us to further investigate the transition zone and the possibility of detecting transition zone conditions and eventually quantifying its actual REs based on radiative measurements. However, being able to find a set of reference cases which can confidently be labeled as the transition zone was the biggest challenge ahead. This is because in most cases (if not all) the transition zone condition is not visible to the human eye thus we will rely on the radiative measurements or other passive or active observations to figure that out. On the other hand, the information available about the interactions of transition zone particle suspension with radiation is very limited which makes the search for characteristics which could potentially fit the definition provided for the transition zone (Koren et al., 2007) in the radiative measurements quite challenging. That is because the decision about the state of sky in the current cloud screening methods is made based upon on the characteristics expected from visible clouds and the sky labeled as cloud-free is assumed to contain some load of aerosol (Calbó et al., 2017; see section 1.3), making it hard to look for some characteristics between cloud and aerosol. Also, many processes occur in parallel at different levels of the atmosphere while we want to search for radiative signatures corresponding to the transition zone occurring at a specific level of the atmosphere.

To tackle this issue, we came up with a wide range of ideas and tested them one by one and from the experiences learned, we developed newer ideas. For example, we initially tried adjusting/changing the thresholds applied in the cloud-screening algorithms used in MFRSR and Sky-Camera measurements to divide the state of sky into three classes (cloudy, transition zone and clear). But we were not able to decide on the exact thresholds which need to be applied. Then, we came up with other ideas to search for conditions which would match the definition of the transition zone (Koren et al., 2007). For example, we studied the temporal variations in the signal received at water vapor absorptive bands of the MFRSR in comparison with those of the non-absorptive bands and looked for conditions which may represent particle growth and shrink due to water vapor absorption/lose. Most of these efforts, however, failed to detect conditions which could confidently be labeled as the transition zone. This time due to the insufficient sampling frequency, measurement accuracy and also probably due to the fact that what is observed from the surface correspond to many processes occurring in parallel at different levels of the atmosphere.

Eventually, we succeeded developing a method for quantifying the actual TOA broadband longwave REs. This method involves combining multiple products of the CERES and MODIS spaceborne instruments for labeling CERES footprints with homogeneous transition zone conditions and radiative transfer calculations performed using the SBDART model fed by the ERA5 atmospheric profiles and surface data. We tested this approach using the radiative measurements made by the MODIS and CERES instruments onboard Aqua platform over the south-eastern Atlantic Ocean during August 2010. The results obtained from this analysis proved that there exist particle suspensions between cloud-free and cloudy skies with different micro- and macro-physical characteristics, which is to be expected and is consistent with what is referred to as the transition zone. These results also prove that our proposed approach is capable of capturing the radiative signatures of transition zone conditions with a broad range of characteristics present at different altitudes at CERES measurement spatial resolution with an accuracy of ± 3.7 W m^{-2} and thus can be applied for studying REs of transition zone conditions with different characteristics, eventually at a global scale. According to the analysis performed on the basis of this method, we found that for the studied period and domain, transition zone was on average producing RE of about 8.0 W m^{-2} (heating effect), although cases with RE as large as 50 W m^{-2} were found.

We also studied the magnitude of the estimated transition zone REs as a function of the difference between the temperatures at which the emission is performed, specifically between the sea surface and the top of a parcel of an atmospheric particle suspension, which plays a primary role in the longwave RE of this suspension at TOA. From this analysis we found that the temperature differences for the transition zone footprints analyzed in the present study varies between -1.5 and 31 K, which implies that the transition zone footprints selected and analyzed in the present study in fact represent transition zone conditions at different altitudes. We analyzed the magnitude of the transition zone REs corresponding to the transition zone footprints with relatively small differences (they could potentially represent transition zone conditions near the sea surface), and we found that for them the average RE is about 0.8 W m^{-2}. Although we applied our proposed method to a limited domain, this number is closely in agreement with what was found by Eytan et al. (2020) as the globally averaged magnitude of transition zone RE around the warm low cloud fields (~0.75 W m^{-2}). This is interesting because in the latter study (Eytan et al. ,2020) distance from the nearest cloud was used as a measure for the probability of finding transition zone conditions, and the transition zone RE was calculated based on mean TOA MODIS radiance observations which have a spatial resolution of about 1 km at nadir. In contrast, the methodology proposed in this thesis is based on instantaneous coarse scale satellite observations (spatial resolution: 20 km at nadir) and radiative transfer calculations. It is worth mentioning that the areas we refer to as the transition zone are often discarded in the observations, as they cannot be labeled as cloud nor aerosol, thus their REs are not included in the studies quantifying the Earth's energy budget.

Indeed, the success in quantifying the transition zone radiative signature was an important step towards representation of the transition zone in the atmospheric models. That is because it can help testing different ideas proposed for dealing with the transition zone REs in the atmospheric models. In other words, it makes it possible to investigate the accuracy and applicability of different methods proposed for presenting the transition zone in the radiative transfer and atmospheric models. For example, one can compare the observed REs with those simulated under different assumptions towards the transition zone (similar to what illustrated in Figure 5.3) and come up with an empirical approach for addressing the transition zone broadband REs.

Nevertheless, it should be noted that there are some limitations involved with this approach. For example, although we assume that the MODIS pixels classified as “Lost” correspond to the transition zone conditions, we cannot be totally sure that this assumption is true for all of the lost cases analyzed in our study. That is because, there may exist lost pixels with fully developed scattered clouds present at subpixel scale. In addition, the criteria considered in chapter 6 for selection of horizontally homogeneous transition zone footprints allows up to 10% of contamination by other atmospheric suspensions, which has an influence on the estimated RE_{trz} values. In other words, the RE_{trz} values given in Figures 6.3 and 6.4 cloud partly be affected by the REs of cloud edges and those of aerosols present in the subpixel scale. To show the influence of subpixel clouds on the calculated REs, we analyzed the magnitude of RE_{trz} values given in Figure 6.3 as a function of cloud fraction in CERES FOV.

To perform this analysis, we clustered the transition zone CERES footprints based on the calculated cloud fraction into 10 cloud fraction bins ranging between 0 and 10 % (each bin is 1% wide). Then, for each individual cloud fraction bin, we calculated the bootstrap mean. Specifically, we selected 1000 sample groups (population of each group: 50; random sampling with replacement) from each individual cloud fraction bin and calculated the mean RE for sample group. Afterwards, the overall average RE (and the corresponding standard deviation) for each cloud fraction bin was calculated from the sample group means. This procedure is referred to as bootstrapping in statistics (Efron & Tibshirani, 1985) and is a perfect tool for comparing data from groups with unequal sample number. The results of this analysis are presented in Figure 7.1. From the information provided in this figure it can be seen that RE increases with cloud fraction, which confirms the abovementioned statements about the effect of cloud edges and scattered clouds in the subpixels scale on the calculated RE_{trz} values. However, the information provided in this figure also shows that for majority ($\approx$ 71%) of the CERES transition zone footprints that we have analyzed, the cloud fraction is below 4%. This implies that although subpixel clouds have had an influence on our results given in Figure 6.3, their effect on the overall results of the analysis presented in chapter 6 is rather minimal.

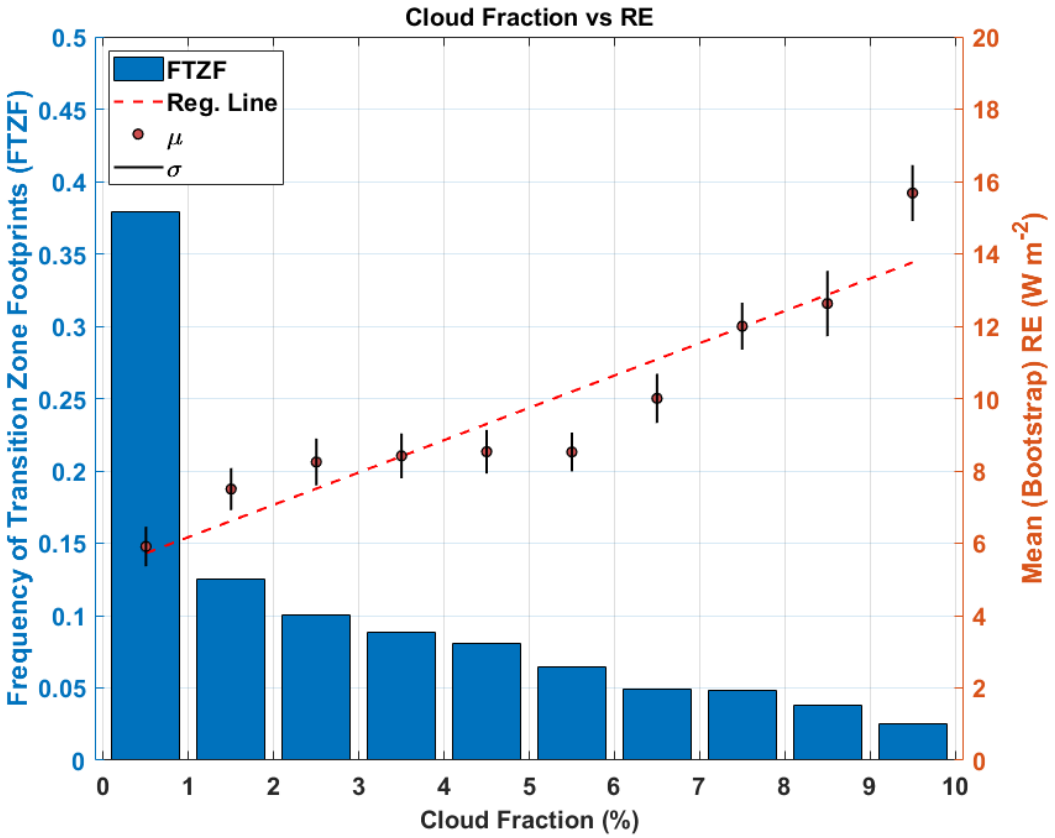

Figure 7.1. RE_{trz} as a function of cloud fraction. Each cloud fraction bin given in this figure is 1% wide and the bar charts indicate the frequency of the transition zone footprints falling within the limits of each cloud fraction bin. The red circles and black vertical lines indicate the (bootstrapped) mean RE_{trz} and the corresponding standard deviation for each cloud fraction bin, respectively. The red dashed line is a linear regression line fitted to (bootstrapped) mean RE_{trz} values.

Another limitation is the fact that this approach only provides information about the longwave REs of the transition zone over the oceans. Whereas to be able to understand the role that the transition zone plays in the determination of the Earth's energy budget and the climate system, it is required to study the transition zone radiative effects in both longwave and shortwave spectral bands over larger domains, covering land and sea and for longer time spans. Despite these limitations, our findings can yet provide the basis for further understanding and characterizing the transition zone particle suspension. For example, the criteria considered in our study for identification of transition zone conditions based on MODIS narrowband radiative measurements can be applied to multi-wavelength narrowband radiometers such as MFRSR. This will help finding sets of transition zone conditions, which could serve as reference conditions for adjusting the criteria considered in the cloud-screening algorithms in a way that it divides the state of sky into three classes (cloudy, transition zone and clear). These aspects, however, are the matter of future research efforts.

Chapter 8
Conclusions

Conclusions

In this thesis we have contributed to the knowledge available about the climate system from an energy budget point of view by showing that the transition zone is indeed an important phase of particle suspension in the atmosphere with a notable radiative signature, which its neglection (assuming it as cloud or aerosol) in models and observations can introduce large uncertainties to the estimates of the Earth's energy budget. In pursuit of this goal, we have been guided by the objectives presented in Section 2.

Specifically, and regarding the first specific objective, we have found that assuming a situation corresponding to the transition zone as optically thin layers of cloud and aerosol by the radiative parameterizations can indeed introduce substantial uncertainties to the radiative processes simulated in both shortwave and longwave bands, which will eventually influence the dynamics in a meteorological model. Specifically, based on the tested configurations, we showed that different treatments of the transition zone can cause up to 27.0 W m^{-2} and 7.2 W m^{-2} of uncertainty in the simulated surface shortwave and longwave irradiances at a very low τ of 0.10, respectively. Also, our results showed that the magnitude of these uncertainties increases with τ and may reach to up to about 400 W m^{-2} and 60 W m^{-2} in shortwave and longwave bands, respectively (for τ = 2.00).

Furthermore, in line with the second objective of this thesis, we came up with a wide range of ideas and tested them one by one and from the experiences learned, we developed newer ideas. Eventually, we succeeded developing a method for quantifying the actual transition zone broadband RE at the TOA based on the instantaneous radiative measurements made by MODIS and CERES spaceborne radiometers over the oceans. This method was tested using the daytime data recorded by MODIS and CERES instruments onboard Aqua spacecraft during August 2010 over South-East Atlantic Ocean. The results obtained from this analysis showed that the proposed method can detect the radiative signatures of a particle suspension between cloud-free and cloudy skies with different micro- and macro-physical characteristics, which matched well the description proved for the transition zone with an accuracy of $\pm$ 3.7 W m^{-2} at 95% confidence level. For the studied period and domain, we found that transition zone was on average producing RE of about 8.0 W m^{-2} (heating effect), although cases with RE as large as 50 W m^{-2} were found. It is worth mentioning that the areas we refer to as the

transition zone are often discarded in the observations, as they cannot be labeled as cloud nor aerosol, thus their REs are not included in the studies focusing on the Earth's energy budget.

Other important conclusions of this thesis also include:

- Different radiative parameterizations solve the RTE in the atmosphere with different levels of complexity and because of that, they show various degrees of sensitivity to different treatments of the transition zone. Specifically, there exist important and distinct differences between the REs of cloud and aerosol layers with the same effective size and optical depth simulated by parameterizations that deal with the RTE in more detail. Thus, assigning the characteristics of optically thin clouds and aerosols to the transition zone can introduce large uncertainties to the estimated REs. Whereas some others simulate rather similar REs for particle suspensions with the same effective sizes and concentrations regardless of the type (i.e. aerosol, ice cloud, liquid cloud).
- The transition zone occurs over vast areas which makes it possible to observe its TOA radiative signature in radiative measurements at a spatial resolution as coarse as that of CERES. This fact again show that the transition zone is indeed an important phase of particle suspensions in the atmosphere with a notable radiative signature.

Furthermore, the substantial uncertainties associated with neglecting the transition zone and the magnitude of the transition zone REs found over large areas encourage further investigation of the transition zone from different aspects:

- Studying transition zone radiative effects in both longwave and shortwave spectral bands over larger domains and longer time spans to better understand the role that the transition zone plays in the determination of the Earth's energy budget.
- Characterizing the transition zone based on the radiative measurements made by other spaceborne, in situ or surface radiometers.
- Presenting the transition zone REs in atmospheric/meteorological/climate models. Our proposals for presenting the REs of the transition zone in atmospheric models include:

  a) Treating clouds and aerosols as continuum fields in radiative parameterizations/models and observations. Such treatment of clouds and aerosols

particles would rely on modification/development of bin microphysical models/parameterizations capable of continuous modeling of the suspension's optical properties (from pure, dry aerosols to typical clouds).

b) Defining an additional intermediate phase between the cloudy and clear skies and implementing it in in the remote sensing algorithms, as well as in climatic, meteorological, and atmospheric studies. This can be done through gathering information about the microphysical characteristics of the transition zone and its radiative signature in interaction with radiation from the observations. But, doing so would highly rely on being able to find a set of reference cases which can confidently be labeled as the transition zone.
c) Running the meteorological model under different microphysical configurations and presenting the overall magnitude of the radiative process as the average of all individual simulations (ensemble modeling).

To sum up, we believe that the transition (or twilight) zone is an important phase of particle suspension in the atmosphere which its radiative and microphysical characteristics need to be further investigated. We do also think that all kinds of approaches, from observational studies using different platforms to modeling efforts (with both relatively simple parameterizations to full radiative transfer models) may be necessary to reach a general picture about the transition zone and its contribution to the Earth's radiation balance and the weather system.

References

Abdul-Razzak, H., & Ghan, S. J. (2002). A parameterization of aerosol activation 3. Sectional representation. *Journal of Geophysical Research Atmospheres*, *107*(3), 1–6. https://doi.org/10.1029/2001jd000483

Ackerman, S., Richard, F., Kathleen, S., Yinghui, L., Chris, M., Liam, G., et al. (2010). Discriminating clear-sky from cloud with MODIS algorithm theoretical basis document (MOD35). *University of Wisconsin - Madison*, (October), 129. Retrieved from http://citeseerx.ist.psu.edu/viewdoc/summary?doi=10.1.1.385.4885

Ackerman, S. A., & Frey, R. (2015). MODIS Atmosphere L2 Cloud Mask Product (35_L2). *NASA MODIS Adaptive Processing System, Goddard Space Flight Center*. https://doi.org/http://dx.doi.org/10.5067/MODIS/MYD35_L2.006

Ahrens, C. D. (2009). *Meteorology Today: an introduction to weather, climate, and the environment* (9th ed.). Brooks Cole Cengage Learning.

Anderson, G. P., Clough, S. A., Kneizys, F. X., Chetwynd, J. H., & Shettle, E. P. (1986). *AFGL atmospheric constituent profiles (0 - 120km)*. *Air Force Geophysics Laboratory, Hanscom AFB, MA 01731*.

Baek, S. (2017). A revised radiation package of G-packed McICA and two-stream approximation: Performance evaluation in a global weather forecasting model. *Journal of Advances in Modeling Earth Systems*, *9*, 1628–1640. https://doi.org/10.1002/2017MS000994.

Bar-Or, R. Z., Altaratz, O., & Koren, I. (2011). Global analysis of cloud field coverage and radiative properties, using morphological methods and MODIS observations. *Atmospheric Chemistry and Physics*, *11*(1), 191–200. https://doi.org/10.5194/acp-11-191-2011

Blossey, P. N., Bretherton, C. S., Zhang, M., Cheng, A., Endo, S., Heus, T., et al. (2013). Marine low cloud sensitivity to an idealized climate change: The CGILS les intercomparison. *Journal of Advances in Modeling Earth Systems*, *5*(2), 234–258. https://doi.org/10.1002/jame.20025

Bohren, C. F., & Huffman, D. R. (1998). *Absorption and Scattering of Light by Small Particles*. *Absorption and Scattering of Light by Small Particles*.

https://doi.org/10.1002/9783527618156

Boucher, O., Randall, D., Artaxo, P., Bretherton, C., Feingold, G., Forster, P., et al. (2013). Clouds and aerosols. *Climate Change 2013 the Physical Science Basis: Working Group I Contribution to the Fifth Assessment Report of the Intergovernmental Panel on Climate Change*, *9781107057*, 571–658. https://doi.org/10.1017/CBO9781107415324.016

Calbó, J., & Sabburg, J. (2008). Feature extraction from Whole-sky ground-based images for cloud-type recognition. *Journal of Atmospheric and Oceanic Technology*, *25*(1), 3–14. https://doi.org/10.1175/2007JTECHA959.1

Calbó, J., Long, C. N., González, J. A., Augustine, J., & McComiskey, A. (2017). The thin border between cloud and aerosol: Sensitivity of several ground based observation techniques. *Atmospheric Research*, *196*(May), 248–260. https://doi.org/10.1016/j.atmosres.2017.06.010

Carslaw, K. S., Lee, L. A., Reddington, C. L., Pringle, K. J., Rap, A., Forster, P. M., et al. (2013). Large contribution of natural aerosols to uncertainty in indirect forcing. *Nature*, *503*(7474), 67–71. https://doi.org/10.1038/nature12674

Charlson, R. J., Ackerman, A. S., Bender, F. A. M., Anderson, T. L., & Liu, Z. (2007). On the climate forcing consequences of the albedo continuum between cloudy and clear air. *Tellus, Series B: Chemical and Physical Meteorology*, *59*(4), 715–727. https://doi.org/10.1111/j.1600-0889.2007.00297.x

Chen, M., Rood, R. B., & Takacs, L. L. (1997). Impact of a semi-Lagrangian and an Eulerian dynamical core on climate simulations. *Journal of Climate*, *10*(9), 2374–2389. https://doi.org/10.1175/1520-0442(1997)010<2374:IOASLA>2.0.CO;2

Chou, M.-D., & Suarez, M. J. (1999). *A Solar Radiation Parameterization (CLIRAD-SW) for Atmospheric Studies*. *National Aeronautics and Space Administration, Goddard Space Flight Center, Laboratory for Atmospheres, Climate and Radiation Branch*. Retrieved from http://www2.mmm.ucar.edu/wrf/users/phys_refs/SW_LW/Goddard_part1.pdf

Clough, S. A., & Iacono, M. J. (1995). Line-by-line calculation of atmospheric fluxes and cooling rates 2. Application to carbon dioxide, ozone, methane, nitrous oxide and the halocarbons. *Journal of Geophysical Research*, *100*(D8), 16519–16535.

https://doi.org/10.1029/95jd01386

Collins, W. D., Bitz, C. M., Blackmon, M. L., Bonan, G. B., Bretherton, C. S., Carton, J. A., et al. (2006). The community climate system model version 3 (CCSM3). *Journal of Climate*, *19*(11), 2122–2143. https://doi.org/10.1175/JCLI3761.1

Dudhia, J. (1989). Numerical Study of Convection Observed during the Winter Monsoon Experiment Using a Mesoscale Two-Dimensional Model. *Journal of the Atmospheric Sciences*, *46*(20), 3077–3107. https://doi.org/10.1175/1520-0469(1989)046<3077:NSOCOD>2.0.CO;2

Dürr, B., & Philipona, R. (2004). Automatic cloud amount detection by surface longwave downward radiation measurements. *Journal of Geophysical Research: Atmospheres*, *109*(5), 1–9. https://doi.org/10.1029/2003jd004182

Efron, B., & Tibshirani, R. (1985). The Bootstrap Method for Assessing Statistical Accuracy. *Behaviormetrika*, *12*(17), 1–35. https://doi.org/10.2333/bhmk.12.17_1

Eytan, E., Koren, I., Altaratz, O., Kostinski, A. B., & Ronen, A. (2020). Longwave radiative effect of the cloud twilight zone. *Nature Geoscience*, *13*(10), 669–673. https://doi.org/10.1038/s41561-020-0636-8

Fan, J., Wang, Y., Rosenfeld, D., & Liu, X. (2016). Review of Aerosol–Cloud Interactions: Mechanisms, Significance, and Challenges. *Journal of the Atmospheric Sciences*, *73*(11), 4221–4252. https://doi.org/10.1175/JAS-D-16-0037.1

Fels, S. B., & Schwarzkopf, M. D. (1981). An efficient, accurate algorithm for calculating CO 2 15 μm band cooling rates. *Journal of Geophysical Research*, *86*(C2), 1205–1232. https://doi.org/10.1029/JC086iC02p01205

Frey, R. A., Ackerman, S. A., Liu, Y., Strabala, K. I., Zhang, H., Key, J. R., & Wang, X. (2008). Cloud detection with MODIS. Part I: Improvements in the MODIS cloud mask for Collection 5. *Journal of Atmospheric and Oceanic Technology*, *25*(7), 1057–1072. https://doi.org/10.1175/2008JTECHA1052.1

Fu, Q. (1996). An Accurate Parameterization of the Solar Radiative Properties of Cirrus Clouds for Climate Models. *Journal of Climate*, *9*, 2058–2082.

Fuchs, J., & Cermak, J. (2015). Where Aerosols become clouds-potential for global analysis based on CALIPSO data. *Remote Sensing*, *7*(4), 4178–4190. https://doi.org/10.3390/rs70404178

Geier, E. B., Green, R. N., Kratz, D. P., Minnis, P., Miller, W. F., Nolan, S. K., & Franklin, C. B. (2003). *CERES data management system: Single Satellite Footprint TOA/surface fluxes and clouds (SSF) collection document, release 2, version 1*. *NASA Langley Research Center, Climate Science Branch Science, Science Directorate, 21 Langley Boulevard, Hampton*.

González, J. A., Calbó, J., & Sanchez-Romero, A. (2017). Measuring fast optical depth variations in cloud edges with a CCD-array spectrometer. *AIP Conference Proceedings*, *1810*. https://doi.org/10.1063/1.4975534

Grabowski, W. W., & Thomas, L. (2021). Cloud droplet diffusional growth in homogeneous isotropic turbulence: Bin microphysics versus Lagrangian super-droplet simulations. *Atmospheric Chemistry and Physics*, *21*(5), 4059–4077. https://doi.org/10.5194/acp-21-4059-2021

Gu, Y., Liou, K. N., Ou, S. C., & Fovell, R. (2011). Cirrus cloud simulations using WRF with improved radiation parameterization and increased vertical resolution. *Journal of Geophysical Research Atmospheres*, *116*(6), 1–14. https://doi.org/10.1029/2010JD014574

Ha, S., Snyder, C., Skamarock, W. C., Anderson, J., & Collins, N. (2017). Ensemble Kalman filter data assimilation for the Model for Prediction Across Scales (MPAS). *Monthly Weather Review*, *145*(11), 4673–4692. https://doi.org/10.1175/MWR-D-17-0145.1

Harrison, L., & Michalsky, J. (1994). Objective algorithms for the retrieval of optical depths from ground-based measurements. *Appl. Opt.*, *33*, 5126–5132.

Hersbach, H., Bell, B., Berrisford, P., Biavati, G., Horányi, A., Muñoz Sabater, J., et al. (2018a). ERA5 hourly data on pressure levels from 1979 to present. https://doi.org/10.24381/cds.bd0915c6

Hersbach, H., Bell, B., Berrisford, P., Biavati, G., Horányi, A., Muñoz Sabater, J., et al. (2018b). ERA5 hourly data on single levels from 1979 to present.

https://doi.org/10.24381/cds.adbb2d47

Hess, M., Koepke, P., & Schult, I. (1998). Optical properties of aerosols and clouds. *Bulletin of the American Meteorological Society*, *79*(5), 831–844. https://doi.org/10.1175/1520-0477(1998)079<0831:OPOAAC>2.0.CO;2

Houghton, H. G. (1985). *Physical Meteorology*. MIT Press.

Hu, Y. X., & Stamnes, K. (1993). An accurate parameterization of the radiative properties of water clouds suitable for use in climate models. *Journal of Climate*, *6*(4), 728–742. https://doi.org/10.1175/1520-0442(1993)006<0728:AAPOTR>2.0.CO;2

Huang, Y., & Wang, Y. (2019). How does radiation code accuracy matter? *Journal of Geophysical Research: Atmospheres*, *124*(20), 10742–10752. https://doi.org/10.1029/2019jd030296

Iacono, M. J., Delamere, J. S., Mlawer, E. J., Shephard, M. W., Clough, S. A., & Collins, W. D. (2008). Radiative forcing by long-lived greenhouse gases: Calculations with the AER radiative transfer models. *Journal of Geophysical Research Atmospheres*, *113*(13), 2–9. https://doi.org/10.1029/2008JD009944

Jahani, B., Calbó, J., & González, J. A. (2019). Transition Zone Radiative Effects in Shortwave Radiation Parameterizations: Case of Weather Research and Forecasting Model. *Journal of Geophysical Research: Atmospheres*, *124*(23), 13091–13104. https://doi.org/10.1029/2019JD031064

Jahani, B., Calbó, J., & González, J. A. (2020). Quantifying Transition Zone Radiative Effects in Longwave Radiation Parameterizations. *Geophysical Research Letters*, *47*(22), e2020GL090408. https://doi.org/https://doi.org/10.1029/2020GL090408

Jahani, B., Andersen, H., Calbó, J., González, J. A., & Cermak, J. (2021). Longwave Radiative Effect of the Cloud-Aerosol Transition Zone Based on CERES Observations. *Atmospheric Chemistry and Physics Discussions*. https://doi.org/10.5194/acp-2021-421

Jimenez, P. A., Hacker, J. P., Dudhia, J., Haupt, S. E., Ruiz-Arias, J. A., Gueymard, C. A., et al. (2016). WRF-SOLAR: Description and clear-sky assessment of an augmented NWP model for solar power prediction. *Bulletin of the American Meteorological Society*, *97*(7), 1249–

1264. https://doi.org/10.1175/BAMS-D-14-00279.1

Joseph, J. H., Wiscombe, W. J., & Weinman, J. A. (1976). The Delta-Eddington Approximation for Radiative Flux Transfer. *Journal of the Atmospheric Sciences*, *33*(12), 2452–2459. https://doi.org/10.1175/1520-0469(1976)033<2452:tdeafr>2.0.co;2

Kanji, Z. A., Ladino, L. A., Wex, H., Boose, Y., Burkert-Kohn, M., Cziczo, D. J., & Krämer, M. (2017). Overview of Ice Nucleating Particles. *Meteorological Monographs*, *58*, 1.1-1.33. https://doi.org/10.1175/amsmonographs-d-16-0006.1

Kazantzidis, A., Tzoumanikas, P., Bais, A. F., Fotopoulos, S., & Economou, G. (2012). Cloud detection and classification with the use of whole-sky ground-based images. *Atmospheric Research*, *113*, 80–88. https://doi.org/10.1016/j.atmosres.2012.05.005

Khain, A. P., Beheng, K. D., Heymsfield, A., Korolev, A., Krichak, S. O., Levin, Z., et al. (2015). Representation of microphysical processes in cloud-resolving models: Spectral (bin) microphysics versus bulk parameterization. *Reviews of Geophysics*, *53*, 247–322. https://doi.org/10.1002/2014RG000468

Koren, I., Remer, L. A., Kaufman, Y. J., Rudich, Y., & Martins, J. V. (2007). On the twilight zone between clouds and aerosols. *Geophysical Research Letters*, *34*(8), 1–5. https://doi.org/10.1029/2007GL029253

Koren, I., Feingold, G., Jiang, H., & Altaratz, O. (2009). Aerosol effects on the inter-cloud region of a small cumulus cloud field. *Geophysical Research Letters*, *36*(14), 1–5. https://doi.org/10.1029/2009GL037424

Kotu, V., & Deshpande, B. (2019). Chapter 2 - Data Science Process. In V. Kotu & B. Deshpande (Eds.), *Data Science* (Second Edi, pp. 19–37). Morgan Kaufmann. https://doi.org/https://doi.org/10.1016/B978-0-12-814761-0.00002-2

Levy, R., Hsu, C., Sayer, A., Mattoo, S., & Lee, J. (2015). MODIS Atmosphere L2 Aerosol Product. *NASA MODIS Adaptive Processing System, Goddard Space Flight Center*.

Lin, W., Liu, Y., Vogelmann, A. M., Fridlind, A., Endo, S., Song, H., et al. (2015). RACORO continental boundary layer cloud investigations: 3. separation of parameterization biases single-column model CAM5 simulations of shallow cumulus. *Journal of*

Geophysical Research, *120*(12), 6015–6033. https://doi.org/10.1002/2014JD022524

Liou, K.-N. (1980). *An Introduction to Atmospheric Radiation*. London: Academic Press.

Liou, K.-N., Fu, Q., & Ackerman, T. P. (1988). A Simple Formulation of the Delta-Four-Stream Approximation for Radiative Transfer Parameterizations. *Journal of Atmospheric Sciences*, *45*(13), 1940–1947.

Liu, Z., Vaughan, M., Winker, D., Kittaka, C., Getzewich, B., Kuehn, R., et al. (2009). The CALIPSO lidar cloud and aerosol discrimination: Version 2 algorithm and initial assessment of performance. *Journal of Atmospheric and Oceanic Technology*, *26*(7), 1198–1213. https://doi.org/10.1175/2009JTECHA1229.1

Loeb, N. G., Priestley, K. J., Kratz, D. P., Geier, E. B., Green, R. N., Wielicki, B. A., et al. (2001). Determination of unfiltered radiances from the clouds and the earth's radiant energy system instrument. *Journal of Applied Meteorology*, *40*(4), 822–835. https://doi.org/10.1175/1520-0450(2001)040<0822:DOURFT>2.0.CO;2

Loeb, N. G., Sun, W., Miller, W. F., Loukachine, K., & Davies, R. (2006). Fusion of CERES, MISR, and MODIS measurements for top-of atmosphere radiative flux validation. *Journal of Geophysical Research Atmospheres*, *111*(18), 1–11. https://doi.org/10.1029/2006JD007146

Loeb, N. G., Su, W., Doelling, D. R., Wong, T., Minnis, P., Thomas, S., & Miller, W. F. (2018). 5.03 - Earth's top-of-atmosphere radiation budget. In *Comprehensive Remote Sensing* (Vol. 5, pp. 67–84). https://doi.org/https://doi.org/10.1016/B978-0-12-409548-9.10367-7

Loeb, N. G., Yang, P., Rose, F. G., Hong, G., Sun-Mack, S., Minnis, P., et al. (2018). Impact of ice cloud microphysics on satellite cloud retrievals and broadband flux radiative transfer model calculations. *Journal of Climate*, *31*(5), 1851–1864. https://doi.org/10.1175/JCLI-D-17-0426.1

Long, C. N., & Ackerman, T. P. (2000). Identification of clear skies from broadband pyranometer measurements and calculation of downwelling shortwave cloud effects. *Journal of Geophysical Research Atmospheres*, *105*(D12), 15609–15626. https://doi.org/10.1029/2000JD900077

Long, C. N., Sabburg, J. M., Calbó, J., & Pagès, D. (2006). Retrieving cloud characteristics from ground-based daytime color all-sky images. *Journal of Atmospheric and Oceanic Technology*, *23*(5), 633–652. https://doi.org/10.1175/JTECH1875.1

Luke, E. P., Kollias, P., & Shupe, M. D. (2010). Detection of supercooled liquid in mixed-phase clouds using radar Doppler spectra. *Journal of Geophysical Research Atmospheres*, *115*(19), 1–14. https://doi.org/10.1029/2009JD012884

Marchand, R., Mace, G. G., Ackerman, T., & Stephens, G. (2008). Hydrometeor detection using Cloudsat - An earth-orbiting 94-GHz cloud radar. *Journal of Atmospheric and Oceanic Technology*, *25*(4), 519–533. https://doi.org/10.1175/2007JTECHA1006.1

Martucci, G., Milroy, C., & O'Dowd, C. D. (2010). Detection of cloud-base height using Jenoptik CHM15K and Vaisala CL31 ceilometers. *Journal of Atmospheric and Oceanic Technology*, *27*(2), 305–318. https://doi.org/10.1175/2009JTECHA1326.1

Mateos, D., Sanchez-Lorenzo, A., Antón, M., Cachorro, V. E., Calbó, J., Costa, M. J., et al. (2014). Quantifying the respective roles of aerosols and clouds in the strong brightening since the early 2000s over the Iberian Peninsula. *Journal of Geophysical Research*, *119*(17), 10,382-10,393. https://doi.org/10.1002/2014JD022076

Menang, K. P. (2018). Assessment of the Impact of Solar Spectral Irradiance on Near-Infrared Clear-Sky Atmospheric Absorption and Heating Rates. *Journal of Geophysical Research: Atmospheres*, *123*(12), 6460–6468. https://doi.org/10.1029/2018JD028342

Michalsky, J., Denn, F., Flynn, C., Hodges, G., Kiedron, P., Koontz, A., et al. (2010). Climatology of aerosol optical depth in north-central Oklahoma: 1992–2008. *Journal of Geophysical Research*, *115*(D7), D07203. https://doi.org/10.1029/2009JD012197

Ming, Y., & Held, I. M. (2018). Modeling water vapor and clouds as passive tracers in an idealized GCM. *Journal of Climate*, *31*(2), 775–786. https://doi.org/10.1175/JCLI-D-16-0812.1

Minnis, P., Sun-Mack, S., Chen, Y., Khaiyer, M. M., Yi, Y., Ayers, J. K., et al. (2011). CERES edition-2 cloud property retrievals using TRMM VIRS and Terra and Aqua MODIS data-Part II: Examples of average results and comparisons with other data. *IEEE Transactions on Geoscience and Remote Sensing*, *49*(11 PART 2), 4401–4430.

https://doi.org/10.1109/TGRS.2011.2144602

Mishra, A. K., Koren, I., & Rudich, Y. (2015). Effect of aerosol vertical distribution on aerosol-radiation interaction: A theoretical prospect. *Heliyon*, *1*(2), E00036. https://doi.org/10.1016/j.heliyon.2015.e00036

Mitchell, D. L., & Finnegan, W. (2009). Modification of cirrus clouds to reduce global warming. *Environmental Research Letters*, *4*(4). https://doi.org/10.1088/1748-9326/4/4/045102

MODIS Characterization Support Team (MCST). (2017). MODIS Geolocation Fields Product. NASA MODIS Adaptive Processing System, Goddard Space Flight Center, USA. https://doi.org/http://dx.doi.org/10.5067/MODIS/MYD03.061

Moeng, C.-H., Dudhia, J., Klemp, J., & Sullivan, P. (2007). Examining Two-Way Grid Nesting for Large Eddy Simulation of the PBL Using the WRF Model. *Monthly Weather Review*, *135*(6), 2295–2311. https://doi.org/10.1175/MWR3406.1

Montornes, A., Codina, B., Zack, J. W., & Sola, Y. (2016). Implementation of Bessel's method for solar eclipses prediction in the WRF-ARW model. *Atmospheric Chemistry and Physics*, *16*(9), 5949–5967. https://doi.org/10.5194/acp-16-5949-2016

Montornès, A. (2017). *A study of the shortwave schemes in the Weather Research and Forecasting model A study of the shortwave schemes in the Weather Research and Forecasting model*. Retrieved from http://diposit.ub.edu/dspace/handle/2445/108519?mode=full

Montornès, A., Codina, B., & Zack, J. W. (2015). Analysis of the ozone profile specifications in the WRF-ARW model and their impact on the simulation of direct solar radiation. *Atmospheric Chemistry and Physics*, *15*(5), 2693–2707. https://doi.org/10.5194/acp-15-2693-2015

Myhre, G., Shindell, D., Bréon, F.-M., Collins, W., Fuglestvedt, J., Huang, J., et al. (2013). Climate change 2013: the physical science basis. Contribution of Working Group I to the Fifth Assessment Report of the Intergovernmental Panel on Climate Change. In *K., Tignor, M., Allen, SK, Boschung, J., Nauels, A., Xia, Y., Bex, V., and Midgley, PM, Cambridge University Press Cambridge, United Kingdom and New York, NY, USA*.

Petty, G. W. (1958). *A First Course on Atmospheric Radiation*. *Sundog Publishing* (2nd ed.). Madison, Wisconsin: Sundog Publishing. https://doi.org/10.1029/2004eo360007

Platnick, S., King, M. D., Ackerman, S. A., Menzel, W. P., Baum, B. A., Riédi, J. C., & Frey, R. A. (2003). The MODIS cloud products: Algorithms and examples from terra. *IEEE Transactions on Geoscience and Remote Sensing*, *41*(2 PART 1), 459–472. https://doi.org/10.1109/TGRS.2002.808301

Platnick, S., Ackerman, A. S., King, M. D., Meyer, K., W.P., M., Holz, R. E., et al. (2015). MODIS atmosphere L2 cloud product (06_L2). *NASA MODIS Adaptive Processing System*.

Powers, J. G., Klemp, J. B., Skamarock, W. C., Davis, C. A., Dudhia, J., Gill, D. O., et al. (2017). The weather research and forecasting model: Overview, system efforts, and future directions. *Bulletin of the American Meteorological Society*, *98*(8), 1717–1737. https://doi.org/10.1175/BAMS-D-15-00308.1

Priestley, K. J., Smith, G. L., Thomas, S., Cooper, D., Lee, R. B., Walikainen, D., et al. (2011). Radiometric performance of the CERES earth radiation budget climate record sensors on the EOS Aqua and Terra spacecraft through April 2007. *Journal of Atmospheric and Oceanic Technology*, *28*(1), 3–21. https://doi.org/10.1175/2010JTECHA1521.1

Redemann, J., Zhang, Q., Russell, P. B., Livingston, J. M., & Remer, L. A. (2009). Case studies of aerosol remote sensing in the vicinity of clouds. *Journal of Geophysical Research Atmospheres*, *114*(6), 1–9. https://doi.org/10.1029/2008JD010774

Rejano, F., Titos, G., Casquero-Vera, J. A., Lyamani, H., Andrews, E., Sheridan, P., et al. (2021). Activation properties of aerosol particles as cloud condensation nuclei at urban and high-altitude remote sites in southern Europe. *Science of the Total Environment*, *762*(xxxx), 143100. https://doi.org/10.1016/j.scitotenv.2020.143100

Ricchiazzi, P., Yang, S., Gautier, C., & Sowle, D. (1998). SBDART: A Research and Teaching Software Tool for Plane-Parallel Radiative Transfer in the Earth's Atmosphere. *Bulletin of the American Meteorological Society*, *79*(10), 2101–2114. https://doi.org/10.1175/1520-0477(1998)079<2101:SARATS>2.0.CO;2

Rosenfeld, D., Andreae, M. O., Asmi, A., Chin, M., Leeuw, G. de, Donovan, D. P., et al. (2014). Global observations of aerosol-cloud-precipitation- climate interactions. *Reviews of*

Geophysics REVIEW, *52*, 750–808. https://doi.org/10.1002/2013RG000441

Ruiz-Arias, J. A., Dudhia, J., Santos-Alamillos, F. J., & Pozo-Vázquez, D. (2013). Surface clear-sky shortwave radiative closure intercomparisons in the Weather Research and Forecasting model. *Journal of Geophysical Research Atmospheres*, *118*(17), 9901–9913. https://doi.org/10.1002/jgrd.50778

Schwarz, K., Cermak, J., Fuchs, J., & Andersen, H. (2017). Mapping the twilight zone-What we are missing between clouds and aerosols. *Remote Sensing*, *9*(6), 1–10. https://doi.org/10.3390/rs9060577

Seinfeld, J. H., Bretherton, C., Carslaw, K. S., Coe, H., DeMott, P. J., Dunlea, E. J., et al. (2016). Improving our fundamental understanding of the role of aerosol-cloud interactions in the climate system. *Proceedings of the National Academy of Sciences of the United States of America*, *113*(21), 5781–5790. https://doi.org/10.1073/pnas.1514043113

Skamarock, W. C., Klemp, J. B., Dudhi, J., Gill, D. O., Barker, D. M., Duda, M. G., et al. (2008). A Description of the Advanced Research WRF Version 3. *Technical Report*, (June), 113. https://doi.org/10.5065/D6DZ069T

Slingo, A. (1989). A GCM Parameterization for Shortwave Radiative Properties of Water Clouds. *Journal of the Atmospheric Sciences*, *46*(10), 1419–1427.

Slingo, A., & Schrecker, H. M. (1982). On the shortwave radiative properties of stratiform water clouds. *Quarterly Journal of the Royal Meteorological Society*, *108*(456), 407–426. https://doi.org/10.1002/qj.49710845607

Spencer, R. S., Levy, R. C., Remer, L. A., Mattoo, S., Arnold, G. T., Hlavka, D. L., et al. (2019). Exploring Aerosols Near Clouds With High-Spatial-Resolution Aircraft Remote Sensing During SEAC 4 RS. *Journal of Geophysical Research: Atmospheres*, *124*(4), 2148–2173. https://doi.org/10.1029/2018JD028989

Spiridonov, V., & Ćurić, M. (2021). Atmospheric Stability. In *Fundamentals of Meteorology*. https://doi.org/https://doi.org/10.1007/978-3-030-52655-9_9

Tao, W. K., Anderson, D., Chern, J., Entin, J., Hou, A., Houser, P., et al. (2009). The Goddard multi-scale modeling system with unified physics. *Annales Geophysicae*, *27*(8), 3055–

3064. https://doi.org/10.5194/angeo-27-3055-2009

Trepte, C. (2021). CALIPSO: Data User's Guide - Data Product Descriptions - Lidar Level 2 Cloud and Aerosol Layer Products. Retrieved July 13, 2021, from https://www-calipso.larc.nasa.gov/resources/calipso_users_guide/data_summaries/layer/index.php#cad_score

Várnai, T., & Marshak, A. (2011). Global CALIPSO observations of aerosol changes near clouds. *IEEE Geoscience and Remote Sensing Letters*, *8*(1), 19–23. https://doi.org/10.1109/LGRS.2010.2049982

Várnai, T., & Marshak, A. (2015). Effect of cloud fraction on near-cloud aerosol behavior in the MODIS atmospheric correction ocean color product. *Remote Sensing*, *7*(5), 5283–5299. https://doi.org/10.3390/rs70505283

Várnai, T., Marshak, A., & Yang, W. (2013). Multi-satellite aerosol observations in the vicinity of clouds. *Atmospheric Chemistry and Physics*, *13*(8), 3899–39808. https://doi.org/10.5194/acp-13-3899-2013

Várnai, T., Marshak, A., & Eck, T. F. (2017). Observation-Based Study on Aerosol Optical Depth and Particle Size in Partly Cloudy Regions. *Journal of Geophysical Research: Atmospheres*, *122*(18), 10,013-10,024. https://doi.org/10.1002/2017JD027028

Vaughan, M. A., Powell, K. A., Kuehn, R. E., Young, S. A., Winker, D. M., Hostetler, C. A., et al. (2009). Fully automated detection of cloud and aerosol layers in the CALIPSO lidar measurements. *Journal of Atmospheric and Oceanic Technology*, *26*(10), 2034–2050. https://doi.org/10.1175/2009JTECHA1228.1

Wacker, S., Gröbner, J., Emde, C., Vuilleumier, L., Mayer, B., & Rozanov, E. (2009). Comparison of Measured and Modeled Nocturnal Clear Sky Longwave Downward Radiation at Payerne, Switzerland. *AIP Conference Proceedings*, *1100*(1), 589–592. https://doi.org/10.1063/1.3117055

Wang, H., Skamarock, W. C., & Feingold, G. (2009). Evaluation of Scalar Advection Schemes in the Advanced Research WRF Model Using Large-Eddy Simulations of Aerosol–Cloud Interactions. *Monthly Weather Review*, *137*(8), 2547–2558. https://doi.org/10.1175/2009MWR2820.1

Wild, M., Gilgen, H., Roesch, A., Ohmura, A., Long, C. N., Dutton, E. G., et al. (2005). From Dimming to Brightening : Decadal Changes in Solar Radiation at Earth ' s Surface. *Science*, *308*, 847–851. https://doi.org/10.1126/science.1103215

Wild, M., Folini, D., Schär, C., Loeb, N., Dutton, E. G., & König-Langlo, G. (2013). The global energy balance from a surface perspective. *Climate Dynamics*, *40*(11–12), 3107–3134. https://doi.org/10.1007/s00382-012-1569-8

Wollner, U., Koren, I., Altaratz, O., & Remer, L. A. (2014). On the signature of the cirrus twilight zone. *Environmental Research Letters*, *9*(9). https://doi.org/10.1088/1748-9326/9/9/094010

Yamaguchi, T., & Feingold, G. (2012). Technical note: Large-eddy simulation of cloudy boundary layer with the Advanced Research WRF model. *Journal of Advances in Modeling Earth Systems*, *4*(9). https://doi.org/10.1029/2012MS000164

Zdunkowski, W. G., Welch, R. M., & Korb, G. (1980). An investigation of the structure of typical two-stream-methods for the calculation of solar fluxes and heating rates in clouds. *Beiträge Zur Physik Der Atmosphäre*, *53*(2), 147–166.

Zhong, X., Ruiz-Arias, J. A., & Kleissl, J. (2016). Dissecting surface clear sky irradiance bias in numerical weather prediction: Application and corrections to the New Goddard Shortwave Scheme. *Solar Energy*, *132*, 103–113. https://doi.org/10.1016/j.solener.2016.03.009